

INFORMATION TO USERS

This manuscript has been reproduced from the microfilm master. UMI films the text directly from the original or copy submitted. Thus, some thesis and dissertation copies are in typewriter face, while others may be from any type of computer printer.

The quality of this reproduction is dependent upon the quality of the copy submitted. Broken or indistinct print, colored or poor quality illustrations and photographs, print bleedthrough, substandard margins, and improper alignment can adversely affect reproduction.

In the unlikely event that the author did not send UMI a complete manuscript and there are missing pages, these will be noted. Also, if unauthorized copyright material had to be removed, a note will indicate the deletion.

Oversize materials (e.g., maps, drawings, charts) are reproduced by sectioning the original, beginning at the upper left-hand corner and continuing from left to right in equal sections with small overlaps. Each original is also photographed in one exposure and is included in reduced form at the back of the book.

Photographs included in the original manuscript have been reproduced xerographically in this copy. Higher quality 6" x 9" black and white photographic prints are available for any photographs or illustrations appearing in this copy for an additional charge. Contact UMI directly to order.

UMI

A Bell & Howell Information Company
300 North Zeeb Road, Ann Arbor MI 48106-1346 USA
313/761-4700 800/521-0600

**Stress And Surface Deformation Due To Earthquakes And Volcanoes
In Alaska**

A
THESIS

Presented to the Faculty
of the University of Alaska Fairbanks
in Partial Fulfillment of the Requirements
for the Degree of

DOCTOR OF PHILOSOPHY

By
Zhong Lu, B.S., M.S.

Fairbanks, Alaska

August 1996

UMI Number: 9701146

**UMI Microform 9701146
Copyright 1996, by UMI Company. All rights reserved.**

**This microform edition is protected against unauthorized
copying under Title 17, United States Code.**

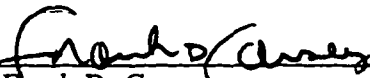
UMI
300 North Zeeb Road
Ann Arbor, MI 48103

**Stress And Surface Deformation Due To Earthquakes And Volcanoes
In Alaska**

by

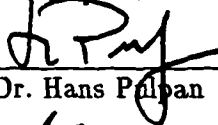
Zhong Lu


RECOMMENDED:

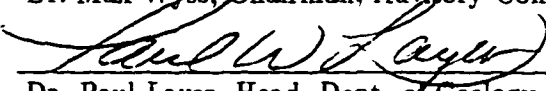

Dr. Frank D. Carsey


Dr. Douglas H. Christensen



Dr. Stephen R. McNutt

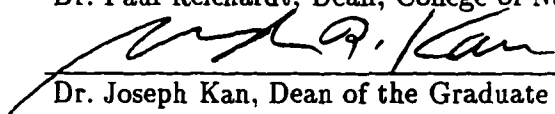

Dr. Hans Palpan


Dr. Max Wyes, Chairman, Advisory Committee


Dr. Paul Layer, Head, Dept. of Geology and Geophysics

APPROVED:


Dr. Paul Reichardt, Dean, College of Natural Sciences


Dr. Joseph Kan, Dean of the Graduate School

7/23/96
Date

Abstract

A new method has been developed to investigate stress homogeneity along plate boundaries based on the cumulative misfit between the theoretical and observed slip directions on fault planes of individual earthquake focal mechanisms, calculated using assumed stress tensors. This method allows identification of volumes with uniform stress directions, suitable for inversion for stress orientations, with a minimum of computing time. The method also affords an alternative estimate of the significance of differences in stress directions. Applying this method in the Aleutians, we found that the Aleutian plate boundary is segmented based on the observations that the misfits are relatively constant within segments of uniform stress orientation but that they change abruptly at segment boundaries. The segmentation boundaries correspond to fracture zones, boundaries of asperities and ends of aftershock zones of great earthquakes. Applying this method in the Alaska Wadati-Benioff Zone (WBZ), we depict the stress field at two different scales. The stress directions measured by large earthquakes ($M_s \sim 5$) are homogeneous, with extension down dip and greatest compression along strike. The unusual orientation of the greatest principal stress is attributed to the bend of the slab under central Alaska, which generates compressive stresses along strike. The stress directions measured by small earthquakes ($M_L \sim 3$), reveal a great deal of heterogeneity as a function of depth and along strike, although they show a trend that confirms the overall stress field derived from the large events. We propose that the ratio of the dimensions of the stress field (sensed by earthquakes) to the rupture dimensions is about 20 to 50.

Using ERS-1 Synthetic Aperture Radar (SAR) interferometry, we have constructed high resolution topographic maps, and detected several centimeters of uplift that accumulated during two years (1993-1995) at two neighboring volca-

noes in Alaska's Katmai National Park: New Trident vent and Novarupta Dome. From the uplift gradient we estimate the depth of the pressure source, presumably a magma body or hydrothermal system, under New Trident volcano to be 2 km. These are the first observations of volcanic deformation in this area and will be helpful to characterize the volcano's structure and behaviour.

Contents

Abstract	iii
List of Figures	viii
List of Tables	xii
Acknowledgments	xiii
1 Introduction	1
References	6
2 Segmentation of the Aleutian Plate Boundary Derived From Stress Direction Estimates Based on Fault Plane Solutions	13
2.1 Abstract	13
2.2 Introduction	15
2.3 Method	17
2.4 Data and Analysis	19
2.4.1 Stress Changes as a Function of Time	20
2.4.2 Stress Changes as a Function of Space	22
2.4.3 Stress Segmentation Sensitivity to the Reference Stress Model	24

2.4.4	Confirmation of Segment Boundaries by Stress Inversion in Moving Windows	25
2.4.5	Principal Stress Orientation	26
2.5	Discussion	27
2.6	Conclusions	33
2.7	References	34
3	Details of Stress Directions in the Alaska Subduction Zone From Fault Plane Solutions	48
3.1	Abstract	48
3.2	Introduction	50
3.3	Stress Tensor Inversion and the Cumulative Misfit Method	53
3.3.1	Stress Tensor Inversion Method	53
3.3.2	Criteria for Successful Inversions	54
3.3.3	The Cumulative Misfit Method	55
3.3.4	Test of the Cumulative Misfit Method	56
3.3.5	Discussion	60
3.4	Stress Directions Along the Alaska WBZ	62
3.4.1	Data	62
3.4.2	Analysis	63
3.4.2.1	Large Earthquakes in the WBZ	63
3.4.2.2	Small Earthquakes in the Crust	64
3.4.2.3	Small Earthquakes in the WBZ	65
3.4.3	Results and Discussion	67
3.4.3.1	Stress Directions in the Alaskan WBZ	67
3.4.3.2	Stress Directions in the Crust	70
3.5	Scale of the Stress Field and the Size of Earthquake Ruptures	72

3.6	Conclusions	73
3.7	References	76
4	Review of Interferometric SAR Theory	97
4.1	Introduction	97
4.2	Basics of SAR Interferometry	98
4.3	Phase in Interferograms	100
4.4	The Effect of Baseline and Topography on Range Difference	102
4.5	Errors in Elevation and Deformation Estimates	105
4.6	Correlation in INSAR Images	108
4.7	Phase Unwrapping	110
4.8	Limitations of the interferometric technique	111
4.9	References	113
5	Deformation of Volcanic Vents Detected by ERS-1 SAR Interferometry, Katmai National Park, Alaska	118
5.1	Abstract	118
5.2	Introduction	119
5.3	Analysis	122
5.4	Conclusion	128
5.5	References	130
6	Conclusions	141
A	Appendix	144

List of Figures

2.1	Map of aftershock areas (light shading) of earthquakes with $M_s \geq 7.4$ along the Aleutian arc from 1938 to 1986.	41
2.2	Cumulative misfit angle as a function of earthquake number (a) in the western part of the aftershock zone of the 1957 earthquake and (b) in the southwestern part of the aftershock zone of the 1964 earthquake.	42
2.3	(top) The epicenters of the earthquakes are shown as dots in the upper plot. (bottom) Cumulative misfit as a function of earthquake numbers which are ordered from west to east for the time interval from 1964 to 1993 is shown.	43
2.4	Epicenters of the earthquakes (dots) from 1964 to 1993 and segmentation boundaries of the Aleutian arc based on the stress distribution for the time intervals from 1964 to 1993, 1964 to 1986, and 1986 to 1993, respectively.	44
2.5	Cumulative misfit as a function of earthquake numbers for four reference stress tensors.	45
2.6	Average misfit angle for inversions for stress directions as a function of positions of the moving window for three different window lengths. (a) 17, (b) 25, and (c) 31 earthquakes.	46

2.7	Segmentation of the Aleutian arc based on the stress distribution estimated from fault plane solutions.	47
3.1	Average misfit for inversions for stress directions as a function of position of the moving windows for several window lengths, 10, 13, 15, 17, 20, 22, 25, 28, 30, 33, and 50.	83
3.2	Cumulative misfit as a function of earthquake number for seven reference stress tensors.	84
3.3	Average misfit (dots) and its standard deviation (dashed lines) as a function earthquake number.	85
3.4	Average misfits as a function of earthquake number for data sets selected randomly from 50 events, which come from a single stress regime.	86
3.5	Epicenter map of small earthquakes ($M_L \sim 3.0$) with fault plane solutions in Alaska.	87
3.6	Epicenter map of small crustal earthquakes ($M_L \sim 3$) with fault plane solutions in Alaska and stereographic projection of the best fitting principal stress directions for two homogeneous data sets: 1W (crosses), west McKinley; 2N (diamonds) (Table 3.1).	88
3.7	Epicenter map of large earthquakes ($M_s \sim 5$) with fault plane solutions in Alaska and stereographic projection of the best fitting principal stress directions for shallow WBZ events (triangles, set La in Table 3.1) and intermediate and deep WBZ earthquakes (stars, set Lb; dots, set Lc, in Table 3.1).	89
3.8	Cumulative misfit as a function of depth in polygon 1 (a), 2 (b), and 3 (c) defined in Figure 3.5.	90

3.9	Cumulative misfit as a function of strike at depth 120 - 140 km using seven different test stress tensors.	91
3.10	Epicenter map of small subcrustal earthquakes in the depth ranges 120 -140 km (crosses), and 60 - 75 km (circles), together with stereographic projections of the best fitting principal stress directions for subsets selected based on cumulative misfit slopes.	92
3.11	Epicenter map of small subcrustal earthquakes in the depth ranges 75 - 90 km (circles), 40 - 50 km (dots), and 0 - 40 km (triangles), together with stereographic projections of the best fitting principal stress directions for subsets selected based on cumulative misfit slopes (same as Figure 3.10).	93
3.12	Epicenter map of small subcrustal earthquakes in the depth ranges 90 - 120 km (circles), and 50 - 60 km (dots), together with stereographic projections of the best fitting principal stress directions for subsets selected based on cumulative misfit slopes (same as Figure 3.10).	94
3.13	The principal stress directions of several inversions did not yield meaningful results.	95
3.14	Map of stress directions in Alaska in the crust (thin bars) and in the subducting slab (thick bars) based on inversions of fault plane solutions of $M_L \sim 3$ earthquakes.	96
4.1	Geometry of an interferometric SAR	116
4.2	Baseline geometry of an interferometric SAR	117
5.1	Interferogram using ERS-SAR data for an area with dimensions of 17×14 km covering Novarupta Dome, the site of this century's largest eruption on Earth.	135

5.2	Topographic map of the area around Novarupta Dome (12 × 12 km) derived from an interferogram as shown in Figure 5.1.	136
5.3	ERS-1 radar image of Katmai group and surrounding region.	137
5.4	Interferograms at New Trident vent (a), and the area of Novarupta Dome (b).	138
5.5	Interferograms of New Trident vent (a), and in the area of Novarupta (b).	139
5.6	Comparison of histograms of correlation coefficients for an area with loss of coherence (a) and an area of inflated region at New Trident vent (b).	140
A.1	Schematic plot shows that the segmentation of the fault AZ which can be found made up of 4 sub-faults, AB, BC, CD, and DZ.	146
A.2	Cumulative misfit as a function of strike at depth 40 - 50 km using four different test stress tensors.	147
A.3	Cumulative misfit as a function of strike at depth 50 - 60 km using five different test stress tensors.	148
A.4	Cumulative misfit as a function of strike at depth 60 - 75 km using five different test stress tensors.	149
A.5	Cumulative misfit as a function of strike at depth 75 - 90 km using five different test stress tensors.	150
A.6	Cumulative misfit as a function of strike at depth 90 - 120 km using five different test stress tensors.	151

List of Tables

2.1	Stress inversion results for the Aleutians	40
3.1	Stress tensor results for the Alaska WBZ	81

Acknowledgments

This study was supervised by Max Wyss, the chairman of my advisory committee. I greatly appreciate Max's dedication to my study and me. I sincerely thank him for his enthusiasm, and excellent scientific guidance throughout the study.

I am grateful to the other members of my graduate advisory committee, Frank Carsey, Douglas Christensen, Stephen McNutt, and Hans Pulpan. Each of them made helpful suggestions for improving the dissertation and provided guidance in a variety of ways during the project.

I could not have learned the radar interferometry techniques without the tutoring of Shusun Li, and Dennis R. Fatland. I thank them for their generous contributions by providing some computer codes for constructing interferograms. The interferometry work is a team project. I thank Ken Dean, John Eichelberger, Jeff Freymeuller, Craig Lingle, Rick Guritz for their helpful discussions and support.

I also thank my friends and colleagues in Seismology lab, Alaska Volcano Observatory, and Alaska SAR Facility. Special thanks go to John Benoit, Stefan Wiemer, Hilary Fletcher, Dominique Gillard (Princeton University), Mitch Robinson, John Lahr, Art Jolly, Charlotte Rowe, Guy Tytgat. I quite enjoyed the daily "Lunch Gathering".

I, especially, thank my wife, Qun Chen, for her dedicated love, her encouragements, and her spiritual and moral support, which are the most important in my life.

Chapter 1

Introduction

This thesis consists of two projects: stress tensor orientations due to earthquakes (Chapters 2 and 3), and surface deformation on volcanoes (Chapters 4 and 5).

The determination of the tectonic stress field is of major concern in tectonics and seismology. The direction of shear stress on a fault plane can be expressed as a function of the principal stress directions, the ratio of the magnitudes of the principal stresses, and the orientation of fault planes [e.g. *Bott*, 1959; *Angelier*, 1979]. Assuming that all earthquakes have occurred in response to the regional stress field, and that the slip direction of the fault plane coincides with the shear stress direction, many attempts have been made to construct the stress field using earthquake focal mechanisms. Articles developing methods include: *Angelier* [1979]; *Etchecopar et al.* [1981]; *Angelier et al.* [1982]; *Angelier* [1984]; *Gephart and Forsyth* [1984]; *Michael* [1984]; *Gephart* [1985]; *Reches* [1987]; *Angelier* [1990]; *Gephart* [1990]; *Yin and Ranalli* [1993]. Articles applying methods include: *Vasseur et al.* [1983]; *Gephart and Forsyth* [1985]; *Lana and Correig* [1987]; *Michael* [1987]; *Angelier* [1989]; *Huang and Angelier* [1989]; *Bergerat et al.* [1990]; *Rivera and Cisernas* [1990]; *Vetter* [1990]; *Fleischmann and Nemcok* [1991]; *Liang and Wyss*

[1991]; *Will and Powell* [1991]; *Gillard et al.* [1992]; *Wyss et al.* [1992]; *Neri and Wyss* [1993]; *Hartse et al.* [1994]; *Hauksson* [1994]; *Jolly et al.* [1994]; *Gillard and Wyss* [1995]; *Gillard et al.* [1995]; *Horiuchi et al.* [1995]; *Wyss and Lu* [1995]; *Yin and Rogers* [1995]; *Lu and Wyss* [1996]; *Petit et al.* [1996]. All the techniques to invert fault plane solutions for stress tensor orientation minimize a measure of the misfit between the observed and the theoretical slip directions on fault planes.

The fundamental assumption for deriving stress orientations based on earthquake focal mechanism data is that the stress-tensor is uniform in the volume from which the data are taken [e.g. *Angelier*, 1979; *Michael*, 1984; *Gephart and Forsyth*, 1984; *Yin and Ranalli*, 1993]. However, it is difficult to verify whether the assumption of uniform stress direction is fulfilled in any given data set. *Wyss et al.* [1992] and *Gillard and Wyss* [1995] have proposed that in some data sets, average misfit (F) $> 6^\circ$ may indicate that the assumption is violated, because $F < 6^\circ$ can be explained by errors in the fault parameters. Based on this observation, they could judge whether inversion results were acceptable or not, but they could not know this before the inversions. Up to now the selection of the spatial limits of the data set was done subjectively, based on tectonic considerations, such as clustering of epicenters, fault strike, and style of faulting. In this thesis, a new method is developed to define quantitatively the extent of volumes with uniform stress directions. The fault plane solutions in individual subsets are then inverted efficiently for stress tensor orientations. This is the topic of Chapter 2.

The overall picture of stress directions in subduction zones was essentially settled during the discoveries related to plate tectonics: subducting slabs act as stress guides, which are either in compression or tension [e.g. *Isacks and Molnar*, 1971; *Isacks et al.*, 1968; *Bhattacharya and Biswas*, 1979; *House and Jacob*, 1983]. The significant bends of the Alaska Wadati-Benioff Zone (WBZ) permit substantial deviations in the stress field from the basic conditions, as expected from detailed

numerical models [e.g. *Creager et al.*, 1995]. In addition, perturbations of the stress directions may also exist in relatively straight slab segments as suggested by the orientations of P and T axes of small earthquakes or composite solutions [e.g. *Reyners and Coles*, 1982; *Matsuzawa et al.*, 1986; *Smith et al.*, 1993; *Wiens et al.*, 1993; *Comte and Suarez*, 1994; *Iguchi et al.*, 1995]. Some detailed analyses of subducting slabs, which have concentrated on mapping the P- and T-axes [e.g. *Lahr et al.*, 1993, 1994; *Iguchi et al.*, 1995] found variations in these parameters. However, it is not necessarily correct to interpret the P and T axes as the directions of the greatest and least principal stresses because earthquakes could occur along faults which are preexisting planes of weakness [*McKenzie*, 1969]. In Chapter 3 of this thesis we investigate, for the first time, the details of the stress directions on scales of a few tens of kilometers in the Alaska WBZ. We use the verified focal mechanisms of earthquakes, instead of P and T axes, to resolve stress directions in small volumes of the slab, and apply an objective method developed in Chapter 2 to find volumes of homogeneous stress directions. We also further refine the criteria for judging the inversion results.

The question of the scale at which directions of stress can be estimated from fault plane solutions has not been discussed in detail by seismologists. Geologists, on the other hand, are aware of the problem of scale. *Rebai et al.* [1992] showed how large and small faults may perturb the regional stress field and lead to locally varying conditions. Therefore, it is not likely that ruptures of substantial segments of large faults would reflect local perturbations of the stress field. Instead we expect them to respond to the large-scale, overall stress field. In this thesis, we will invert separately the fault plane solutions of large and small earthquakes in the Alaska WBZ. Such separation will allow us to examine the stress orientations in the same area at two different, independent scale lengths. Based on the results from this thesis and previous studies [*Gillard et al.*, 1995; *Gillard and Wyss*, 1995]

a relationship between the rupture dimensions of earthquakes and the dimensions of the stress field that generate these earthquakes will be proposed.

Many eruptions of the world's volcanoes are accompanied by significant surface deformation, and thus precise monitoring of surface deformation could contribute to accurate predictions of volcanic eruption [e.g. *Newhall and Dzurisin*, 1988; *Thatcher*, 1990; *Shimada et al.*, 1990]. However, very few of the world's active volcanoes are being monitored geodetically. Furthermore, it is often difficult or impossible to acquire the necessary geodetic measurements with conventional techniques without putting field crews at significant risk. Synthetic Aperture Radar (SAR) interferometry has the potential to provide the requisite data. The repeat-pass of C-band ERS-1 Interferometric SAR (INSAR) has been used to measure the velocity field of glaciers [e.g. *Goldstein et al.*, 1993; *Joughin et al.*, 1995; *Kwok and Fahnestock*, 1996], and the displacement from earthquakes [e.g. *Massonnet et al.*, 1993, 1994; *Zebker et al.*, 1994; *Massonnet and Feigl*, 1995; *Peltzer and Rosen*, 1995]. *Murakami et al.* [1995, 1996] demonstrated that L-band repeat-pass JERS-1 INSAR could be used to map the displacement field of earthquakes and to detect crustal deformation. *Massonnet et al.* [1995] were the first to map the deflation associated with the eruption of Etna volcano by interferometric SAR. In Chapter 5, we report, for the first time, on a successful attempt to use ERS-1 interferometry to monitor long-term uplift at two Alaska's volcanoes at Katmai National Park.

In Chapter 2, a new method is introduced to find sub-volumes where the stress directions are uniform. This method is tested and applied to the Aleutian plate boundary. In Chapter 3, the method described in Chapter 2 was applied to the Alaska WBZ to derive detailed stress orientations along the strike as well as down-dip. In addition, the criteria for judging the stress inversion results are summarized, and the relationship between the rupture dimensions of earthquakes and the dimensions of the stress field that generate these earthquakes is proposed.

In Chapter 4, the basics of SAR interferometry are reviewed. In Chapter 5, the reasons for experimenting with the SAR interferometry technique on Alaska's volcanoes is discussed. A high resolution topography map is produced by INSAR, and the several centimeters inflation associated with the long-term deformation of two Alaska volcanoes detected by INSAR during the 1993 and 1995 is reported.

References

- Angelier, J., Determination of the mean principal directions of stresses for a given fault population. *Tectonophysics*, *56*, T17-T26, 1979.
- Angelier, J., A. Tarantola, G. Valette, and S. Manoussis. Inversion of field data in fault tectonics to obtain the regional stress. I, single phase fault populations: A new method of computing the stress tensor. *Geophys. J. R. Astron. Soc.*, *69*, 607-621, 1982.
- Angelier, J., Tectonic analysis of fault slip data sets. *J. Geophys. Res.*, *89*, 5835-5848, 1984.
- Angelier, J., From orientation to magnitude in paleostress determinations using fault slip data. *J. Struct. Geol.*, *11*, 37-50, 1989.
- Angelier, J., Inversion of field data in fault tectonics to obtain the regional stress - III. a new rapid direct inversion method by analytical means. *Geophys. J. Int.*, *103*, 363-376, 1990.
- Bergerat, F., J. Angelier, and T. Villemin. Fault systems and stress patterns on emerged oceanic ridges: a case study in Iceland. *Tectonophysics*, *179*, 183-197, 1990.
- Bott, M. H. P., The mechanics of oblique slip faulting, *Geol. Mag.*, *96*, 109-117, 1959.
- Bhattacharya, B., and N. N. Biswas, Implications of north Pacific plate tectonics in central Alaska: focal mechanisms of earthquakes. *Tectonophysics*, *53*, 99-130, 1979.
- Comte, D., and G. Suarez. An inverted double seismic zone in Chile: evidence of phase

- transformation in the subducted slab, *Science*, *263*, 212-215, 1994.
- Creager, C., L. Y. Chiao, J. P. Winchester, and E. R. Engdahl, Membrane strain rates in the subducting plate beneath South America. *Geophys. Res. Letts.*, *22*, 2321-2324, 1995.
- Etchecopar, A., B. Vasseur, and M. Daignieres. An inverse problem in microtectonics for the determination of stress tensors from fault striation analysis. *J. Struct. Geol.*, *3*, 51-56, 1981.
- Fleischmann, K.H., and M. Nemcok. Paleostress inversion of fault-slip data using the shear stress solutions of means. *Tectonophysics*, *196*, 195-202, 1991.
- Gephart, J. W., and D. W. Forsyth, An improved method of determining the regional stress tensor using the earthquake focal mechanism data: Application to the San Fernando earthquake sequence. *J. Geophys. Res.*, *89*, 9305-9320, 1984.
- Gephart, J. W., Principal stress directions and the ambiguity in fault plane identification from focal mechanism, *Bull. Seism. Soc. Am.*, *75*, 621-625, 1985.
- Gephart, J. W., FMSI: a FORTRAN program for inverting fault/slickenside and earthquake focal mechanism data to obtain the original stress tensor. *Computer and Geosciences*, *16*, 953-989, 1990.
- Gillard, D., M. Wyss, and J. S. Nakata, A seismotectonic model for western Hawaii based on stress- tensor inversion from fault-plane solutions, *J. Geophys. Res.*, *97*, 6629-6641, 1992.
- Gillard, D., and M. Wyss, Comparison of strain and stress tensor orientation: Application to Iran and southern California, *J. Geophys. Res.*, *100*, *in press*, 1995.
- Gillard, D., M. Wyss, and P. Okubo, Stress and strain tensor orientations in the south flank of Kilauea, Hawaii, estimated from fault plane solutions, *J. Geophys. Res.*, *100*, *in press*, 1995.

- Goldstein, R. M., H. Engelhardt, B. Kamb, and R. M. Frolich. Satellite Radar Interferometry for Monitoring Ice Sheet Motion: Application to an Antarctic Ice Stream. *Science*, *262*, 1525-1530, 1993.
- Hartse, H. E., R. C. Aster, M. C. Fehler, J. S. Scott, and F. L. Vernon, Small-scale stress heterogeneity in the Anza seismic gap, southern California. *J. Geophys. Res.*, *99*, 6801-6818, 1994.
- Hauksson, E., State of stress from focal mechanisms before and after the 1992 Landers earthquake sequence, *Bull. Seism. Soc. Am.*, *84*, 917-934, 1994.
- Horiuchi, S., G. Rocco, and A. Hasegawa. Discrimination of fault planes from auxiliary planes based on simultaneous determination of stress tensor and a large number of fault plane solutions. *J. Geophys. Res.*, *100*, 8327-8338, 1995.
- House, L. S., and K. H. Jacob. Earthquakes, plate subduction, and stress reversals in the eastern Aleutian arc. *J. Geophys. Res.*, *88*, 9347-9373, 1983.
- Huang, Q, and J. Angelier, Inversion of field data in fault tectonics to obtain the regional stress, II. using conjugate sets within heterogeneous families for computing paleostress axes. *Geophys. J.*, *96*, 139-149, 1989.
- Iguchi, M., K. Ishihara, and Y. Tatsumi. Characteristics non-down-dip-extensional intermediate-depth earthquakes immediately beneath the volcanic front in South Kyushu, Japan. *Geophys. Res. Letts.*, *22*, 1905-1908, 1995.
- Isacks, B., J. Oliver, and L. R. Sykes, Seismology and the new global tectonics. *J. Geophys. Res.*, *73*, 5855-5899, 1968.
- Isacks, B., and P. Molnar, Distribution of stresses in the descending lithosphere from a global survey of focal mechanism solution of mantle earthquakes, *Rev. Geophys. Space Phys.*, *9*, 103, 1971.
- Jolly, A. D., R. A. Page, and J. A. Power, Seismicity and stress in the vicinity of Mount

- Spurr volcano, south central Alaska, *J. Geophys. Res.*, *99*, 15305-15318, 1994.
- Joughin, I. R., D. P. Winebrenner, and M. A. Fahnestock. Observation of complex ice-sheet motion in Greenland using satellite radar interferometry, *Geophys. Res. Letts.*, *22*, 571-574, 1995.
- Kwok, R., and M. A. Fahnestock. Ice sheet motion and topography from radar interferometry, *IEEE Transactions on Geoscience and Remote Sensing*, *34*, 189-200, 1996.
- Lahr, J., C. D. Stephens, R. Page, and K. Fogleman, characteristics of the Aleutian Wadati- Benioff zone seismicity beneath southern Alaska, 301-303, *SUBCON: An Interdisciplinary Conference on the subduction Process*, Catalina Island, California, 1994.
- Lahr, J., K. Fogleman, and R. Page, Stress within the Pacific plate of Southern Alaska, *EOS. Transactions, AGU*, *74*, 95, 1993.
- Lana, X., and A. M. Correig, An example of stress tensor distribution deduced from the aftershocks of the November 23, 1980 southern Italy earthquake, *Tectonophysics*, *135*, 289-296, 1987.
- Liang, B., and M. Wyss, Estimates of orientation of stress and strain tensors based on fault plane solutions in the epicenter area of the great Hawaiian earthquake of 1868, *Bull. Seis. Soc. Am.*, *81*, 2320-2334, 1991.
- Lu, Z., and M. Wyss, Segmentation of the Aleutian plate boundary derived from stress direction estimates based on fault plane solutions, *J. Geophys. Res.*, *101*, 803-816, 1996.
- Massonnet, D., M. Rossi, C. Carmona, F. Adragna, G. Peltzer, K. Feigl, and T. Rabauté. The displacement field of the Landers earthquake mapped by radar interferometry, *Nature*, *364*, 138-142, 1993.
- Massonnet, D., and K. L. Feigl, Satellite radar interferometric map of the coseismic

- deformation field of the M=6.1 Eureka Valley, California earthquake of May 17, 1993. *Geophys. Res. Letts.*, *22*, 1541-1544, 1995.
- Massonnet, D., K. Feigi, M. Rossi, C. Carmona, and F. Adragna, Radar interferometry mapping of deformation in the year after the landers earthquake. *Nature*, *369*, 227-229, 1994.
- Massonnet, D., P. Briole, and A. Arnaud, Deflation of Mount Etna monitored by space-borne radar interferometry, *Nature*, *375*, 567-570, 1995.
- Michael, A. J., Determination of stress from slip data: faults and folds. *J. Geophys. Res.*, *89*, 11517-11526, 1984.
- Michael, A. J., Use of focal mechanisms to determine stress: a control study. *J. Geophys. Res.*, *92*, 357-368, 1987.
- Matsuzawa, T., N. Umino, A. Hasegawa, and A. Takagi, Normal fault type events in the upper plane of the double-planed deep seismic zone beneath the northeastern Japan arc, *J. Phys. Earth*, *34*, 85-94, 1986.
- McKenzie, D. P., The relationship between fault plane solutions for earthquakes and the directions of the principal stresses. *Bull. Seism. Soc. Am.*, *59*, 591-601, 1969.
- Murakami, M., S. Fujiwara, M. Nemoto, T. Saito, P. Rosen, M. Tobita, and C. Werner, Application of the interferometric JERS-1 SAR for detection of crustal deformations in the Izu Peninsula, Japan. *EOS, Trans. Am. Geophys. Union*, *76*, F63, 1995.
- Murakami, M., M. Tobita, S. Fujiwara, T. Saito, and H. Massaharu, Coseismic crustal deformations of 1994 Northridge California earthquake detected by interferometric JERS-1 SAR. *J. Geophys. Res.*, *in prsss*, 1996.
- Nakamura, K., K. H. Jacob, and J. N. Davies, Volcanoes as possible indicators of tectonic stress orientation - Aleutians and Alaska, *PAGEOPH*, *115*, 87-112, 1977.
- Neri, G., and M. Wyss, Stress in Sicily, *Geophys. J. Int.*, *113*, 1111-1121, 1995.

- Newhall, C. G., and D. Dzurisin. Historical unrest at large calderas of the world. *U.S. Geol. Surv. Bulletin*, 1855, 1988.
- Peltzer, G., and P. Rosen, Surface displacement of the 17 May 1993 Eureka Valley, California, earthquake observed by SAR interferometry, *Science*, 268, 1333-1336, 1995.
- Petit, C., J. Deverchere, and F. Houdry, Present stress field changes along the Baikal rift and tectonic implications, *Tectonics*, *in press*, 1996.
- Rebai, S., H. Philip, and A. Taboada, Modern tectonic stress field in the Mediterranean region: evidence for variation in stress directions at different scales, *Geophys. J. Int.*, 110, 106-140, 1992.
- Reches, Z., Determination of the tectonic stress tensor from slip along faults that obey the Coulomb yield conditions, *Tectonics*, 6, 849-861, 1987.
- Reyners, M., and K. Coles, Fine structure of the dipping seismic zone and subduction mechanics in the Shumagin Islands, Alaska, *J. Geophys. Res.*, 87, 356-366, 1982.
- Rivera, L., and A. Cisternas, Stress tensor and fault plane solutions for a population of earthquakes, *Bull. Seism. Soc. Am.*, 80, 600-614, 1990.
- Shimada, S., Y. Fujinawa, S. Sekiguchi, S. Ohmi, T. Eguchi, and Y. Okada, Detection of a volcanic fracture using GPS, *Nature*, 343, 631-633, 1990.
- Smith, S. W., J. S. Knapp, and R. C. McPherson, Seismicity of the Gorda plate, structure of the continental margin, and an eastward jump of the Mendocino triple junction, *J. Geophys. Res.*, 98, 8153-8171, 1993.
- Thatcher, W., Precursors to eruption, *Nature*, 343, 590-591, 1990.
- Vasseur, G., A. Etchecopar, and H. Philip, State of stress inferred from multiple focal mechanism, *Ann. Geophys.*, 1, 291-298, 1983.
- Vetter, U. R., Variation of the regional stress tensor at the western great Basin boundary

- from the inversion of earthquake focal mechanisms, *Tectonics*, *9*, 63-79, 1990.
- Wiens, D. A., J. J. McGuire, and P. J. Shore. Evidence for transformational faulting from a deep double seismic zone in Tonga, *Nature*, *364*, 790-793, 1993.
- Will, T. M., and R. Powell. A robust approach to the calculation of paleostress field from fault plane data, *J. Struct. Geol.*, *13*, 813-821, 1991.
- Wyss, M., B. Liang, W. R. Tanigawa, and X. Wu. Comparison of orientations of stress and strain tensors based on fault plane solutions in Kaoiki Hawaii, *J. Geophys. Res.*, *97*, 4769- 4790, 1992.
- Wyss, M., and Z. Lu. Plate boundary segmentation by stress directions: Southern San Andreas fault, California, *Geophys. Res. Letts.*, *22*, 547-550, 1995.
- Yin, Z. M., and G. Ranalli. Determination of tectonic stress field from fault slip data: toward a probabilistic model, *J. Geophys. Res.*, *98*, 12165-12716, 1993.
- Yin, J. M., and G. C. Rogers. Rotation of the principal stress directions due to earthquake faulting and its seismological implications, *Bull. Seism. Soc. Am.*, *85*, 1513-1517, 1995.
- Zebker, H. A., P. A. Rosen, R. M. Goldstein, A. Gabriel, and C. L. Werner. On the derivation of coseismic displacement fields using differential radar interferometry: The Landers earthquake, *J. Geophys. Res.*, *99*, 19617-19634, 1994.

Chapter 2

Segmentation of the Aleutian Plate Boundary Derived From Stress Direction Estimates Based on Fault Plane Solutions

2.1 Abstract

We propose a new method to investigate stress homogeneity along plate boundaries based on the cumulative misfit of individual fault plane solutions, calculated using assumed stress tensors. Using this method, some segments of faults can be defined, without the time-consuming inversions for stress directions from earthquake fault plane solutions. We assume that the misfits are relatively constant within segments of uniform stress orientation but that they change abruptly at

⁰This chapter contains the complete text and figures of the manuscript, Segmentation of the Aleutian plate boundary derived from stress direction estimates based on fault plane solutions, by Z. Lu and M. Wyss, as published in *J. Geophys. Res.*, 101, 803-816, 1996.

boundaries of segments. This assumption is supported by the pattern of misfits observed for about 400 earthquakes located along the Aleutian subduction zone from 170°E to 145°W , which occurred between 1964 and 1993. The efficacy of the approach is confirmed by stress inversion analysis of moving windows. The cumulative misfit as a function of strike along the Aleutian arc shows there are five first-order boundaries where the stress directions change significantly. The first one is near 177.5°E , which corresponds to the northward projection of the Rat fracture zone. The second one falls on the Adak fracture zone. The third is near the locus where the Amlia fracture zone intersects the trench. The fourth lies on the easternmost end of the 1957 aftershock zone. The last is located where the two major asperities of the 1964 rupture are separated. The segmentation boundaries found in our analysis may be controlled by the fracture zones in the subducted plate. This observation may be interpreted as due to decoupling within the underthrusting plate along the zones of weakness (the fracture zones) across which stress may not be transmitted fully. The boundaries defined by our method may also be related to the asperity and aftershock distributions of great earthquakes. The focal mechanism data in the segments defined as stress-homogeneous by our method are then used to invert for the principal stress orientations by employing the Focal Mechanism Stress Inversion (FMSI) computer programs of Gephart. We find that the stress directions within these segments are different from each other, where they can be defined well, and the average misfits in these volumes are very small (2.8° and 5.5°). The method is not robust enough to detect all the stress segmentation boundaries based on only one reference stress tensor. Analyses with different reference stress models help to define most or all the stress segmentation boundaries.

2.2 Introduction

The seismological evidence for the segmentation of the Aleutian arc, which has a history of rupturing in great earthquakes, is based on the distribution of the aftershock zones of these ruptures. The most recent sequence, beginning in 1938 ($M_w = 8.2$), ruptured almost the entire Aleutian arc (Figure 2.1) in 1957 ($M_w = 8.6$), 1964 ($M_w = 9.2$), and 1965 ($M_w = 8.7$). The segments of the arc which have apparently not ruptured during this sequence are seismic gaps where future large earthquakes may be likely. Thus the Aleutian arc consists of several segments, delineated by boundaries of the aftershock zones of the great earthquakes. Because there is little overlap between aftershock zones of the 1965 and 1957 earthquakes and because the aftershock zones of the 1964 earthquake and the 1938 earthquake abut, this kind of segmentation is used as the basis for estimating seismic potential along the Aleutians [*Nishenko and McCann*, 1981]. However, the 1986 ($M_w = 8.0$) shock occurred within the rupture area of the 1957 earthquake, which had been thought to have a low seismic potential for the next few decades [*Nishenko and McCann*, 1981]. The seismic potential had to be reevaluated [*Nishenko and Jacob*, 1990] as the apparent segmentation changed based on the aftershock zone of the 1986 earthquake. The asperity distributions of great earthquakes may also reflect the heterogeneous stress conditions in the main thrust zone along the Aleutian arc. However, this information is not taken into account when estimating the seismic potential.

The geological evidence for the segmentation of the western Aleutian arc, on the other hand, is based on the facts that the arc is cut by several large transverse canyons (Figure 2.1). *Geist et al.* [1988] and *Ryan and Scholl* [1993] proposed that the western Aleutian arc is composed of discrete clockwise rotating and westward translating blocks, which are bounded by submarine canyons oriented transverse to

the arc. In their models, the transverse canyons are formed by differential rotation and along-arc translation of blocks of the arc massif. This segmentation is also used as the basis for estimating the seismic potential and time to failure in the Alaska-Aleutians region [Bufe *et al.*, 1994].

The earthquake focal mechanism data in an area can be used to infer the stress tensor orientation. As earthquakes can occur along faults which are preexisting planes of weakness [McKenzie, 1969], it is not necessarily correct to interpret the P and T axes as the directions of the greatest and least principal stresses. By assuming that the slip on the fault plane occurs in the direction of the resolved shear stress [Bott, 1959; McKenzie, 1969] and that the stress orientation is homogeneous in the study area [Angelier, 1979], Gephart and Forsyth [1984] developed an inversion algorithm which finds a best fitting principal stress tensor to a group of earthquakes by a grid search over a range of possible models. The potential pitfall of this inversion method is that a composite stress tensor may be obtained if the data set is composed of sets from more than one volume with significantly different stress orientations [Michael, 1987] and that this solution may not readily be identified as incorrect. Therefore care must be taken to identify reasonably homogeneous populations of data.

The portion of the average misfit, F , that could be due to fault plane solution errors of approximately 10° was estimated as ranging up to $F = 6^\circ$, based on synthetic data sets [Wyss *et al.*, 1992; Gillard and Wyss, 1995]. In no data set can we be certain what portion of the average misfit is due to errors of the fault plane solutions and what is due to stress heterogeneity. However, since values of $F \leq 6^\circ$ can be explained by modest errors in the fault plane solutions, we will accept results with $F \leq 6^\circ$ as satisfying the homogeneity requirement. Inversions with $F > 6^\circ$ will be suspect of containing some heterogeneous data, although errors in fault plane solutions of approximately 15° may occur and contribute to an increase

of F into the range $6^\circ < F < 9^\circ$. The most informative criterion on homogeneity that we will employ is the following: if subsets of data can be formed by dividing as a function of space or time which results in a substantial reduction of F (say from $F \simeq 6^\circ$ to $F \simeq 3^\circ$), then we conclude that part of the initial misfit was due to heterogeneity.

In this paper, a new method is used to investigate the segmentation of major plate boundaries or faults. We hypothesize that stress directions are uniform within segments of the plate boundaries and that they change abruptly across the boundaries between the segments. If this is the case, we should be able to define segments of constant slope in misfit plots. Within each segment we will then be able to calculate meaningful stress directions by inversion of the fault slip data. If we can show that this method works, we will be able to avoid extensive computing, which is necessary if we try to delineate segments of constant stress directions by iterative inversions of many subsets of the data. In this paper we will use the computing-intensive approach of inverting for many data sets using a sliding window, in order to confirm the cumulative misfit method. The statistical significance of our method to identify the segment boundaries is tested quantitatively. We use this method to estimate the segmentation of the Aleutian arc. The relationships between the boundaries of the proposed segmentation along the Aleutian arc, the tectonic features of the oceanic plate, and the asperity boundaries of the great earthquakes are also discussed.

2.3 Method

We assume the stress in a particular large volume is heterogeneous as a whole but can be considered homogeneous in subvolumes. Our purpose is to find where the segmentation boundaries may be located. We propose as a reference tensor

the stress model that fits well a subgroup of earthquakes and then calculate the misfit of each individual earthquake with respect to this stress model. The stress model is defined by the azimuths and plunges of the three principal stresses and the measure of stress magnitude. R , indicating the magnitude ratio of the intermediate principal stress relative to the two extreme ones ($R = (\sigma_2 - \sigma_1) / (\sigma_3 - \sigma_1)$, where σ_1 , σ_2 , and σ_3 are greatest, intermediate, and least principal stress). The misfit is defined as the smallest rotation angle about an axis of any orientation that would bring the direction and sense of slip, associated with either of the two observed nodal planes, into agreement with the direction and the sense of slip predicted by the stress model.

Earthquakes happen in a three-dimensional space. But the distribution of earthquakes along a major fault or a plate boundary can be simplified into one-dimensional space, that is, by specifying the direction along the strike of the fault and neglecting the depth as a spatial parameter. We order the earthquakes sequentially from one end of the fault to the other. The plot of the cumulative misfit as a function of the earthquake number can then be used to derive some information about the segmentation of the fault [Wyss and Lu, 1995].

In our method, the statistical significance of the stress differences across a boundary of two segments can be quantitatively expressed by the z test (number of samples greater than 30) or the t test (number of samples smaller than 30):

$$z = \frac{\mu_1 - \mu_2}{\sqrt{\frac{s_1^2}{n_1} + \frac{s_2^2}{n_2}}}, \quad (2.1)$$

$$t = \frac{(\mu_1 - \mu_2)\sqrt{n_1 + n_2 - 2}}{\sqrt{(n_1 - 1)s_1^2 + (n_2 - 1)s_2^2}\sqrt{\frac{1}{n_1} + \frac{1}{n_2}}}. \quad (2.2)$$

where μ_1 is the mean misfit in segment 1, μ_2 is the mean misfit in segment 2, s_1 and s_2 are the standard deviations in the two segments, and n_1 and n_2 are the numbers of earthquakes.

2.4 Data and Analysis

The main source for the earthquake focal mechanism data is the Harvard Centroid Moment Tensor (CMT) catalog for the period from 1977 to 1993. All the earthquakes in this catalog have magnitudes $M_w \geq 5.0$. We also collected the available earthquake data with focal mechanisms from the following studies: *Stauder and Udias* [1963], *Stauder and Bollinger* [1966], *Stauder* [1968a, b, 1972], *Davies et al.* [1981], *House and Jacob* [1983], and *Newberry et al.* [1986].

The earthquakes are divided into four distinct groups based on their locations [*Taber et al.*, 1991]: (1) trench and outer rise, (2) main thrust zone, (3) upper plate, and (4) Wadati-Benioff zone. In this paper, only the earthquakes in the main thrust zone are used to study the segmentation of the Aleutian arc.

Most of the seismic strain generated by the plate convergence is released by the earthquakes in the main thrust zone, which generally extends 50 to 120 km arcward from the trench. The main thrust zone extends to approximately 40-km depth [*Tichelaar and Ruff*, 1993]. Its thickness is about 10 - 20 km [*Ekstrom and Engdahl*, 1989]. One important feature is that the region between 173°W and 171.5°W and the one from 152°W to 149°W lack moderate-sized earthquakes. There has been no earthquake with $M_w \geq 5.0$ in those regions at least since 1977. Another important characteristic is that the main thrust earthquakes seem to cluster. West of 174°E, the lower part of the main thrust zone lacks seismicity in the $M_w \geq 5.0$ range. The upper part of the main thrust zone between 175°W and 173°W lacks $M_w \geq 5.0$ earthquakes.

Our goal is to try to define the segmentation of the Aleutian arc in terms of stress homogeneity. Our data span the period from 1964 to 1993. However, the great earthquakes may affect the orientation of the stress field. Thus we define the segmentation of the Aleutian arc by the following two steps: we first plot

the cumulative misfit as a function of time for the aftershock zones of 1964 and 1986 earthquakes to see whether the stress direction of the aftershock sequence is different from that of the background (before the main shock) and/or from that of the foreground (after the main shock) stress fields. The aftershock sequence is eliminated from the data set defining the segmentation if its stress direction differs from that of the background and foreground. The remaining data without the aftershocks are used for the analysis of the stress segmentation of the Aleutian arc. We analyzed the stress distribution with time for the 1964 and 1986 aftershock zones only. The aftershock sequences of the 1957 and 1965 earthquake were not studied because our database does not contain enough information for these two shocks.

We estimated the stress directions using the Focal Mechanism Stress Inversion (FMSI) computer codes of *Gephart* [1990] for the earthquake focal mechanism data in the western half of the 1957 aftershock zone ($173^{\circ}\text{W}/180^{\circ}\text{W}$) for the period from 1964 to 1993 and employed this as the standard solution, based on which all misfits for individual earthquakes are calculated. The stress model used for the following analyses is $\sigma_1 = 30/156$, $\sigma_2 = 4/63$, $\sigma_3 = 60/326$ (plunge and azimuth, respectively), and $R = 0.6$.

2.4.1 Stress Changes as a Function of Time

The cumulative misfit as a function of time for the western part of the 1957 aftershock zone (west of 172°W) is shown in Figure 2.2a. The main shock of 1986 corresponds to earthquake number 55. The aftershock sequence of 1986 clearly shows the lowest slope, i.e., the lowest average misfit of 2.2° compared with an average misfit of 4.0° for the rest. The last earthquake conforming to the stress pattern of the aftershocks, number 78, took place on October 18, 1986, 6 months

after the main shock. Five preshocks, starting from earthquake number 50 (July 17, 1985, 10 months before the main shock), exhibit a stress direction similar to that of the aftershock sequence. We can regard the whole data set in this plot as comprising three sequences with fairly constant misfits (1) earthquake number 1 to 49, (2) earthquake number 50 to 78, that is, five preshocks and 24 aftershocks, and (3) earthquake number 81 to 122, respectively. Using the z test, we find that sequence 1 is similar to sequence 3, but both are significantly different from that of sequence 2 at the 99% confidence level (Figure 2.2a). We conclude that the 1986 preshock and aftershock sequence is more homogeneous than earthquakes that occurred at other times in the western Aleutian arc. This difference may be interpreted in two ways. Either the stress tensor was more homogeneous during the preshock and aftershock sequence, or the fault plane solutions of that sequence were more similar to each other than at other times. Thus the data set without the earthquakes number 50 to 78 has fairly constant misfits as a function of time and is used to analyze the stress segmentation of the Aleutian arc.

The cumulative misfit as a function of time for the southwestern part of the 1964 aftershock zone (south of 57°N) is shown in Figure 2.2b. The events from number 1 (2 months before the main shock) to 3 are the preshocks of the 1964 main shock. A clear change in mean misfit (slope in Figure 2.2b) occurs at event 18 (June 23, 1965), although one unusually large misfit during the aftershock sequence disturbs the pattern. The average misfits for the period before and after June 23, 1965, are 4.0° (3.1° if the single largest misfit of the data set is excluded) and 5.9° , respectively. Since event number 17, just before the noticeable change in slope, occurred on September 27, 1964, we propose that it is the last undisputable aftershock and thus the foreshock and aftershock sequence in this case is also more homogeneous (or more similar to each other) than the earthquakes occurring at other times. The misfits remain relatively constant between September 27, 1964,

and 1993. Again, we conclude that the stress directions derived from the data after September 27, 1964, do not change with time.

From the above analysis of slip vector misfits as a function of time, we conclude that the aftershock sequences of the 1964 and 1986 events can be interpreted as reflecting a more homogeneous stress tensor than those of the foreground and background sequences. The homogeneity conditions last approximately 1 year. During the rest of time, the stress directions remain approximately constant.

2.4.2 Stress Changes as a Function of Space

All 386 earthquakes which occurred in the main thrust zone, not counting the aftershock sequences of both 1964 and 1986 mainshocks, are used for analyzing the segmentation of the Aleutian arc for the time interval from 1964 to 1993. The earthquakes are ordered from the west (from about 170°E) to the east till about 145°W . Their epicenters and the cumulative misfit are shown in the upper and lower plots of Figure 2.3, respectively. It is noted that the abscissa of the lower plot is in units of event numbers, which produce a variable distance scale. In order to identify the geographic locations of data segments in the lower plot, dashed lines connect some points of the two distance scales. In the cumulative misfit curve we notice that differences in slope (mean misfit) exist but that within segments the slope is fairly constant. This is consistent with our hypothesis that the stress tensor orientation is constant within segments of the plate boundary and that differences between segments can be measured quantitatively. The statistical significance levels of the differences in mean misfit between neighboring segments are also shown in Figure 2.3.

The most significant change of the slope of the cumulative misfit (Figure 2.3) takes place near earthquake number 45, which corresponds to a longitude of about

177.5°E. The second most significant change of the slope occurs near 149°W longitude and corresponds to the earthquake number 375, approximately. The mean misfits of the segment west of 177.5°E and the one east of 149°W are different at the 99% level from any segment of the sequence, and these segments are apparently separated from the rest by the two most pronounced boundaries. We will call them boundaries A1 and A2. Between A1 and A2, there exists an additional highly significant (99% confidence) boundary, A3, which is located near 173°W (event 218).

The region between A3 and A2 can be divided by four additional boundaries, named B1, B2, B3, and B4, with significance levels ranging from 90% to 95%. B2 corresponds to the eastern end of the 1957 aftershock zone, B1 is about 100 km west of B2, B3 is the eastern end of the Unalaska gap, and B4 is located in the middle of the Shumagin gap.

The slope in the cumulative misfit plot for the area between A1 and A3 is quite constant, except for a transition zone defined by the boundaries B5 and B6. These two boundaries correspond to the western edge of the 1986 earthquake.

We also tested whether or not the stress segmentation changes with time. The number of data points does not allow division into more than two sets: we examined separately the data before and after the 1986 main shock. The analysis for the period between 1964 and 1986 indicated that B7 is an additional segment boundary (Figure 2.4). The results for the interval from 1986 to 1993 show B8 is a boundary (Figure 2.4).

Based on the above analyses, we conclude that essentially the same segmentation is derived from the entire data set and from the sets of two time intervals. Thus temporal changes, other than those due to major aftershock sequences discovered above, do not exist in the stress regime, and we may use the entire data set as the most representative sample.

2.4.3 Stress Segmentation Sensitivity to the Reference Stress Model

We analyzed the cumulative misfit plots by choosing several different reference stress models. As our method is based on the changes of stress direction and as the relationship between misfits and stress models is nonlinear, it is possible that some of the segment boundaries do not show up relative to a particular reference stress tensor. We used the following four reference stress models to investigate the changes of slopes of cumulative misfit curves, model 1: $\sigma_1 = 6/352$, $\sigma_2 = 0/82$, $\sigma_3 = 84/175$ (plunge and azimuth, respectively), and $R = 0.2$; model 2: $\sigma_1 = 30/156$, $\sigma_2 = 4/63$, $\sigma_3 = 60/326$, and $R = 0.6$, which is the same reference stress model used to estimate the segmentation boundaries A1 to A3 and B1 to B8 (Figure 2.4); model 3: $\sigma_1 = 57/155$, $\sigma_2 = 17/233$, $\sigma_3 = 27/12$, and $R = 0.9$; model 4: $\sigma_1 = 2/49$, $\sigma_2 = 4/139$, $\sigma_3 = 86/291$, and $R = 0.4$. These stress tensors are derived by inverting four patches of homogeneous earthquake focal mechanism data along the Aleutians. Figure 2.5 is the cumulative misfit angle as a function of earthquake number for the four reference stress tensors. We use 0, 1, and 2 to rank the significance of the segmentation from no boundary, to weak boundary, and to strong boundary (Figure 2.5).

A new boundary, B9 (Figure 2.5), not found by using stress model 2, was picked up by reference stress models 1, 3, and 4. Using model 1 as the reference stress tensor, we found a boundary B10 (Figure 2.5). B9 is located at Amchitka Pass, the segment boundaries between the aftershock zones of 1957 and 1965 earthquakes (Figure 2.1). B10 is the location where the aftershock zones of 1964 and 1938 abut (Figure 2.1).

It seems that our method is not robust enough to define all the stress segmentation boundaries by employing only one reference stress tensor. By comparing

cumulative misfit curves, we also found that the location of segment boundaries shifts by approximately five earthquakes, which may correspond to several to tens of kilometers in distance.

2.4.4 Confirmation of Segment Boundaries by Stress Inversion in Moving Windows

We performed stress inversions in a moving window along the strike of the Aleutian arc to check on the reliability of the segmentation boundaries derived based on the cumulative misfit curves. This method is based on the assumption that average misfit angles will become bigger if the segmentation boundaries fall within the window. Therefore the segmentation boundaries should be near the peaks of curves of average misfit versus window position. The procedure of stress inversion in a moving window is as follows. The focal mechanism data are inverted using FMSI codes for earthquakes within the window. The average misfit angle is determined, and the window is advanced by one earthquake along the strike of the arc.

Figure 2.6 shows the average misfit angle as a function of position of the moving window for three different window lengths, 17, 25, and 31 (Figures 2.6a, 2.6b, and 2.6c, respectively). The three curves in Figure 2.6 have similar features and trends. There are five major peaks, which correspond to segment boundaries A1, B6, A3, B3, and A2.

The inversion of subsets in many parts of the Aleutians leads to very low average misfits $1.8^\circ \leq F \leq 3^\circ$. We made the reasonable assumption that the quality of focal mechanisms is constant throughout our data set and interpret inversions resulting in $F > 3^\circ$ as being partially contaminated by stress heterogeneity. The clearest peaks of average misfit in Figure 2.6 are those confirming boundaries B3 and A2. The increased value of F is also very clear at boundaries B6 and A3 when

compared with the segment between these two boundaries. The boundary A1, which is clearly defined by the cumulative misfit curves, shows the most poorly developed peak in Figure 2.6. The high level of F in the segment between A3 and B3 suggests a relatively high level of heterogeneity exists in that segment.

Based on the analyses of cumulative misfit curves and stress inversion in a moving window, we propose that there exist five first-order boundaries, A1, B6, A3, B3, and A2, along the strike of Aleutian arc (Figure 2.6). A further subdivision is composed of several second-order boundaries, B9, B5, B8, B1, B2, B4, B7, and B10, from west to east in the study region. The terms of first-order and second-order refer to our ability to resolve the presence of the boundary; however, they may not necessarily describe the degree of tectonic significance.

2.4.5 Principal Stress Orientation

The Aleutian arc can be divided into five major segments based on the locations of first-order boundaries (Figure 2.6 and 2.7): the first is from 170°E to boundary A1, the second is from boundary A1 to B6, the third is from B6 to A3, the fourth is from A3 to B3, and the last is from B3 to A2. Segments 2, 3, 4, and especially segment 5 can be further divided into several subsegments.

The inversion algorithm by *Gephart* [1990] is used to find a best fitting principal stress tensor expressed by the plunges and azimuths of the three principal stresses and the relative magnitude of the principal stresses, R . The 95% confidence areas are derived based on the one-norm misfit statistics [*Gephart and Forsyth*, 1984; *Gephart*, 1990].

The orientations of the principal stresses for the five major segments are shown in Figure 2.7 and listed in Table 1. The P and T axes of the focal mechanisms used to invert the stress orientations are shown in Figure 2.4. In segment 1, the greatest

principal stress strikes almost north-south horizontally, and the least principal stress plunges vertically. The 95% confidence region of the greatest principal stress is completely resolved from that of the least principal stress. In segment 2, the greatest principal stress has similar orientation to that in segment 1. The direction of least principal stress changes from vertical in segment 1 to horizontal in segment 2. The 95% confidence region of the least principal stress is resolvable from that of the greatest principal stress but not from the intermediate principal stress. The greatest principal stress in segment 3 shows an azimuth similar to that in segment 2 but with a steeper plunge of 25° . The orientation of the least principal stress cannot be resolved from that of the intermediate stress at the 95% level. The greatest principal stress in segment 4 shows the same azimuth as that in segment 3 but a much steeper plunge of 57° . The least principal stress is resolved from the intermediate principal stress at the 95% confidence level. The greatest principal stresses in segment 5 are not well constrained. The least principal stress is oriented vertically, but the 95% confidence regions of the greatest and the intermediate stress overlap.

2.5 Discussion

The method of plotting the cumulative misfit as a function of space along arc has been used to investigate the segmentation of the Aleutian main thrust zone. The dependence of the results on the stress model used to calculate misfit was investigated. The overall best fitting stress tensor is not suitable for our method because it evenly distributes errors among all segments. We find that seven of the boundaries are identified using the stress tensors best fitting four homogeneous segments. Five additional boundaries are only defined using some of the stress models. We conclude that we cannot be certain that we have found all existing

boundaries in stress directions, but the locations of change found by our method represent real boundaries. At these boundaries the stress directions either change or at least the tectonic style goes from one of homogeneous to relatively heterogeneous stress directions. We confirm the conclusion by *Wyss and Lu* [1995] that some segmentation of plate boundaries can be mapped by the cumulative misfit method.

The significance levels based on the z test or t test can be used to measure the degree to which the two neighboring segments are different. The results of the inversion of focal mechanism data by a moving window analysis further demonstrate the success of our method. The principal stress orientations from the inversions of focal mechanism data (Figure 2.7) agree with the results from maximum horizontal stress trajectories by some researchers [e.g., *Nakamura et al.*, 1977; *Nakamura and Uyeda*, 1980; *Estabrook and Jacob*, 1991] and are generally consistent with the direction of convergence between the Pacific and North American plates.

The idea that the large-scale structural features on the oceanic plates may have profound effects on the subduction process was proposed by several researchers [e.g., *Vogt et al.*, 1976; *Kelleher and McCann*, 1976; *House and Jacob*, 1983]. One of the significant factors that affects the subduction process of the Aleutian arc may be the fracture zones in the Pacific plate. There are several fracture zones in the study area. They are the Rat, the Adak, the Amlia, the Aja, and two unnamed fracture zones north of the Aja fracture zone (Figure 2.7). The delineation of the fracture zones is mainly based on the magnetic anomalies and sometimes on the bathymetric topography in the Pacific plate.

The Rat fracture zone offsets the magnetic anomalies about 80 km left laterally at a trough along 177.7°E [*Erickson et al.*, 1970; *Rea and Dixon*, 1983]. The northward projection of the Rat fracture zone intersects the Aleutian arc at the location of boundary A1 in the segmentation analysis (Figure 2.7).

The Adak fracture zone trends north-south with an axis at about 177.4°W , as indicated by the bathymetric and magnetic anomaly data [*Grim and Erickson*, 1969; *Rea and Dixon*, 1983]. Magnetic anomaly profiles across the Adak fracture zone show an apparent left lateral offset of about 30 km. The northern projection of the Adak fracture zone, which lies just east of Adak canyon, separates regions of strikingly different topography. For example, the seafloor east of the canyon is relatively smooth, whereas the seafloor to the west is chaotic and deeply incised by canyons [*Perry and Nichols*, 1965]. The Adak fracture zone intersects the Aleutian arc in the transition zone defined by boundary B6 in our segmentation.

The Amlia fracture zone intersects the Aleutian trench near 173.2°W (Figure 2.7). It offsets the magnetic anomalies of the Pacific plate about 220 km in a left lateral sense [*Hayes and Heirtzler*, 1968; *Grim and Erickson*, 1969]. Both the volcanic line (on the overriding plate) and the subducting plate (oceanic plate) are offset horizontally by about 40 km in a right-lateral sense near the downdip projection of the Amlia fracture zone [*House and Jacob*, 1983]. Seismicity studies by *Engdahl et al.* [1982] support the existence of this feature, since east of about 176°W the intermediate-depth seismic zone becomes progressively more offset to the south of the volcanic line as longitude 173°W is approached. *House and Jacob* [1983] suggest that as the offset of the downgoing plate moves slowly westward, it may cause a mass deficiency between the subducting slab and the overriding plate. This may cause both an upwelling of the asthenosphere above the slab and the subsidence in the overriding lithosphere, explaining the occurrence of the summit basins and a 40-km offset in the volcanic arc. Another result of the mass deficiency and subsidence may be a temporary decrease in coupling between the subducting and overriding plates along the main thrust zone such that the seismicity in the main thrust zone may temporarily (of the order of a few million years) decrease or disappear. Figure 2.4 shows that the main thrust zone between 171.5°W and

173°W currently lacks moderate-sized earthquakes and suggests that this area may experience aseismic slip because of the reduced coupling. The northward projection of the Amlia fracture zone lies at the western margin of the wide boundary A3 formed in our segmentation analysis.

The Aja fracture zone is oriented east-west and offsets the magnetic anomalies about 150 km left laterally [Naugler and Wageman, 1973; Owen, 1983] (Figure 2.7). The westward projection of the Aja fracture zone may intersect the subduction zone in the middle of the 1938 aftershock zone and corresponds to the boundary B7 in our segmentation. However, the location of the Aja fracture zone by Naugler and Wageman [1973] is different than that by Owen [1983]; thus we are not confident on the relationship between boundary B7 and Aja fracture zone. There exist two unnamed fracture zones intersecting the plate boundary in the 1964 rupture area [Naugler and Wageman, 1973; Owen, 1983] (Figure 2.7). Both of these strike east-west and are left lateral. The arc segment between the intersection of these two fracture zones is an area lacking moderate-sized earthquakes and it coincides with our wide boundary A2.

The amplitudes of the magnetic anomalies are sharply reduced where the fracture zones intersect the trench, resulting in a 100-km-wide magnetically "quiet zone" over most of the Aleutian trench and terrace [Hayes and Heirtzler, 1968; Grim and Erickson, 1969]. Because of the quiet zone, we cannot be certain that these fracture zones continue all the way into the trench, and our correlation may not be correct. However, Lonsdale [1988] suggested that the Amlia fracture zone actually extends north to underlie the Aleutian arc, and Mogi [1969] recognized an influence of the fracture zone in the pattern of the 1957 earthquake's aftershock sequence, although Sykes [1971] emphasized that the Amlia fracture zone did not act as a boundary for the rupture zone of this event.

We conclude that some major boundaries in the stress orientation may be con-

trolled by fracture zones in the subducting plate. This may result from topographic irregularities and the age difference of the seafloor across the fracture zones.

The boundaries defined by our method may also be related to the asperity distributions of the great earthquakes. The asperities considered here refer to the area of highest seismic moment release, assumed to be the strongest coupling between the subducted and the overriding plate [e.g., *Ruff and Kanamori*, 1983; *Beck and Christensen*, 1991; *Dmowska and Lovison*, 1992; *Christensen and Beck*, 1994; *Johnson et al.*, 1994].

The seismic moment release of the 1938 earthquake is concentrated in the eastern half of the aftershock zone (Figure 2.7) [*Johnson and Satake*, 1994], that is, east of B7 of our segmentation. The eastern boundary of the 1938 aftershock zone corresponds to B10 of our segmentation boundary. B10 is poorly defined in our analysis, which may be attributed to the limited earthquake focal mechanism data in the 1938 aftershock zone area. The existence of B10 supports the conclusion that there is a tectonic boundary between the 1964 and 1938 earthquake where the aftershock zones of the two earthquakes abut [e.g., *Sykes*, 1971; *Christensen and Beck*, 1994].

The asperity areas of the 1957 main shock (modified from *Johnson et al.* [1994]), are shown in Figure 2.7. The aftershock zone of 1957 is separated into two segments by the Amlia fracture zone, which is also the boundary A3 of our result. Most of the moment release was concentrated in the western half of the aftershock zone based on the surface and tsunami wave inversion [*Johnson et al.*, 1994], which is therefore the biggest asperity area of this earthquake. There is also another small asperity between 169°W and 168°W. The western end of the larger asperity is B9 of our analysis. The existence of B9 may also support the idea that the Amchitka Pass played an important role in ending the ruptures of 1965 and 1957 earthquakes [e.g., *Stauder*, 1972; *Ryan and Scholl*, 1993]. The eastern end of the second asperity

is approximately defined by boundary B1, which is also the location suggested by *Johnson et al.* [1994] as the end of the 1957 rupture. Boundary B2 in the stress direction corresponds to the eastern end of the aftershock zone.

The 1964 earthquake had two major asperities, separated by a gap of about 200 km [*Christensen and Beck*, 1994]. The boundary A2 in our analysis clearly separates the two asperity areas (Figure 2.5).

There are three major asperities in the 1965 rupture process (Figure 2.7). The largest and first asperity extends from the epicenter to 100 km to the WNW [*Beck and Christensen*, 1991]. The boundary A1 corresponds to the west end of the largest asperity. The second pulse of moment release is jagged and is less coherent between stations. The last resolvable asperity extends from 360 to 420 km WNW of the epicenter. Both the second and the last asperity boundaries cannot be resolved by our analysis.

The aftershock zone of the 1986 earthquake extends to boundary A3 to the east and boundary B6 to the west (Figure 2.7). Most of the moment release of the 1986 earthquake was generated in the neighboring regions of the epicenter, and very little moment was released near the epicenter of the main shock [*Yoshida*, 1992; *Das and Kostrov*, 1990; *Hwang and Kanamori*, 1986; *Boyd and Nabelek*, 1988]. The boundary B8 separates the two major asperity areas of the 1986 rupture (Figure 2.7).

Boundary B4 lies in the middle of the Shumagin seismic gap, which may suggest that the west and east of the Shumagin gap may behave differently [e.g., *Lu et al.*, 1994]. This supports the hypothesis that the Shumagin gap can be divided into western and eastern parts based on the transition from double to single Wadati-Benioff seismic zone [*Hudnut and Taber*, 1987].

The transverse canyons in the western Aleutians (Figure 2.1) trend nearly at right angles to the regional slip vector of the plate motion. *Gates and Gibson*

[1965] provided some geologic evidence to show that all the transverse canyons are not of erosional origins. The Adak canyon is one of the most prominent canyons and is the only one which correlates with a stress boundary. *LaForge and Engdahl* [1979] studied small magnitude earthquakes in the wedge-shaped zone above the main thrust zone in the Adak canyon region. Evidence from the focal mechanisms for normal faulting in the wedge led them to conclude that Adak canyon is a block-fault structure caused by lateral extension of the overriding plate. However, *Spence* [1977] suggested that the Adak canyon is the result of the existence of the topographic relief of the Adak fracture zone. We suggest that the transverse canyons might be tectonic in origin but may be related to the curvature of the western Aleutian trench with respect to the slip direction of the subducted plate as the canyons are generally absent in the Aleutian arc east of 177°W . The canyons may also be related to the earthquakes in the upper plate and do not significantly affect processes in the main thrust zone. This may be the reason why these canyons appear not to influence the stress directions.

2.6 Conclusions

The method of plotting the cumulative misfit as a function of earthquake numbers, which are ordered in space, is proposed for investigating the stress homogeneity of the Aleutian arc. Using this method, one can divide the area into subareas where the stresses are homogeneous. We conclude that the aftershock sequences of the 1964 and 1986 events appear more homogeneous than those of the foreground and background sequences, based on the analysis of slip vector misfits as a function of time. The homogeneity condition of the aftershock sequence (sometimes also containing several preshocks) lasts approximately 1 year.

The cumulative misfit as a function of earthquake number along the strike of

the arc shows that the Aleutian arc (from 170°E to 145°W) can be divided into five major segments. The focal mechanism data in the stress-homogeneous segments are then used to invert the principal stress orientations using FMSI computer codes of *Gephart* [1990]. The stress inversion analysis in a moving window and the orientations of the principal stresses in the five segments support the feasibility of our method.

We considered the correlation of the stress boundaries with four other tectonic features: fracture zones, submarine canyons, ends of the aftershock zones of great ruptures, and asperities. The strongest correlation seems to exist between fracture zones and stress direction changes. This may be interpreted as indicating a decoupling within the underthrusting plate along the zones of weakness (the fracture zones) across which stress may not be transmitted fully. The correlation of morphological features, such as canyons, with stress discontinuities is weakest. This suggests that most of the canyons may not influence the process in the lower crust. Further, a fairly strong correlation of asperities and ends of ruptures with location of stress discontinuity is observed.

2.7 References

- Angelier, J., Determination of the mean principal directions of stresses for a given fault population, *Tectonophysics*, 56, T17-T26, 1979.
- Beck, S. L., and D. H. Christensen, Rupture process of the February 4, 1965, Rat Islands earthquake, *J. Geophys. Res.*, 96, 2205-2221, 1991.
- Bott, M. H. P., The mechanics of oblique slip faulting, *Geol. Mag.*, 96, 109-117, 1959.
- Boyd, T. M., and J. L. Nabelek, Rupture process of the Andreanof Islands earthquake of May 7, 1986, *Bull. Seismol. Soc. Am.*, 78, 1653-1673, 1988.

- Bufe, C. G., S. P. Nishenko, and D. J. Varnes, Seismicity trends and potential for large earthquakes in the Alaska-Aleutian region. *Pure Appl. Geophys.*, 142, 83-99, 1994.
- Christensen, D. H., and S. L. Beck, The rupture process and tectonic implications of the great 1964 Prince William Sound earthquake, *Pure Appl. Geophys.*, 142, 29-53, 1994.
- Das, S., and B. V. Kostrov, Inversion for seismic slip rate history and distribution with stabilizing constraints: Application to the 1986 Andreanof Islands earthquake. *J. Geophys. Res.*, 95, 9-6913, 1990.
- Davies, J., L. Sykes, L. House, and K. Jacob, Shumagin seismic gap, Alaska peninsula: History of great earthquakes, tectonic setting, and evidence for high seismic potential, *J. Geophys. Res.*, 86, 3821-3855, 1981.
- Dmowska, R., and L. C. Lovison, Influence of asperities along subduction interfaces on the stressing and seismicity of the adjacent areas. *Tectonophysics*, 211, 23-43, 1992.
- Ekstrom, G., and E. R. Engdahl, Earthquake source parameters and stress distribution in Adak Island region of the central Aleutian Islands, Alaska. *J. Geophys. Res.*, 94, 15,499-15,519, 1989.
- Engdahl, E. R., J. W. Dewey, and S. Billington, Evidence for contortion of the subducted plate in the central Aleutians (abstract). *Eos Trans. AGU*, 63, 439, 1982.
- Erickson, B. H., F. P. Naugler, and W. H. Lucas, Emperor fracture zone: A newly discovered feature in central North Pacific, *Nature*, 225, 53-54, 1970.
- Estabrook, C. H., and K. H. Jacob, Stress indicators in Alaska, in *Decade Map, Vol. 1, Neotectonics of North America*, edited by D. B. Slemmons, E. R. Engdahl, N. D. Zoback, and D. D. Blackwell, pp. 387-399, Geol. Soc. of Am., Boulder, Colo., 1991.

- Gates, O., and W. Gibson, Interpretation of the configuration of the Aleutian arc. *Geol. Soc. Am. Bull.*, 67, 127-146, 1965.
- Geist, E. L., J. R. Childs, and D. W. Scholl, The origin of summit basins of the Aleutian Ridge: Implications for block rotation of an arc massif. *Tectonics*, 7, 327-341, 1988.
- Gephart, J. W., FMSI: A FORTRAN program for inverting fault/slickenside and earthquake focal mechanism data to obtain the original stress tensor. *Comput. and Geosci.*, 16, 953-989, 1990.
- Gephart, J. W., and D. W. Forsyth, An improved method of determining the regional stress tensor using the earthquake focal mechanism data: Application to the San Fernando earthquake sequence. *J. Geophys. Res.*, 89, 9305-9320, 1984.
- Gillard, D., and M. Wyss, Comparison of strain and stress tensor orientation: Application to Iran and southern California. *J. Geophys. Res.*, in press, 1995.
- Grim, P. J., and B. H. Erickson, Fracture zones and magnetic anomalies south of the Aleutian trench, *J. Geophys. Res.*, 74, 1488-1494, 1969.
- Hayes, D. E., and J. R. Heirtzler, Magnetic anomalies and their relation to the Aleutian Island Arc, *J. Geophys. Res.*, 73, 4637-4646, 1968.
- House, L. S., and K. H. Jacob, Earthquakes, plate subduction, and stress reversals in the eastern Aleutian arc. *J. Geophys. Res.*, 88, 9347-9373, 1983.
- Hudnut, K. W., and J. J. Taber, Transition from double to single Wadati-Benioff seismic zone in the Shumagin Islands, Alaska. *Geophys. Res. Lett.*, 14, 143-146, 1987.
- Hwang, L. J., and H. Kanamori, Of the May 7, 1986 Andreanof Islands earthquake source parameters. *Geophys. Res. Lett.*, 13, 1426-1429, 1986.
- Johnson, J. M., and K. Satake, Rupture extent of the 1938 Alaskan earthquake as inferred from tsunami waveforms, *Geophys. Res. Lett.*, 21, 733-736, 1994.
- Johnson, J. M., Y. Tanioka, L. J. Ruff, K. Satake, H. Kanamori, and L. R. Sykes,

- The 1957 Great Aleutian earthquake. *Pure Appl. Geophys.*, 142, 3-28, 1994.
- Kelleher, J., and W. McCann. Buoyant zones, great earthquakes, and unstable boundaries of subduction. *J. Geophys. Res.*, 81, 4885-4896, 1976.
- LaForge, R., and E. R. Engdahl. Tectonic implication of seismicity in the Adak Canyon region, central Aleutians, *Bull. Seismol. Soc. Am.*, 69, 1515-1532, 1979.
- Lonsdale, P.. Paleogene history of the Kula plate: Offshore evidence and onshore implications, *Geol. Soc. Am. Bull.*, 100, 733-754, 1988.
- Lu, Z., M. Wyss, and S. Wiemer, Recent seismicity in and around the Shumagin-Unalaska seismic gap, Alaska (abstract), *Seismol. Res. Lett.*, 65, 33, 1994.
- McKenzie, D. P.. The relationship between fault plane solutions for earthquakes and the directions of the principal stresses. *Bull. Seismol. Soc. Am.*, 59, 591-601, 1969.
- Michael, A. J., Use of focal mechanisms to determine stress: A control study. *J. Geophys. Res.*, 92, 357-368, 1987.
- Mogi, K., Relationship between the occurrence of great earthquakes and tectonic structures, *Bull. Earthquake Res. Inst. Univ. Tokyo*, 47, 429-451, 1969.
- Nakamura, K., and S. Uyeda. Stress gradient in arc-back arc regions and plate subduction, *J. Geophys. Res.*, 85, 6419-6428, 1980.
- Nakamura, K., K. H. Jacob, and J. N. Davies. Volcanoes as possible indicators of tectonic stress orientation - Aleutians and Alaska. *Pure Appl. Geophys.*, 115, 87-112, 1977.
- Naugler, F. P., and J. M. Wageman. Gulf of Alaska: Magnetic anomalies, fracture zones, and plate interactions. *Geol. Soc. Am. Bull.*, 84, 1575-1584, 1973.
- Newberry, J. T., D. L. Laclair, and K. Fujita, Seismicity and tectonics of the far western Aleutian Islands. *J. Geodynamics*, 6, 13-32, 1986.
- Nishenko, S. P., and K. H. Jacob, Seismologic potential of the Queen Charlotte-Alaska-Aleutian seismic zone, *J. Geophys. Res.*, 95, 2511-2532, 1990.

- Nishenko, S. P., and W. R. McCann, Seismologic potential for the world's major plate boundaries, in *Earthquake Prediction—An International Review, Maurice Ewing Ser., Vol. 4*, edited by D. W. Simpson, and P. G. Richards, pp. 20-28. AGU, Washington, D.C., 1981.
- Owen, H. G., *Atlas of Continental Displacement. 200 Million Years to the Present*. 159 pp., Cambridge Univ. Press, New York, 1983.
- Perry, R. B., and H. Nichols. Bathymetry of Adak canyon, Aleutian arc, Alaska. *Bull. Geol. Soc. Am.*, *76*, 365-370, 1965.
- Rea, D. K., and J. M. Dixon. Late cretaceous and Paleogene tectonic evolution of the north Pacific Ocean. *Earth Planet. Sci. Lett.*, *64*, 67-73, 1983.
- Ruff, L., and H. Kanamori. The rupture process and asperity distribution of three great earthquakes from long-period diffracted P-waves. *Phys. Earth Planet. Inter.*, *31*, 202-230, 1983.
- Ryan, H. F., and D. W. Scholl. Geological implications of great interplate earthquakes along the Aleutian arc. *J. Geophys. Res.*, *98*, 22,135-22,146, 1993.
- Spence, W., The Aleutian arc: Tectonic blocks, episodic subduction, strain diffusion, and magma generation. *J. Geophys. Res.*, *82*, 213-230, 1977.
- Stauder, W., Mechanism of the Rat Island earthquake sequence of February 4, 1965, with relation to island arcs and sea-floor spreading, *J. Geophys. Res.*, *73*, 3847-3858, 1968a.
- Stauder, W., Tensional character of earthquakes foci beneath the Aleutian trench with relation to sea-floor spreading, *J. Geophys. Res.*, *73*, 7693-7701, 1968b.
- Stauder, W., Fault motion and spatially bounded character of the earthquakes in Amchitka Pass and the Delarof Islands, *J. Geophys. Res.*, *77*, 2072-2080, 1972.
- Stauder, W., and G. A. Bollinger. The focal mechanism of the Alaska earthquake of March 28, 1964, and of its aftershock sequence, *J. Geophys. Res.*, *71*, 5283-5296, 1966.

- Stauder, W., and A. Udias, S-wave studies of earthquakes of the North Pacific. II. Aleutian Islands. *Bull. Seismol. Soc. Am.*, *53*, 59-77, 1963.
- Sykes, L. R., Aftershock zones of great earthquakes, seismicity gaps, and earthquake prediction for Alaska and Aleutians. *J. Geophys. Res.*, *76*, 8021-8041, 1971.
- Taber, J. J., S. Billington, and E. R. Engdahl. Seismicity of Aleutian Arc. in *Decade Map, Vol. 1, Neotectonics of North America*, edited by D. B. Slemmons, E. R. Engdahl, N. D. Zoback, and D. D. Blackwell, pp. 29-45. Geol. Soc. of Am., Boulder, Colo., 1991.
- Tichelaar, B. W., and L. Ruff. Depth of seismic coupling along the Aleutian zones. *J. Geophys. Res.*, *98*, 2017-2037, 1993.
- Vogt, P. R., A. Lowrie, D. R. Bracey, and R. N. Hey, Subduction of aseismic oceanic ridges: Effects on shape, seismicity and other characteristics of the consuming plate boundaries. *Spec. Pap. Geol. Soc. Am.*, *172*, 1-59, 1976.
- Wyss, M., and Z. Lu, Plate boundary segmentation by stress directions: Southern San Andreas fault, California. *Geophys. Res. Lett.*, *22*, 547-550, 1995.
- Wyss, M., B. Liang, W. R. Tanigawa, and X. Wu, Comparison of orientations of stress and strain tensors based on fault plane solutions in Kaoiki Hawaii. *J. Geophys. Res.*, *97*, 4769-4790, 1992.
- Yoshida, S., Waveform inversion for rupture using a non-flat seafloor model: Application to 1986 Andreanof Islands and 1985 Chile earthquakes. *Tectonophysics*, *211*, 45-59, 1992.

Table 2.1 Stress inversion results for the Aleutians

Segment	Sample Number	Greatest Stress		Intermediate Stress		Least Stress		<i>R</i>	Average Misfit
		AZ	PL	AZ	PL	AZ	PL		
I	44	352°	6°	82°	0°	175°	84°	0.2	2.8°
II	55	331°	3°	212°	83°	62°	6°	0.4	2.9°
III	109	155°	25°	64°	2°	330°	65°	0.6	3.4°
IV	73	155°	57°	273°	17°	12°	27°	0.7	3.4°
V	100	69°	3°	160°	22°	332°	68°	0.4	5.5°

AZ is azimuth; PL is plunge; *R* is ratio of relative stress magnitude (see text).

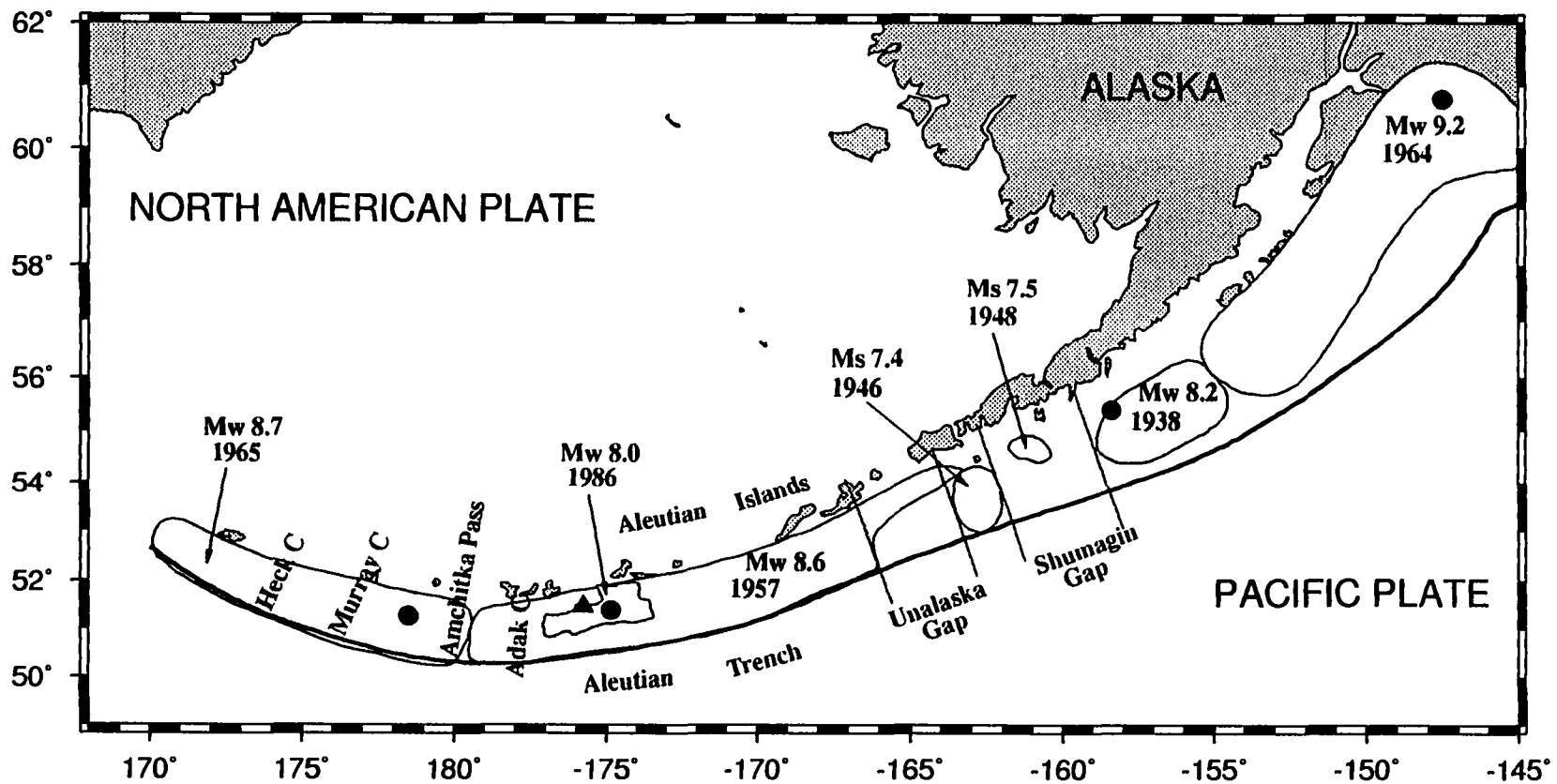


Figure 2.1 Map of aftershock areas (light shading) of earthquakes with $M_s \geq 7.4$ along the Aleutian arc from 1938 to 1986. The solid circles are the epicenters for the (from left to right) 1965, 1986, 1938, and 1964 earthquakes. The solid triangle is the epicenter of the 1957 earthquake. The lines perpendicular to the arc define the Unalaska and the Shumagin gaps. Major transverse tear canyons (C) are indicated.

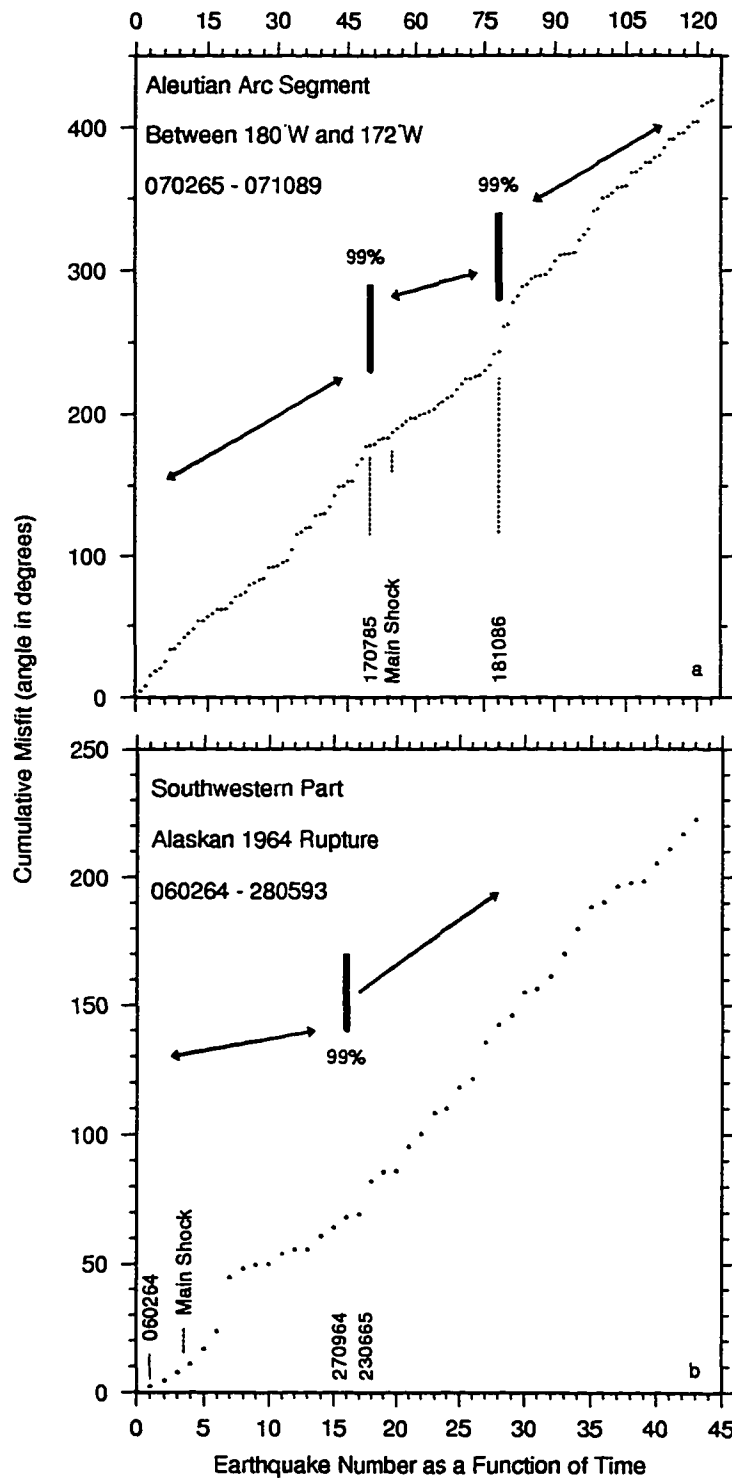


Figure 2.2 Cumulative misfit angle as a function of earthquake number (a) in the western part of the aftershock zone of the 1957 earthquake and (b) in the southwestern part of the aftershock zone of the 1964 earthquake. The earthquakes are ordered according to time. The occurrence times of several earthquakes are marked. The confidence levels at which neighboring segments are different from each other are indicated.

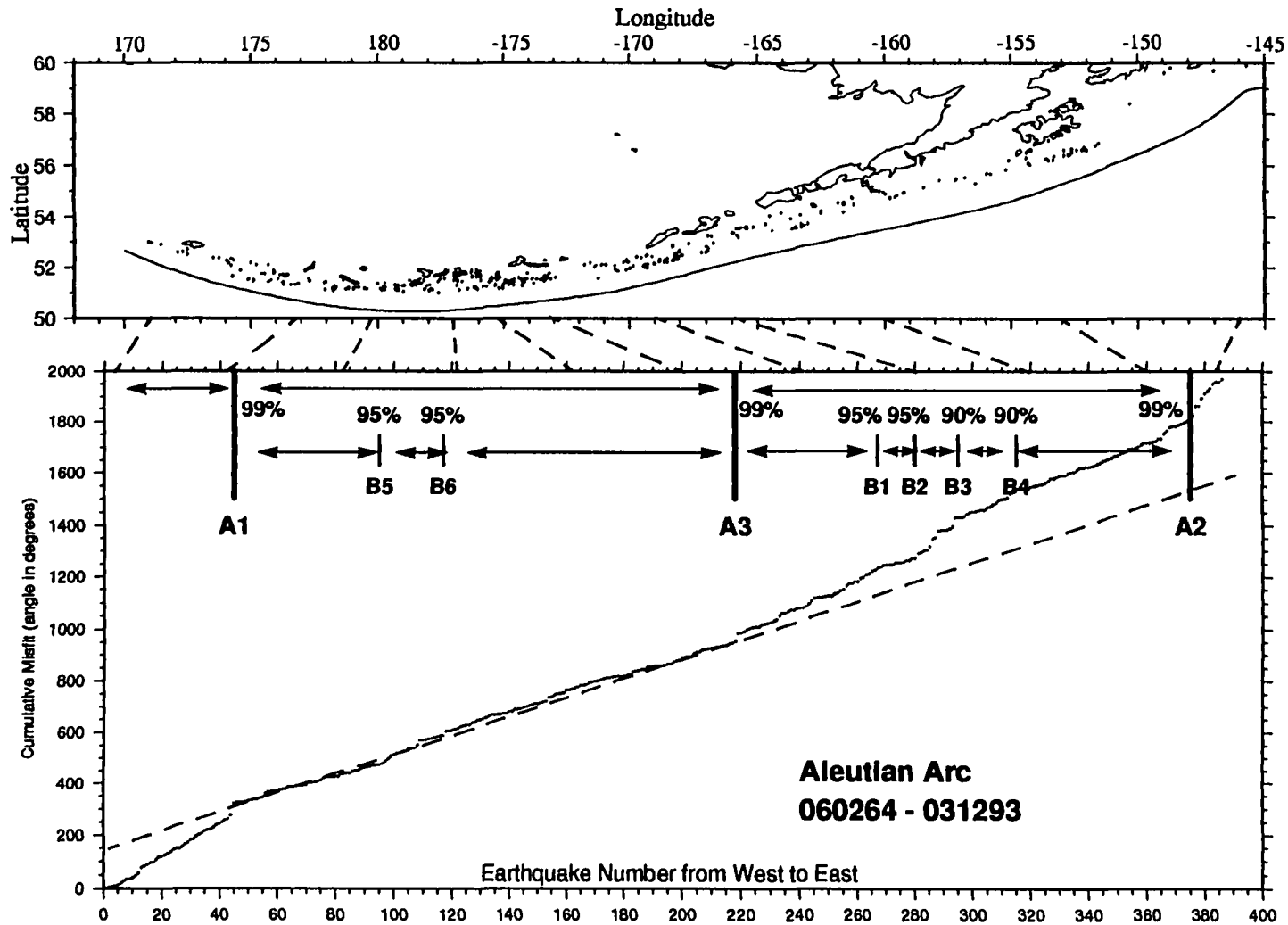


Figure 2.3 (top) The epicenters of the earthquakes are shown as dots in the upper plot. (bottom) Cumulative misfit as a function of earthquake numbers which are ordered from west to east for the time interval from 1964 to 1993 is shown. The significance levels at which the neighboring segments are different from each other are indicated in the bottom figure. Notice the abscissa of the bottom figure is in units of earthquake number while that of the top figure is in longitude. The longitude locations of event numbers 40, 80, ..., 400 are pointed out by dashed lines.

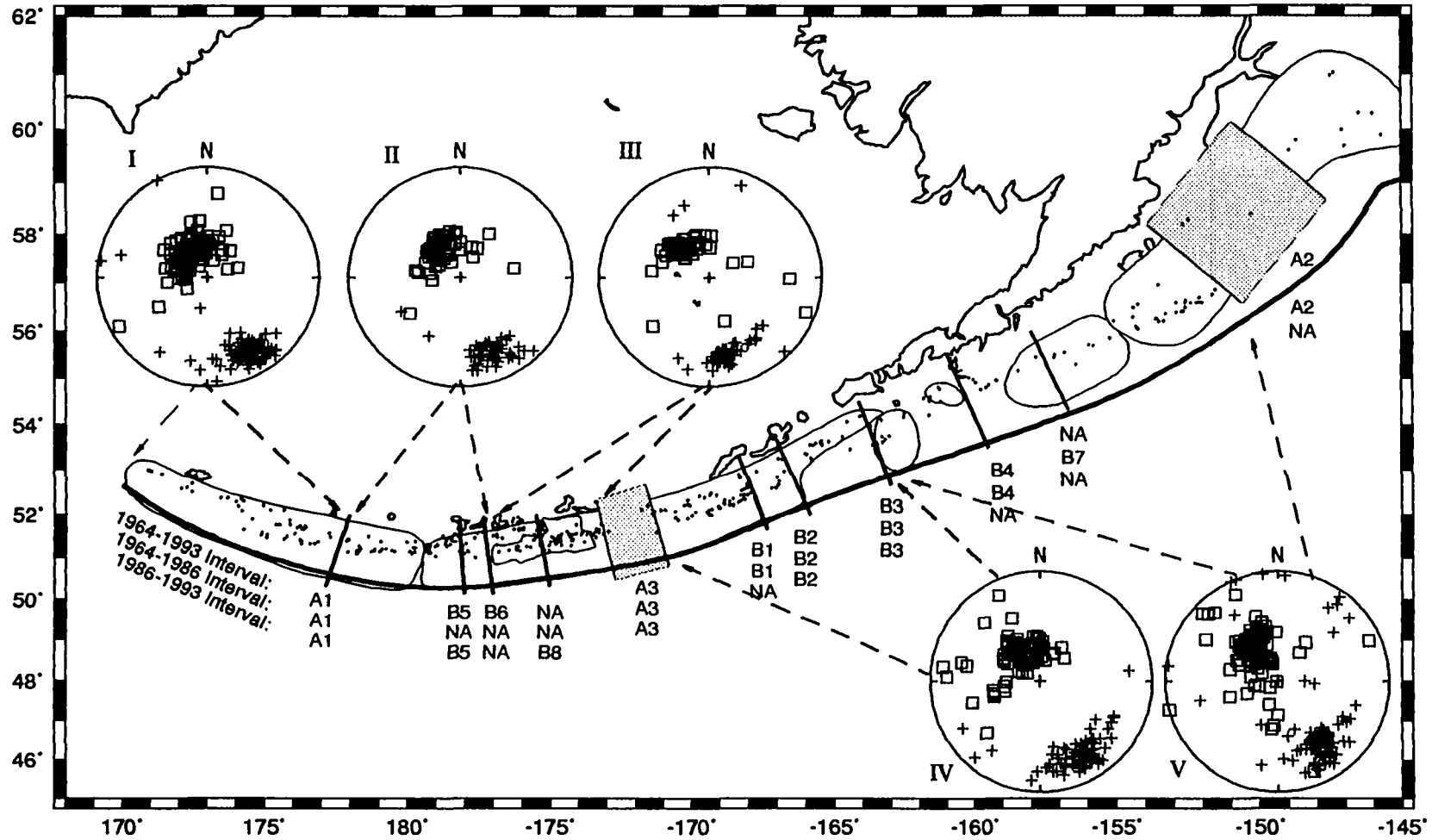


Figure 2.4 Epicenters of the earthquakes (dots) from 1964 to 1993 and segmentation boundaries of the Aleutian arc based on the stress distribution for the time intervals from 1964 to 1993, 1964 to 1986, and 1986 to 1993, respectively. The lines perpendicular to the arc indicate the boundaries of the segmentation along the Aleutian arc based on the analyses for the three time intervals and one reference stress tensor. NA means the stress boundary is not applicable for that period. The orientations of P (pluses) and T (squares) axes of the focal mechanism data in the five segments are plotted on lower hemisphere, equal-area projections.

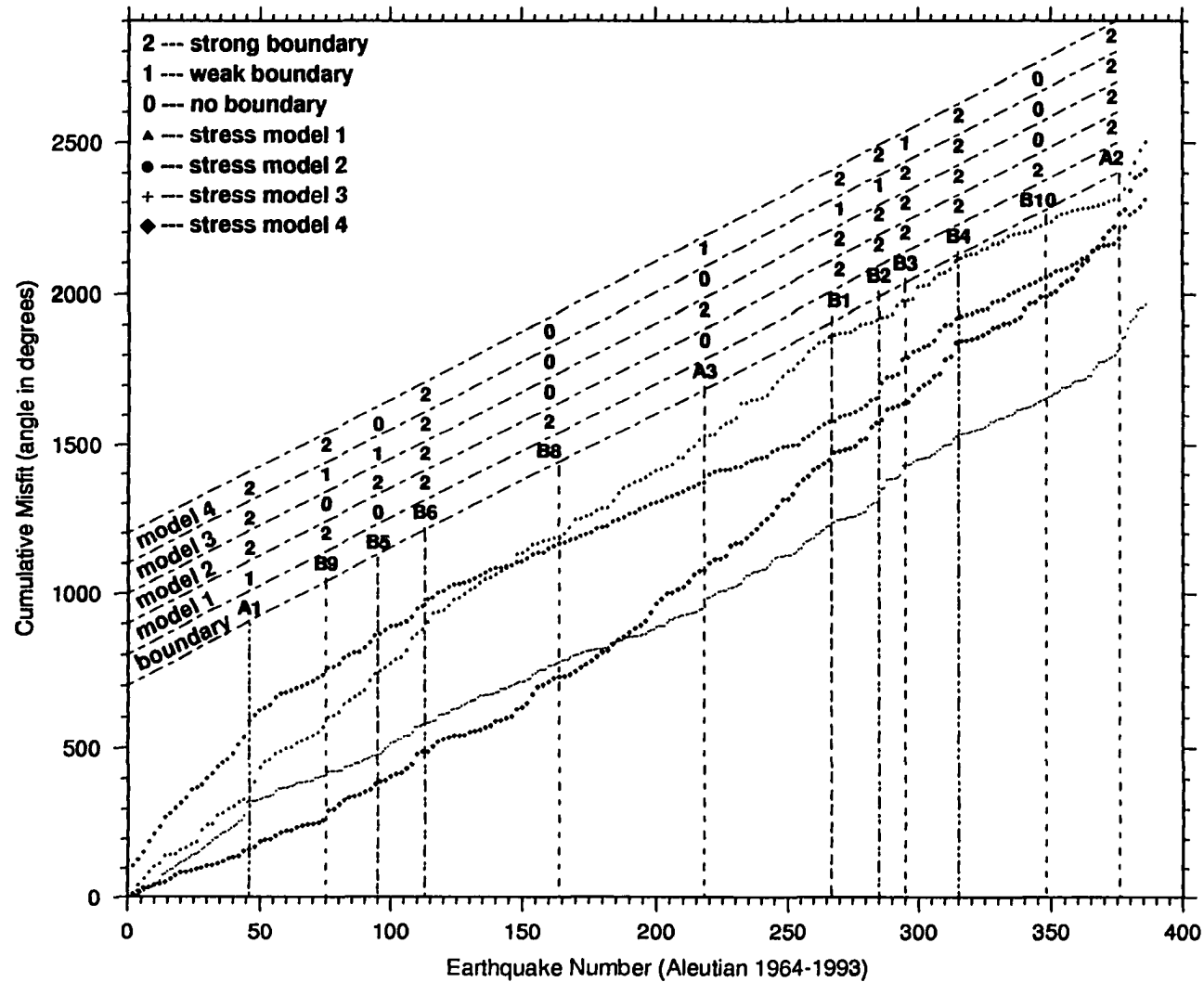


Figure 2.5 Cumulative misfit as a function of earthquake numbers for four reference stress tensors. For clarity, only the even number of earthquakes is shown in the curves with reference stress models 1, 3, and 4, while all the earthquakes are shown in that with the reference stress model 2. The significance of the segmentation, from no boundary, to weak boundary, and to strong boundary, is indicated by 0, 1, and 2, respectively.

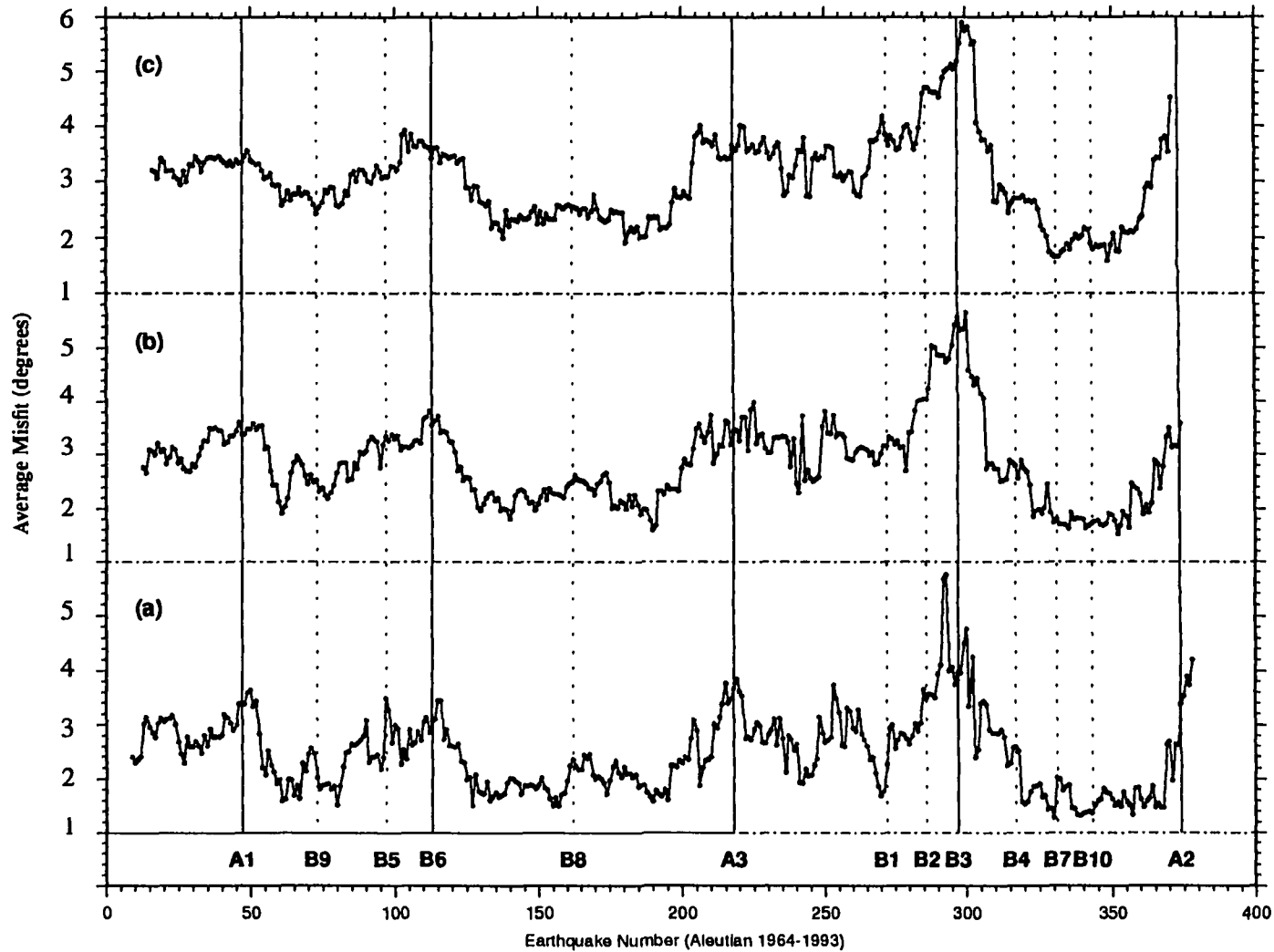


Figure 2.6 Average misfit angle for inversions for stress directions as a function of positions of the moving window for three different window lengths, (a) 17, (b) 25, and (c) 31 earthquakes. The locations of segmentation boundaries based on the analysis of cumulative misfit, A1 to A3 and B1 to B10, are shown by vertical lines. Large misfits result when events from segments with different stress directions are mixed in a window.

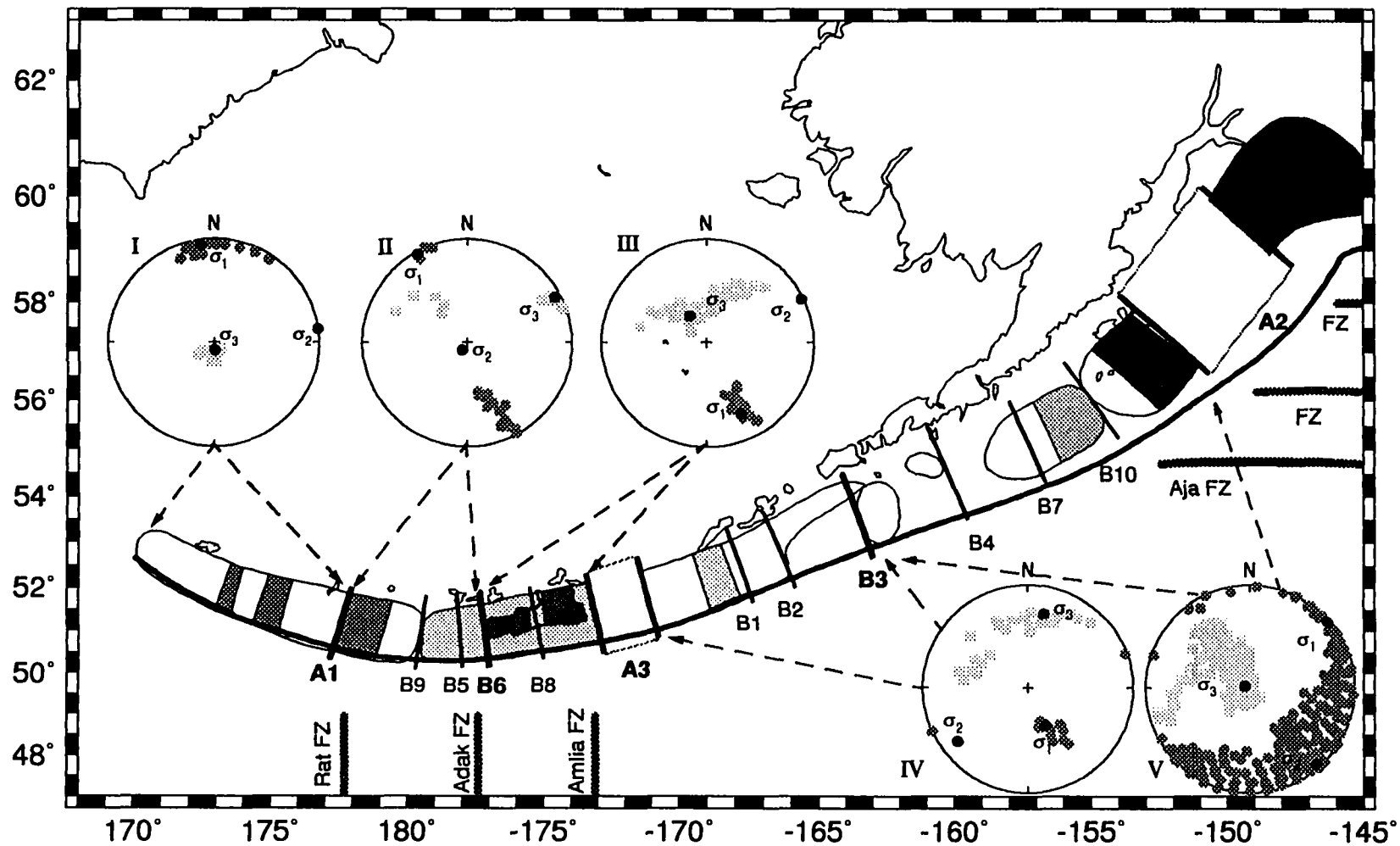


Figure 2.7 Segmentation of the Aleutian arc based on the stress distribution estimated from fault plane solutions. The lines perpendicular to the plate boundary are the segmentation boundaries. The principal stress orientations for the five major segments are plotted on lower hemisphere, equal-area projections in which the 95% confidence regions are defined by circles and squares for the greatest and least principal stress, respectively. The major fracture zones (FZ) are indicated. The shaded areas are the asperities of great earthquakes. The asperities of 1957 and 1938 earthquakes are modified from *Johnson et al. [1994]* and *Johnson and Satake [1994]*, respectively. The aftershock areas of the great earthquakes are the same as those shown in Figure 2.1.

Chapter 3

Details of Stress Directions in the Alaska Subduction Zone From Fault Plane Solutions

3.1 Abstract

We used the cumulative misfit method to divide a data set with heterogeneous stress orientations into subsets with homogeneous stress directions. The spatial locations of slope changes of the cumulative misfit as a function of earthquake number are proposed as the boundaries of homogeneous stresses. Using a synthetic data set of 50 fault plane solutions, composed of two halves corresponding to two incompatible stress tensors, we tested the validity and efficacy of the cumulative misfit method. Our acceptance criteria for results of stress tensor inversions are (1) the directions are well constrained, that is, the 95% confidence regions of

⁰This chapter contains the complete text and figures of the manuscript, Details of Stress Directions in the Alaska subduction zone from fault plane solutions stress direction estimates based on fault plane solutions, by Z. Lu, M. Wyss and H. Pulpan, as submitted to *J. Geophys. Res.*, 101, 1996.

the greatest and least principal stresses do not overlap; and (2) there is evidence for homogeneity in the sample. that is, the average misfit of the inversion is less than 6° . We estimated stress directions in the Alaska Wadati-Benioff Zone (WBZ) using 470 fault plane solutions, which we determined for earthquakes with $M_L \sim 3$ and 67 published fault plane solutions for earthquakes with $M_s \sim 5$. We succeeded in subdividing the data set of the small and large earthquakes into 25 and 3 subsets, with average misfit ranging from 3.2° to 5.5° . These results suggest that uncertainties in faulting parameters in this data set account for less than 6 of the average misfit in inversions. The average misfits of the subsets we accept as satisfying the assumption of homogeneity, are smaller than the average misfit of the overall data set ($F \sim 10^\circ$) by factors of 2 to 3. We estimated the stress fields at two scales along the Alaska WBZ. The stress directions measured by the large earthquakes ($M_s \sim 5$) were homogeneous, with extension down dip and the direction of greatest compression along strike. This unusual orientation of the greatest principal stress is attributed to the bend of the slab under central Alaska, which generates compressive stresses along strike. The stress orientations revealed by small earthquakes ($M_L \sim 3$), in contrast, exhibited a great deal of heterogeneity as a function of space, although they show a trend that confirms the overall stress directions obtained from the large events. We propose that the ratio of the dimensions of the stress field sensed by earthquakes to the rupture dimensions is about 20 to 50. The estimated stress directions of the crustal earthquakes corresponded to the following mechanisms: (1) strike-slip faulting with the greatest principal stress oriented NS near Fairbanks, and (2) thrusting with the greatest principal stress oriented NW-SE near Mount McKinley.

3.2 Introduction

In this paper, we propose to do the following:

1) Test the validity and efficacy of the cumulative misfit method proposed by *Wyss and Lu* [1995] and *Lu and Wyss* [1996], and propose criteria for accepting the stress tensor orientation estimated from inversion of fault plane solutions. The purpose of the cumulative misfit method is to define the extent of volumes with homogeneous stress directions based on the misfit of individual fault plane solutions, calculated using assumed stress tensors. Using this method *Wyss and Lu* [1995] identified the same stress boundaries as those proposed by *Jones* [1988] from tectonic considerations along the San Andreas fault from the Carrizo plains to its southern end. *Lu and Wyss* [1996] successfully found the locations of stress segmentation boundaries along the Aleutian based on this technique. However, the cumulative misfit method has not been tested quantitatively. In this paper, therefore, we will use synthetic data to test the method. We will also propose criteria for accepting the stress tensors estimated from inversion of fault plane solutions. We use the terms "meaningful" and "useful" to mean that inversion results do not violate our acceptance criteria.

2) Estimate the detailed stress directions along the Alaska WBZ, using the cumulative misfit method to subdivide the zone into sections with homogeneous stress directions. Directions of stress in subduction zones were essentially settled during the discoveries related to plate tectonics. In several papers it was shown that the fault planes of intermediate and deep earthquakes were not parallel to the Wadati-Benioff zones (WBZ) and that consistently either the P- or the T-axis (compressive and tensional bisectrices, respectively, of focal mechanisms) are oriented down-dip [e.g., *Isacks and Molnar*, 1971; *Isacks et al.*, 1968; *Bhattacharya and Biswas*, 1979; *House and Jacob*, 1983]. From this it was concluded that the

subducting slabs act as stress guides, which are either in down-dip compression or tension, depending on their length and history. Although we do not doubt that this view of the stress field in subducting slabs is essentially correct, there must be substantial deviations from this basic condition in bends of slabs (along strike as well as down-dip), as expected from detailed slab models [e.g., *Creager and Boyd*, 1991; *Creager et al.*, 1995]. In addition, perturbations of the stress directions may also exist in relatively straight slab segments as suggested by the orientations of P- and T- axes of small earthquakes or composite solutions [e.g., *Reyners and Coles*, 1982; *Matsuzawa et al.*, 1986; *Smith et al.*, 1993; *Wiens et al.*, 1993; *Comte and Suarez*, 1994; *Iguchi et al.*, 1995]. In the WBZ below Cook Inlet, for example, the T-axes of composite focal mechanisms tend to point down-dip, increasing their dip as the dip of the WBZ increases with depth [*Kissling and Lahr*, 1991; *Lahr et al.*, 1993, 1994]. Some detailed analyses of subducting slabs, which have concentrated on mapping the P- and T-axes [e.g., *Lahr et al.*, 1993, 1994; *Iguchi et al.*, 1995] found variations in these parameters. However, it is not necessarily correct to interpret the P and T axes as the directions of the greatest and least principal stress because earthquakes could occur along faults which are preexisting planes of weakness [*McKenzie*, 1969]. In a preliminary study *Li et al.* [1995] found differences in stress directions within volumes defined based on geographical distribution of hypocenters in the Alaska WBZ. In this paper we investigate the details of the stress directions in the Alaska WBZ on scales of a few tens of kilometers. We use the focal mechanisms of earthquakes, instead of P and T axes, to resolve stress directions in the slab. We apply the cumulative method [*Wyss and Lu*, 1995; *Lu and Wyss*, 1996] to define the volumes of homogeneous stress directions.

3) Compare the stress inversion results from small ($M_L \sim 3$) and large ($M_s \sim 5$) earthquakes in the same area and then investigate the scale dependency of stress

field. The scale at which directions of stress can be estimated from fault plane solutions has not been discussed in the literature. Geologists are, however, aware of this problem. For example, *Rebai et al.* [1992] in their figure 3, show how large and small faults may perturb the regional stress field and lead to locally varying stress regimes. In the meantime, a basic assumption for the inversion of fault plane solutions to estimate stress direction is that all earthquakes occur in response to a single stress tensor. Thus, if we mix fault plane solutions from volumes with different stress directions our results will be invalid, but we may not recognize this condition [e.g., *Michael*, 1987]. Therefore, it may not be advisable to mix small and large earthquakes in data sets to be inverted, even if they are located in the same area. Inverting fault plane solutions for stress directions in Sicily, *Caccamo et al.* [1996] noticed that large and small earthquakes in the same area do not always conform to the same stress tensor. One of the key questions of the scale that arises in seismology is: What is the relationship between the rupture dimensions of earthquakes and the dimensions of the stress field that generate these earthquakes? We suspect that it is not likely that ruptures along substantial segments of large faults reflect local perturbations of the stress field. Instead we expect them to respond to the large-scale, overall stress field. We define "large earthquakes" as $M_s \sim 5$, having rupture dimensions of about 10 km. The small earthquakes ($M_L \sim 3$) we describe in this investigation have source dimensions of a few hundred meters. These small earthquakes could occur in response to the overall stress field just as large earthquakes do, if they occur in volumes that are not perturbed. However, because of their small dimensions they can also reflect local perturbations of the stress field. If we have enough small earthquakes in such a volume, we may then derive the locally perturbed stress directions by inversion. Because of the limitation of the number of the earthquake focal mechanisms we have, we could only subdivide the data set into two categories with $M_s \sim 5$ and

$M_L \sim 3$, respectively. In this paper, we invert the fault plane solutions of large and small earthquakes in Alaska separately. This separation has the advantage of examining the same area at two different length scales. We subdivide the data set as a function of space, with the aim of finding homogeneous sets that define the stress directions in relatively small volumes, and ensuring that the assumption of homogeneity is fulfilled.

3.3 Stress Tensor Inversion and the Cumulative Misfit Method

3.3.1 Stress Tensor Inversion Method

To determine stress directions from fault plane solutions we use the Focal Mechanism Stress Inversion (FMSI) computer programs which were developed to find the orientation of a best fitting principal stress tensor to a group of earthquakes by grid search over a range of possible models [Gephart and Forsyth, 1984; Gephart, 1990] under the assumption that the slip on the fault plane occurs in the direction of the resolved shear stress [Bott, 1959; McKenzie, 1969] and that the stress orientation is homogeneous in the study area [e.g., Angelier, 1979; Michael, 1984; Yin and Ranalli, 1993]. The misfit for each earthquake is defined as the smallest rotation angle about an axis of any orientation that would bring the direction and sense of slip, associated with either of the two observed nodal planes, into agreement with the direction and the sense of slip predicted by the stress model [Gephart and Forsyth, 1984; Gephart, 1990]. The best fitting stress tensor is found by minimizing the average of the individual misfits. A stress tensor is defined by the azimuths and plunges of the three principal stresses and the measure of stress magnitude, R , indicating the magnitude ratio of the intermediate principal stress

relative to the two extreme ones ($R = (\sigma_1 - \sigma_2)/(\sigma_1 - \sigma_3)$, where σ_1 , σ_2 , and σ_3 are the greatest, intermediate and least principal stress, respectively).

3.3.2 Criteria for Successful Inversions

We propose that the average misfit, F , is made up of two components: 1) a contribution from errors in the fault plane solutions, and 2) heterogeneity in the stress field that caused the earthquakes in the data set. Thus, we subdivide the data set until we find the smallest possible average misfit, F_{min} . Assuming that the quality of fault plane solutions does not vary significantly as a function of space, we surmise that every inversion will result in an F that contains approximately F_{min} due to errors in fault plane solutions, and the rest, F_{tect} , will be due to heterogeneity of the tectonic stress field.

$$F = F_{min} + F_{tect} \quad (3.1)$$

If F_{tect} is smaller than a threshold, we may term the data set satisfactorily homogeneous; if it is larger, we will reject the inversion result as one contaminated substantially by heterogeneity. We estimate F_{min} by selecting from our large data set of several hundred earthquakes a subset for which F_{tect} may approach zero or be negligibly small. We will assume that the smallest F we obtain for any subset, using a number of events large enough to obtain a stable solution, will be an approximate indication of F_{min} , provided that this value is less than approximately 6° . This requirement is based on the observation that synthetic data sets with errors of approximately 15° (average of the uncertainties in the strike, dip, and rake) lead to $F \leq 6^\circ$ [Wyss *et al.*, 1992; Gillard *et al.*, 1996]. Therefore, the average misfit is the first criterion to estimate the degree of heterogeneity in a sample.

The limit of the 95% confidence regions of the orientation of the principal stress axes is the second criterion for judging the quality of the inversion results. A stress

tensor is accepted if the 95% confidence regions of the greatest and least principal components of the tensor are well constrained, i.e., do not overlap. The 95% confidence regions are also used to judge the difference of two stress tensors. If the corresponding 95% confidence regions of two stress tensors do not overlap, we term the two stress tensors as significantly different at the 95% level. However, two sets of principal stresses with overlapping confidence areas may still be shown to be different on the basis of some criteria [*Michael, 1987*]. Therefore, our criterion requiring that the 95% confidence regions do not overlap for accepting differences between two stress tensors as real, is conservative.

3.3.3 The Cumulative Misfit Method

The cumulative misfit method [*Wyss and Lu, 1995; Lu and Wyss, 1996*] is used as a tool to find volumes containing homogeneous data sets. In this method we use a test-stress tensor to calculate the misfit for every earthquake in the data set. We plot the cumulative misfit of sequential events as a function of distance along strike (or depth or time if these parameters are of interest) expecting to see changes in slope of this curve (i.e. changes in average misfit) wherever the orientation of the stress tensor changes. For the segment of the data set for which the test-tensor is the best solution the misfits will be small (i.e. the slope of the cumulative curve will be low), but for neighboring segments for which the test-tensor is not correct, the misfits are likely to be larger, leading to a steeper slope of the curve [*Wyss and Lu, 1995; Lu and Wyss, 1996*]. The contrast between slopes in segments with different stress tensors depends in a non-linear way on the choice of the test-tensor. In particular, we may not be certain that we have found all existing boundaries between realms of different stress directions. However, where we find a statistically significant contrast between average misfits we have successfully

defined a boundary, if we can also show that F in separate inversions of the subsets is significantly lower than F of the joint data. The statistical significance of the difference between segments is measured by the standard deviate z -test [Wyss and Lu, 1995; Lu and Wyss, 1996]. We use several test-tensors to define homogeneous subsets and use the average of estimates of the slope changes of the cumulative misfit curves for possible stress segmentation boundary locations.

3.3.4 Test of the Cumulative Misfit Method

To demonstrate the validity of the cumulative misfit method for detecting difference in stress orientations, we applied it to a synthetic data set containing two incompatible subsets. We created two data sets with 25 events in each group. These synthetic events are created by adjusting the fault plane solutions such that the slip vector on one of the nodal planes coincides with predicted slip direction based on a presumed stress tensor. Inversion for stress directions of the first set (earthquake No. 1 to 25 in Figure 3.1) yields $\sigma_1=145^\circ/10^\circ$ (azimuth/plunge), $\sigma_2=245^\circ/44^\circ$, $\sigma_3=45^\circ/44^\circ$, $R=0.5$, and $F=0.8^\circ$ (Figure 3.1b). The distribution of P and T-axes of these events is shown in Figure 1a. Inverting the second set of 25 events (earthquake No. 26 to 50 in Figure 3.1, with P and T-axes shown in Figure 3.1g) for stress direction results in $\sigma_1=215^\circ/60^\circ$, $\sigma_2=18^\circ/29^\circ$, $\sigma_3=112^\circ/7^\circ$, $R=0.5$, and $F=0.7^\circ$ (Figure 3.1h). We then performed stress inversions in a moving window, that is, the earthquakes falling within the window are inverted and the average misfit is determined, then the window is advanced by one earthquake along the abscissa. This method is based on the assumption that average misfits will become bigger if the segmentation boundary falls within the window. Therefore the segmentation boundaries should be near the peaks of curves of average misfit versus window position. Figure 3.1 shows the average misfit as a function

of position of the moving window for several different window lengths, i.e., 10, 13, 15, 17, 20, 22, 25, 28, 30, 33, and 50 earthquakes. We find that inversions of samples confined to one of the two homogeneous data sets always result in $F < 1.0^\circ$. Misfits of $F > 1.0^\circ$ indicate that the earthquakes are not confined to one of the two homogeneous data sets. As long as the moving window includes the segmentation boundary (between earthquake No. 25 and 26), the inversion will yield a significant increase of the misfit. The horizontal line in Figure 3.1 separates inversion results that are meaningless as the data came from two stress regimes from valid results (below the line). We interpret $F \sim 1.0^\circ$ as F_{min} in this case, and use it as a guide for judging inversion results in this test.

Figure 3.1 also demonstrates the second criterion used for judging inversion results, that is, the 95% confidence regions of the greatest and least principal stress directions are well constrained. Inverting 10 earthquakes from each data set (i.e., earthquake No. 1 to 10, and No. 41 to 50) yields the same stress directions as those from 25 events, however, the 95% confidence regions for σ_1 and σ_3 are larger (Figures 3.1d and 3.1j). Because the misfits of the inversions for $N = 10$ events are around 1.0° , and the 95% confidence regions for σ_1 and σ_3 are well constrained, we interpret the inversion results as acceptable and meaningful. Inversion for stress directions for five events from each data set separately (i.e., earthquake No. 1 to 5, and No. 46 to 50) results in $F \sim 1.0^\circ$ also. The distributions of P and T-axes for this case are shown in Figures 3.1e and 3.1k, respectively. However, 95% confidence regions for σ_1 and σ_3 are so poorly constrained that we do not accept them as meaningful (Figures 3.1f and 3.1l). The inversion results of the five events would be mis-interpreted as acceptable if we neglected the second criterion for judging the inversion.

In order to help show how the cumulative misfit method [Wyss and Lu, 1995; Lu and Wyss, 1996] could be used to pick up the stress segmentation boundary

between earthquake No. 25 and 26, we used seven stress tensors as reference models, and calculate the misfit of individual events respective to each reference stress tensor, and then plot the cumulative misfit as a function of earthquake number (Figure 3.2). The seven reference stress models are shown at the upper left corner of Figure 3.2. Based on this method, the changes of slopes in the cumulative misfit curves resulting from the application of several stress tensors are interpreted as the segmentation boundaries [Wyss and Lu, 1995; Lu and Wyss, 1996]. Six out of seven cumulative misfit plots clearly show the stress segmentation boundary between earthquake No. 25 and 26. The stress boundary does not show up if the test tensor is close to that best fitting the over all data set of $N = 50$ (d plot in Figure 3.2). Thus we conclude that the method proposed by Wyss and Lu [1995] and Lu and Wyss [1996] is capable to identify at least in some cases the stress segmentation boundaries, if we use several reference stress tensors, and use the average estimates for stress segmentation locations. The ratio of computation time for performing stress inversions as in the moving window analysis (Figure 3.1) and cumulative misfit analysis (Figure 3.2) is 100:1, approximately. This shows that the cumulative misfit method is not only effective, but also time-saving.

The size of F may depend inversely on N , the number of events in the inversion. If F is a strong function of N we have to account for this effect in our criteria for accepting inversion results. To help show how the average misfit changes as function of number of earthquakes used in the inversion, we combine the two synthetic data sets (Figure 3.1) into a single set. We randomly select a number of earthquakes from this single data set, and invert for stress directions, obtaining an average misfit. Figure 3.3 shows the average misfit and its standard deviation as a function of N selected randomly from a total of 50 events. The average misfit is reduced about 1.5° from 10.2° to 8.7° if we reduce the earthquake number from 50 to 25, and about 2.3° (from 8.7° to 6.4°) if we reduce the earthquake number from

25 to 12 (Figure 3.3). Thus the average misfit can be reduced about 15% to 25% in this heterogeneous data set if the number of earthquake is cut in half. Therefore, reducing the earthquake number does not significantly reduce the misfit, if the earthquakes in the inversion are randomly selected from more than a single stress regime.

The way to significantly reduce the misfit is by identifying correctly the segmentation boundaries, and then inverting separately the events within the volumes identified by the boundaries. For comparison, we plot F of the inversion results, which are shown in Figure 3.1 and do not contain the segmentation boundary, in the lower part of Figure 3.3. In these cases F is not a function of N , and the average misfit is reduced by almost an order of magnitude compared to the worst case of inversion result for $N = 50$, the heterogeneous full data set. This demonstrates that by inverting earthquakes from a single stress regime, we could significantly reduce the misfit by a factor of 5 to 8, approximately, compared to F of the events selected randomly from the heterogeneous data set.

Next, we created another set of 50 earthquakes with homogeneous stress direction. The P and T-axes are shown in Figure 3.4a. The inversion using all 50 events yields $F \sim 1.5^\circ$. We then randomly selected a number of events from this single data set, and inverted them for stress directions to obtain the average misfit. The lower part of Figure 3.4 shows F as a function of N . The average misfit stays approximately the same regardless of the number of events used in the inversion. Figure 3.4b shows the best fitting stress tensors from all the random inversions. The solutions of best fitting stress tensors are very stable. This test demonstrates that average misfits of subsets are not reduced significantly if the original data set consists of earthquakes which are homogeneous in stress direction. We conclude that in these cases, significantly reducing the average misfit could be achieved only if the existing stress segmentation boundaries were correctly identified.

3.3.5 Discussion

The cumulative misfit method for identifying changes in stress orientation gives no guarantee that all boundaries are found [d plot in Figure 3.2]. But all boundaries found appear to be real. Based on the tests on the heterogeneous synthetic data set we propose that most test tensors find the location of change in stress direction. Thus, we proceed as follows when searching for homogenous subsets in a large but possibly heterogeneous set of fault plane solutions. We first calculate cumulative misfit curves based on one or several arbitrary test tensors. Then we select a subset of events that have approximately uniform misfits (constant slope) for inversion. If the resulting $F \leq 6^\circ$, and confinement of the stress directions is adequate, then we have found a first meaningful solution that applies to a subset of the data. Then we use this first meaningful solution as a test tensor for the entire data set. The resulting cumulative misfit curve defines the extent of the data for which this test tensor is valid as the segment of the curve with the lowest slope. From this cumulative misfit curve, and from any of the ones calculated before we then select other subsets of the data for separate inversion, repeating the procedure to find homogeneous subsets as described above.

The significance of the difference between average misfits as judged by the z-test [Wyss and Lu, 1995; Lu and Wyss, 1996] is not equivalent to the test of *Cephart and Forsyth* [1984] for the difference between orientations of stress tensors. The average misfit may be found to be significantly different between two samples for which the stress tensors cannot be distinguished at a statistically significant level. In these cases we know that there is a difference in stress directions between the two samples, but we do not know how much this difference is, or we cannot define the stress directions adequately in the two subsets.

Estimates of stress directions by inversion of fault plane solutions are mean-

ingless if they are poorly constrained or derived from heterogeneous data sets. We use the 95% confidence limits calculated using the method by *Gephart and Forsyth* [1984] as the criterion for judging the degree of constraint. For the homogeneity criterion we proposed the generic value of $F \leq 6^\circ$ for the average misfit [*Wyss et al.*, 1992; *Gillard et al.*, 1996]. We do not propose $F = 6^\circ$ as a magic number that always separates homogeneous from heterogeneous sets. Rather we view it as an approximate limit, since the size of the two terms that make up F in equation (1) is unknown. Because average misfits up to 6° can in general be attributed to reasonably small errors in fault plane solutions (15°), solutions with $F \leq 6^\circ$ cannot be rejected. Therefore, we accepted solutions with $F \leq 6^\circ$ as satisfying the assumption of homogeneity and as meaningful, as long as the 95% confidence regions for the greatest and least principal stresses do not overlap. Solutions with misfits in the range $6^\circ < F < 7.5^\circ$ were accepted if the principal stresses are resolvable at the 95% confidence level, although they probably contain a moderate amount of heterogeneity. Inversions for stress directions resulting in $F > 7.5^\circ$ were rejected because they violate the assumption of homogeneity to a degree that is unacceptable. *Beroza and Zoback* [1993], and *Zoback and Beroza* [1993] in their studies of the stress orientation associated with Loma Prieta earthquake and its aftershocks, accepted misfit of more than 10° . Our view is that value of this magnitude definitely reflect heterogeneity of stress directions in the data, considering that the fault plane solutions in the study area should be of high quality.

3.4 Stress Directions Along the Alaska WBZ

3.4.1 Data

The first part of the data set consists of 470 earthquakes with $M_L = 3.0 \pm 0.5$ recorded by the Alaska Earthquake Information Center (AEIC) (Figure 3.5), and is composed of two distinct classes of earthquakes: 1) crustal earthquakes in the overriding plate (North America Plate); and 2) WBZ earthquakes within the subducting part of the oceanic plate (Pacific Plate) landward of the trench. Among the 470 earthquakes, 67 are crustal events in the overriding plate. These crustal events ($D < 40$ km) are distributed in two patches of the study area: the first is near $63.5^\circ\text{N}/151^\circ\text{W}$, the second is spread widely between $63^\circ\text{N} - 65^\circ\text{N}$ and $146.5^\circ\text{W} - 149.5^\circ\text{W}$ (Figure 3.6). The 19 events in the area between Anchorage and Valdez with $D < 40$ km (Figure 3.5) are located in the oceanic plate based on the detailed seismicity study of *Page et al.* [1989]. The WBZ earthquakes with $40 < D < 90$ km are distributed approximately evenly in the study area. For deep WBZ events ($D > 90$ km), the spatial distribution is not even. In the bending parts of the WBZ the density of events is higher than in the straight part of the WBZ (Figure 3.5).

The fault plane solutions for earthquakes occurring between September 1987 and March 1994, are based on P-wave polarities re-read by the authors. We used the program HYPOELLIPSE [*Lahr*, 1989] to locate the earthquakes, and program FPFIT [*Reasenber and Oppenheimer*, 1985; *Lahr*, personal communication] to compute the fault plane solutions. From approximately 650 selected earthquakes, 180 were rejected because of poorly constrained fault plane solutions, resulting in a final data set of 470. The average number of first motions per event is 27. For shallow and intermediate depth events it is essential to use a velocity model

with continuously increasing velocity (1-D) with depth to obtain good quality fault plane solutions. For most earthquakes with $M_L \geq 3$ useful fault plane solutions were obtained. In the range $2.5 < M_L < 3.0$ the success rate varied, with better results for the deeper events. The formal errors of hypocenters of the events are 0.9 ± 0.6 km horizontally, and 2.8 ± 1.3 km vertically. The formal errors of strike, dip, and rake of the focal mechanism solutions are $7^\circ \pm 6^\circ$, $7^\circ \pm 6^\circ$, and $10^\circ \pm 8^\circ$, respectively.

The second part of our data set is composed of 38 focal mechanisms from the Harvard Centroid Moment Tensor (CMT) catalog, and 29 fault plane solutions from *Bhattacharya and Biswas* [1979] and *Estabrook et al.* [1988]. The average magnitude for these 67 earthquakes is 4.8 ± 0.7 . These large events are located in the WBZ. Out of 67 events, 15 are located in the shallow part of the WBZ ($D < 40$ km), and 52 in the intermediate and deep parts of the WBZ ($55 < D < 140$ km) (Figure 3.7). These events occurred during the period of 1972 to 1995.

3.4.2 Analysis

3.4.2.1 Large Earthquakes in the WBZ

Inverting the entire set of large events (set L in Table 1) we find a misfit of $F = 8.5^\circ$ too large to be accepted based on our criteria. Because the cumulative misfit method is only applicable to one dimensional analysis, we did not investigate the stress heterogeneity using the cumulative misfit method for this data subset. By trial and error analysis, we divided the large events into 3 subsets (La, Lb, and Lc, Figure 3.7). We obtained average misfits of 3.3° , 4.0° , and 5.0° for volume La, Lb, and Lc, respectively. These misfits are small enough to match our criterion for acceptably homogenous data sets. Thus, there is no need to further subdivide the data set for large earthquakes. The constraints (i.e. 95% confidence regions)

of these results do not overlap, so they can be accepted as meaningful (Figure 3.7, sets La, Lb and Lc in Table 1).

An invalid stress tensor may be obtained if the data are composed of sets from more than one volume with significantly different stress orientations and this solution may not readily be identified as incorrect. Inverting the 48 large earthquakes (set Ld, Table 1) by combining set La and Lb yields the same stress tensor as the one obtained by inverting set Lb with an average misfit of 6.9° . After subdividing the 48 earthquakes into two subsets, we find the stress tensor in set La is significantly different from that in the set Lb, and the average misfits in set La and Lb are reduced to 3.0° and 4.0° , respectively. As the inversion program itself favors the majority of the focal mechanisms, we may not easily realize that we violate the basic assumption of stress homogeneity in the volume if we neglect the criterion of requiring a small F.

3.4.2.2 Small Earthquakes in the Crust

The small crustal earthquakes ($D < 40$ km) separate into two clusters located near Mt. McKinley (cluster 1) and in the area near the apex of the Denali Fault and Fairbanks, cluster 2 (Figure 3.6). As a first sub-division we selected these two sets on the basis of geographic distribution. The average misfits for clusters 1 and 2 (Figure 3.6) are smaller than 10.2° , the average misfit obtained by using all small shallow earthquakes (set S0, Table 1), but they are too large to be accepted as homogeneous: 7.5° and 8.7° (sets 1 and 2, Table 1), respectively. By trial and error we subdivided set 2 into a northern and southern part, finding no dividing line that leads to a satisfactorily small misfit for the southern part ($F = 8.9^\circ$, set 2S, Table 1). Thus, we cannot reliably define the stress directions at the northern apex of the Denali fault (dots in Figure 3.6). In the area near Fairbanks the stress directions are well constrained (diamonds in Figure 3.6) and the misfit is small (F

= 3.8° , set 2N, Table 1).

When the shallow earthquake cluster 1, near Mount McKinley, was subdivided by trial and error, we found two sets with acceptably small average misfits (sets 1W and 1E, Table 1). However, the result for the eastern part (1E, Table 1) is so poorly constrained (Figure 3.13) that we do not accept the solution as meaningful.

3.4.2.3 Small Earthquakes in the WBZ

We separately inverted the fault plane solutions of the 19 earthquakes ($D \leq 40$ km) located near Valdez (Figure 3.5) because these events are widely separated from the other WBZ earthquakes. The inversion of the data yields $F = 3.3^\circ$ (Set 3, Table 1), which equals approximately the smallest values we have found in other data sets [*Liang and Wyss*, 1991; *Gillard et al.*, 1992; *Gillard and Wyss*, 1996; *Gillard et al.*, 1996; *Lu and Wyss*, 1996]. This suggests that the quality of the Alaskan fault plane solutions is comparable to those in Hawaii, California, Iran and the Aleutians.

We subdivided the bulk of our data, the remaining 403 small subcrustal earthquakes ($40 < D < 140$ km), using the cumulative misfit method [*Wyss and Lu*, 1995; *Lu and Wyss*, 1996]. Because this method is currently applicable for one-dimensional analysis only, we had to decide whether to search for segmentation as a function of depth or distance along strike of the seismic zone first. Based on preliminary exploration we decided to first define subdivisions in three profiles as a function of depth (Figure 3.5), because the contrasts in this direction are expected to be strongest. The cumulative misfit curves as a function of depth for the three polygons (Figure 3.5) are shown in Figure 3.8. The changes of the slopes in the cumulative plot are interpreted as boundaries in the stress directions. The boundaries suggested by several cumulative curves in Figures 3.8a, 3.8b, and 3.8c are at 50, 60, 75, 90, and 120 km depths. We use the average estimates of changes

of stress directions from several stress tensors as the segmentation boundaries. Because of the limitation of the number of earthquakes in our analyses, some of the boundaries suggested by the cumulative misfit curves are not selected (e.g., around earthquake No. 20 and 30 in Figure 3.8b). All but the 120 km depth boundary are confirmed by results in more than one profile.

The final step in the search for stress boundaries was to plot the cumulative misfit curves as a function of strike from south to north in each of the depth bands 40 - 50, 50 - 60, 60 - 75, 75 - 90, 90 - 120, and 120 - 140 km. As an example with clear segmentation we show the misfit curve for the depth band 120 - 140 km (Figure 3.9). In this example the cumulative misfit angle as a function of distance along strike of the WBZ based on seven test stress tensors, suggests that two stress boundaries exist, dividing the data set into three segments with reasonably uniform misfits. Also the three separate samples happen to contain approximately the same number of events, $N = 19 \pm 1$, which is large enough, in general, to yield stable inversion solutions. The separate inversion of the three subsets at depths 120 - 140 km leads to misfits of 3.8° , 5.0° , and 5.5° (sets 9a, 9b, 9c in Table 1), whereas the inversion using all the earthquakes in this depth range produced $F = 10.4^\circ$. This substantial reduction (a factor of 2 to 3), from an unacceptably large average misfit to small values, confirms that our method of selecting homogeneous data sets by cumulative misfit curves is effective. Based on the geographical distribution of epicenters in this case, we would not have chosen the boundaries found by our technique (Figure 3.10).

The reduction of the average misfit in this example is typical for all depth intervals. The overall data sets for each depth range tended to result in approximately $F = 10^\circ$, whereas the subsets selected by our method had $3.2^\circ < F < 5.5^\circ$ (except for two cases with $F = 6.1^\circ$ and $F = 7.3^\circ$ respectively, Table 1). In some cases, several events located near the segmentation boundaries are excluded from

the final inversions of both neighboring segments because these events do not fit either of the stress tensors of the neighboring segments. For some of the subsets the constraint of the principal stress axes were unsatisfactory (e.g., the data near 61°N in the depth range 50 - 60 km, Figure 3.12; the northern set in the depth range 40 - 50 km, Figure 3.11). The results for these subsets are shown in Figure 3.13.

3.4.3 Results and Discussion

3.4.3.1 Stress Directions in the Alaskan WBZ

For the large earthquakes (67 events) only two divisions into three subsets were necessary to reduce the misfit from an unacceptably large value of 8.5°, 4.0° and 5.0° in the three subsets. These misfit values indicate that stress directions are homogeneous in these volumes. The data set of small earthquakes had to be subdivided into 25 subsets for satisfying the condition of homogeneity. For 20 of these data sets the inversions yielded meaningful results with reasonably well constrained stress directions. The estimated stress directions show some similarities, but they also differ significantly. They reveal a picture of complex stress directions in the subducting slab under Alaska, especially in and near its pronounced bend.

The number of large shallow WBZ earthquakes with fault plane solutions in Alaska is 15. The orientations of the principal stresses (set La in Table 1, Figures 3.7 and 3.14) seem acceptable because the least principal stress is well constrained. Epicenters of most of these events are scattered in the region between Anchorage and Valdez (Figure 3.7). For approximately the same area we have a data set of 19 small earthquakes that also define a normal to strike-slip faulting regime (set 3, Table 1 and Figures 3.11 and 3.14). σ_3 axes defined from both large and small earthquakes are oriented horizontally, striking $N56^\circ \pm 3^\circ W$. Although the data

are somewhat scant, the evidence is clear that in the area between Anchorage and Valdez a stress regime exists with least principal stress striking WNW horizontally. The plunge of the least principal stress, $2^\circ \sim 5^\circ$, is consistent with the gentle dip direction of the WBZ, $6^\circ \sim 7^\circ$, reported by *Page et al.* [1989, 1991].

The stress directions in the WBZ below 40 km present a simple picture if defined by large earthquakes only, but a complex one with different directions in most volumes of dimensions with about 10 to 30 km in depth, by 50 to 100 km along strike (Figure 3.14). The unusual feature of the solution derived from the large earthquake data set is that orientation of the greatest principal stress is parallel to the strike of the WBZ. This is unusual because the typical fault plane solution in deep seismic zones has the intermediate stress direction aligned along strike. The stress orientation derived from the large earthquakes is confirmed by the general trend observed in the stress orientations derived from the small earthquake data set. Approximately 70% of the 18 separate inversion results show the least principal stress axis pointing approximately down-dip of the WBZ, and 60% have a greatest principal stress oriented approximately horizontal and in the direction of the strike of the WBZ (Figure 3.14, Table 1). From this we conclude that the basic force of a sinking slab, causing the orientation of σ_3 in the classical down-dip direction, is modified by the presence of the major bend in the WBZ. Along an axis roughly from Palmer to Mt. McKinley the Alaskan WBZ changes strike by about 35° (Figure 3.14). That portion of the bend with the greatest curvature is also associated with a cluster of seismic activity, particularly in the depth range from 90 to 140 km. In spite of the large number of events available and several subdivisions, it was not possible to resolve the stress in most volumes associated with the bend. We believe that this is due to the very rapid spatial stress changes in the bend, rendering the sub-volumes heterogeneous. The existence of this cluster is possibly a further indication of rapidly changing stresses in the vicinity of the bend.

Along-strike compression in the WBZ below Cook Inlet has also been observed by *Lahr* [1975], *Engle* [1982], *Pulpan and Frohlich* [1985], and *Lahr et al.* [1993, 1994]. *Creager and Chiao* [1992] obtained along-strike compression from 3-D convective flow modeling of a Pacific slab subducting underneath Alaska. The along-strike compression is explained by the "table cloth effect" [*Creager and Chiao*, 1992]. In their model, *Creager and Chiao* [1992] showed that the geometry of the Pacific slab is similar to that of a table cloth draped over the corner of a table. Since the table cloth (Pacific plate) is smooth when lying on the table, a fold of extra material develops when it is pushed past the edge over a table corner. The presence of this extra material in the corner has to be accommodated and translates into horizontal compressive stress within the deep slab away from the bend [*Creager and Chiao*, 1992].

Out of the 23 volumes within which we had enough earthquakes to locally define the stress directions, five showed unusable results (areas shaded in Figure 3.14). Either the average misfits or the confidence areas were too large for acceptance as meaningful results. Most of the remaining 18 solutions were statistically different from each other at the 95% significance level. In the stereographic projections the areas of the confidence levels of one or two principal axes do not overlap. Some of these differences are very pronounced, resulting in a generally heterogeneous picture of stress directions (Figure 3.14). Nevertheless, there are some parts of the WBZ in which neighboring solutions are similar. For example near the deeper northern end of the WBZ volumes 7d, 8d, and 9c show enough similarity that one may consider them approximately the same (Figures 3.10, 3.11, 3.12, and 3.14).

In the Aleutian WBZ, complexity of stress directions similar to those we found probably exist as well. *Reyners and Coles* [1982] subdivided their data set of first motions into five subsets in order to obtain reasonably consistent patterns for composite fault plane solutions for small earthquakes in the WBZ of depths

between 50 and 250 km beneath the Shumagin Islands.

We conclude that the basic stress field of down-dip extension is strongly modified throughout the WBZ under Alaska. The modification is most pronounced in the bend of the strike. Within the bend, volumes with dimension of 10 to 20 km do not satisfy the condition of homogeneity necessary for inversion of the stress directions. The presence of the bend makes itself known by the generation of horizontally compressive stresses along strike of the entire WBZ under Alaska. In addition, local perturbations of the stress field exist within the WBZ in volumes with dimensions of a few tens of kilometers.

3.4.3.2 Stress Directions in the Crust

In the area within about 100 km radius around Fairbanks a set of 16 earthquakes (set 2N in Table 1, and Figure 3.14) defines a stress orientation of strike-slip type, with the greatest principal stress striking approximately NS. The small misfit, $F = 3.8^\circ$, indicates homogeneity, whereas the adjacent 19 earthquakes to the south (set 2S in Table 1 and Figures 3.6 and 3.13) do not fit this solution, nor could a useful solution be obtained using only the southern subset.

The stress directions in the earthquake cluster within a 20 km radius near Mount McKinley are heterogeneous as a whole, but can be defined as of thrusting type in the western part, with the greatest principal stress oriented about NW, perpendicular to the local strike of the Denali fault (set 1W in Table 1 and Figures 3.6 and 3.14). Inversions of the data from the eastern part of this cluster (1E in Table 1) did not lead to meaningful results as the stress directions were too poorly constrained (Figure 3.13). We interpret the stress directions in the areas under Mount McKinley and in 2S as changing rapidly as a function of space, but we do not have enough earthquakes to define them.

The orientation of the near-horizontal greatest principal stress is perpendicu-

lar to the Alaska range, ranging in directions from NNE near Fairbanks to NW near McKinley. This is what one might expect from the topography of the young mountain belt of the Alaska range. The stress tensor solution near Fairbanks obtained from small earthquakes (set 2N, Figure 3.6) is consistent with the few poorly known fault plane solutions of historic large earthquakes in that area [e.g., *Gedney et al.*, 1980; *Estabrook et al.*, 1988; *Page et al.*, 1995; *Fletcher and Christensen*, 1996]. The collision of the Pacific and American plates is most likely responsible for these stresses.

Stress indicators derived from volcanic dikes reported by *Nakamura et al.* [1977] are located in areas where we have no data. Their estimate of greatest principal stress orientation of NNW at Mount Spurr (Figure 3.6), west of Anchorage agrees with that by *Jolly et al.* [1994] based on inversion from focal mechanisms of very small earthquakes near that volcano. In the rest of Alaska only very approximate estimates of stress directions based on surface faulting are available [*Brogan et al.*, 1975; *Bird*, 1996]. These require assumptions in some cases that render the estimates quite uncertain. Nevertheless, they agree with our results in those areas where we have information (Mount McKinley, Fairbanks). It is unfortunate that we have very few fault plane solutions for crustal earthquakes in Alaska. We urgently need more for defining the stress field between Anchorage and Fairbanks as well as along the Denali fault. More high quality fault plane solutions could be obtained if a regional broad band network of seismographs were operated in Alaska.

3.5 Scale of the Stress Field and the Size of Earthquake Ruptures

Large earthquakes can give information about the large scale stress field only, because their rupture dimensions are too large to sense small scale variations in stress directions. Small ruptures, on the other hand could occur in response to the same large scale stress field, but they could alternatively occur in response to a locally perturbed stress field. Therefore one should not assume a-priori that earthquakes of greatly varying size constitute a homogeneous sample [e.g., Caccamo et al., 1996]. This assumption should be tested by inverting the small and large earthquakes in a common area separately. We found that, for the area between Anchorage and Valdez, inversion of large and small earthquakes from the same volume yielded approximately the same stress tensor. In this case we argue that both results are valid, they confirm each other and the large as well as the small earthquakes respond to the regional (dimension of 100 km) stress field.

In the WBZ below 40 km we found well constrained stress directions for the large earthquakes with a satisfactorily small misfit. Since these shocks were distributed in most of the WBZ we accept that result as valid for the WBZ under Alaska as a whole. In contrast, the 384 small earthquakes in the WBZ had to be subdivided into 21 subsets to satisfy our criteria for satisfying the assumption of homogeneity. Most of the 18 well-constrained results showed significant differences from each other, and from the overall solution based on the large events. We conclude that the large scale stress directions in the WBZ measured by the large events are seemingly uniform, but that a great deal of stress perturbations exist in the descending slab at smaller scales, which can only be resolved by inversion of fault plane solutions from small earthquakes.

The rupture dimensions of the small earthquakes we used ($M_L \sim 3$) are a few hundred meters, approximately. The dimensions of the volumes within which we found homogeneity vary from about 10 to 100 km. The ruptures of the large earthquakes we used are approximately 10 km long ($M_s \sim 5$), whereas the stress field sensed by these events seems to be homogeneous over 300 km dimensions. For small earthquakes in Hawaii ($M_L \sim 3$) homogeneity in cubes of the crust with dimensions of about 10 km was found [Gillard *et al.*, 1992, 1996]; whereas in Iran homogeneity in volumes ranging up to 1000 km length was found when studying ruptures longer than 20 km ($M_s > 6$) [Gillard and Wyss, 1996]. The ratio of the dimensions of the homogeneous stress field to the ruptures in all of these cases is similar and approximately 20 to 50. We therefore propose that in inversion of fault plane solutions for stress directions, as performed here, one estimates the stress field in general in an area with dimensions about 20 to 50 times larger than the rupture dimensions of the earthquakes. Also, small earthquakes have the alternate option to sense the overall stress field that has dimensions more than 100 times larger than their ruptures.

3.6 Conclusions

The cumulative misfit method proposed by Wyss and Lu [1995] and Lu and Wyss [1996] is capable of defining segments with homogeneous stress directions along major fault systems or plate boundaries. Both, the results from test on synthetic data sets and application to data from the Alaska WBZ, indicate that the method permits defining regions with homogeneous stress directions. This does not mean the method will always succeed. In its present form, the cumulative misfit method is best suited for application to "belts" of seismicity where the earthquakes are narrowly distributed along a major tectonic feature such as a fault or plate boundary.

To adapt the method for a situation where the seismicity is distributed diffusely over a wide area is a logical next step. Also, in our own application in this paper we found an area where very rapid stress changes made it impossible to obtain sub-volumes with sufficient numbers of fault plane solutions to resolve the stress tensor orientation, and where the cumulative misfit method did not provide information about additional segmentation.

The criteria for accepting a stress tensor, obtained from inverting earthquake focal mechanisms, are (1) the average misfit of the inversion is less than 6° , and (2) the 95% confidence regions of the greatest and least principal stress directions are well constrained. Applying the cumulative misfit method to the Alaska WBZ, we found that the average misfit of at least one of the two new data sets was reduced after dividing a data set. The most typical result of subdividing, using this method, was that F of both subsets were reduced by about a factor of two. Therefore, we conclude that this is a useful method for finding discontinuities in stress directions.

The smallest misfit that can be found in a subset should be calculated in any study of inversion for stress directions, as a gauge of the quality of the fault plane solutions. In Alaska the smallest misfits were about 3.2° , suggesting that the fault plane solutions do not contain substantial errors.

Stress direction along the Alaska WBZ are based on 470 small WBZ earthquakes ($M_L \sim 3$), ranging in depth from the surface to 140 km, and 67 larger earthquakes ($M_s \sim 5$) with known fault plane solutions. For the large earthquakes only two divisions into three sub-sets were necessary to reduce the misfit from an unacceptably large misfit to misfits which indicate that stress directions are homogeneous in the subsets. The data set of small earthquakes had to be subdivided into 25 subsets for satisfying the condition of homogeneity. For 20 of these data sets the inversions yielded meaningful results with reasonably well constrained stress

directions. The stress directions measured by the large earthquakes ($M_s \sim 5$) were homogeneous, with extension down dip and the direction of greatest compression along strike. This unusual orientation of the greatest principal stress is attributed to the bend of the slab under central Alaska, which generates compressive stresses along strike. The stress orientations revealed by small earthquakes, in contrast, exhibited a great deal of heterogeneity as a function of space, although they show a trend that confirms the overall stress directions obtained from the large events. We propose that the ratio of the dimensions of the stress field sensed by earthquakes to the rupture dimensions is about 20 to 50.

The estimated stress directions of the crustal earthquakes corresponded to the following mechanisms: (1) strike-slip faulting with the greatest principal stress oriented NS near Fairbanks, and (2) thrusting with the greatest principal stress oriented NW-SE near Mount McKinley.

3.7 References

- Angelier, J., Determination of the mean principal directions of stresses for a given fault population. *Tectonophysics*, *56*, T17-T26, 1979.
- Beroza, G. C., and M. D. Zoback, Mechanism diversity of the Loma Prieta aftershocks and the mechanics of mainshock-aftershock interaction. *Science*, *259*, 210-213, 1993.
- Bhattacharya, B., and N. N. Biswas, Implications of north Pacific plate tectonics in central Alaska: focal mechanisms of earthquakes. *Tectonophysics*, *53*, 99-130, 1979.
- Bird, P., Computer simulation of Alaskan neotectonics, *Tectonics*, *in press*, 1996.
- Brogan, G. E., L. S. Cluff, M. K. Korringa, and D. B. Slemmons, Active faults of Alaska. *Tectonophysics*, *29*, 73-85, 1975.
- Caccamo, D., G. Neri, A. Sarar, and M. Wyss, Estimates of stress directions by inversion of earthquake fault plane solutions in Sicily, *Geophys. J. Int.*, *113*, 1996.
- Comte, D., and G. Suarez, An inverted double seismic zone in Chile: evidence of phase transformation in the subducted slab. *Science*, *263*, 212-215, 1994.
- Creager, C., L. Y. Chiao, J. P. Winchester, and E. R. Engdahl, Membrane strain rates in the subducting plate beneath South America, *Geophys. Res. Letts.*, *22*, 2321-2324, 1995.
- Creager, C., and L. Y. Chiao, Membrane deformation rate and geometry of Aleutian Alaska subduction, in *Wadati conference on Great Subduction Earthquakes*, eds. D. Christensen, M. Wyss, R. E. Habermann, and J. Davies, p. 27, University of Alaska, Fairbanks, 1992.
- Creager, C., and T. M. Boyd, the geometry of Aleutian subduction: three-dimensional kinematic flow model, *J. Geophys. Res.*, *96*, 2293-2307, 1991.

- Engle, K. Y., 1982, Earthquake focal mechanism studies of Cook Inlet area, Alaska. *M.S. thesis*, University of Alaska Fairbanks, 81 pp, 1982.
- Estabrook, C. H., D. Stone, and J. N. Davies, Seismotectonics of Northern Alaska. *J. Geophys. Res.*, *93*, 12026-12040, 1988.
- Fletcher, H., and D. Christensen. A determination of source properties of large intraplate earthquakes in Alaska. *PAGEOPH*, in press, 1996.
- Gedney, L., S. Estes, and N. Biswas. Earthquake migration in the Fairbanks, Alaska, seismic zone. *Bull. Seism. Soc. Amer.*, *70*, 223-241, 1980.
- Gephart, J. W., and D. W. Forsyth, An improved method of determining the regional stress tensor using the earthquake focal mechanism data: Application to the San Fernando earthquake sequence, *J. Geophys. Res.*, *89*, 9305-9320, 1984.
- Gephart, J. W., FMSI: a FORTRAN program for inverting fault/slickenside and earthquake focal mechanism data to obtain the original stress tensor. *Computer and Geosciences*, *16*, 953-989, 1990.
- Gillard, D., and M. Wyss. Comparison of strain and stress tensor orientation: Application to Iran and southern California, *J. Geophys. Res.*, *100*, *accepted*, 1995.
- Gillard, D., M. Wyss, and J. S. Nakata. A seismotectonic model for western Hawaii based on stress- tensor inversion from fault-plane solutions. *J. Geophys. Res.*, *97*, 6629-6641, 1992.
- Gillard, D., M. Wyss, and P. Okubo, Stress and strain tensor orientations in the south flank of Kilauea, Hawaii, estimated from fault plane solutions, *J. Geophys. Res.*, *100*, *in press*, 1995.
- House, L. S., and K. H. Jacob, Earthquakes, plate subduction, and stress reversals in the eastern Aleutian arc. *J. Geophys. Res.*, *88*, 9347-9373, 1983.
- Iguchi, M., K. Ishihara, and Y. Tatsumi, Characteristics of non-down-dip-extensional intermediate- depth earthquakes immediately beneath the volcanic front in South

- Kyushu, Japan, *Geophys. Res. Letts.*, *22*, 1905-1908, 1995.
- Isacks, B., J. Oliver, and L. R. Sykes. Seismology and the new global tectonics. *J. Geophys. Res.*, *73*, 5855-5899, 1968.
- Isacks, B., and P. Molnar. Distribution of stresses in the descending lithosphere from a global survey of focal mechanism solution of mantle earthquakes. *Rev. Geophys. Space Phys.*, *9*, 103, 1971.
- Jolly, A. D., R. A. Page, and J. A. Power, Seismicity and stress in the vicinity of Mount Spurr volcano, south central Alaska, *J. Geophys. Res.*, *99*, 15305-15318, 1994.
- Jones, L. M., Focal mechanisms and the state of stress on the San Andreas fault in southern California. *J. Geophys. Res.*, *93*, 8869-8891, 1988.
- Kissling, E., and J. C. Lahr, Tomographic image of the Pacific slab under southern Alaska. *Eclogae geol. Helv.*, *84*, 297-315, 1991.
- Lahr, J., C. D. Stephens, R. Page, and K. Fogleman, Characteristics of the Aleutian Wadati- Benioff zone seismicity beneath southern Alaska, 301-303, *SUBCON: An Interdisciplinary Conference on the subduction Process*, Catalina Island, California, 1994.
- Lahr, J., K. Fogleman, and R. Page, Stress within the Pacific plate of Southern Alaska. *EOS. Transactions, AGU*, *74*, 95-95, 1993.
- Lahr, J., HYPOELLIPSE/Version 2.0: A computer program for determining local earthquake hypocentral parameters, magnitude, and first motion pattern. *U.S. Geol. Surv., Open-File Rep.*, *89-116*, 1989.
- Lahr, J., Detailed seismic investigation of Pacific-North American Plate interaction in southern Alaska, *Ph. D. Thesis*, New York, Columbia University, 88p, 1975.
- Li, Z., N. Biswas, G. Tytgat, H. Pulpan, and M. Wyss, Stress directions along the Alaska Wadati-Benioff zone from inversion of focal mechanism data, *Tectonophysics*, *246*, 163-170, 1995.

- Liang, B., and M. Wyss, Estimates of orientation of stress and strain tensors based on fault plane solutions in the epicenter area of the great Hawaiian earthquake of 1868. *Bull. Seis. Soc. Am.*, 81, 2320-2334, 1991.
- Lu, Z., and M. Wyss, Segmentation of the Aleutian plate boundary derived from stress direction estimates based on fault plane solutions, *J. Geophys. Res.*, 101, 803-816, 1996.
- Michael, A. J., Determination of stress from slip data: faults and folds. *J. Geophys. Res.*, 89, 11517-11526, 1984.
- Michael, A. J., Use of focal mechanisms to determine stress: a control study. *J. Geophys. Res.*, 92, 357-368, 1987.
- Matsuzawa, T., N. Umino, A. Hasegawa, and A. Takagi, Normal fault type events in the upper plane of the double-planned deep seismic zone beneath the northeastern Japan arc, *J. Phys. Earth*, 34, 85-94, 1986.
- McKenzie, D. P., The relationship between fault plane solutions for earthquakes and the directions of the principal stresses, *Bull. Seism. Soc. Am.*, 59, 591-601, 1969.
- Nakamura, K., K. H. Jacob, and J. N. Davies, Volcanoes as possible indicators of tectonic stress orientation - Aleutians and Alaska. *PAGEOPH*, 115, 87-112, 1977.
- Page, R. A., N. N. Biswas, J. C. Lahr, and H. Pulpan, Seismicity of continental Alaska, in Slemmons, D. B., Engdahl, E. R., Zoback, M. D., and Blackwell, D. D., eds., *Neotectonics of North America, boulder, Colorado. Geol. Soc. Amer., Decade Map Volume 1*, 1991.
- Page, R. A., G. Plafker, and H. Pulpan, Block rotation in east-central Alaska: A framework for evaluation earthquake potential? *Geology*, 1995.
- Pulpan, H., and C. Frohlich, Geometry of the subducted plate near Kodiak Island and the lower Cook Inlet, Alaska, determined from relocated earthquake

- hypocenters, *Bull. Seism. Soc. Amer.*, *75*, 791-810, 1985.
- Rebai, S., H. Philip, and A. Taboada, Modern tectonic stress field in the Mediterranean region: evidence for variation in stress directions at different scales. *Geophys. J. Int.*, *110*, 106-140, 1992.
- Reasenber, P., and D. Oppenheimer. Fortran computer programs for calculating and displaying earthquake fault plane solutions. *U.S. Geol. Surv., Open-File Rep.*, *85-739*, 1985.
- Reyners, M., and K. Coles. Fine structure of the dipping seismic zone and subduction mechanics in the Shumagin Islands, Alaska, *J. Geophys. Res.*, *87*, 356-366, 1982.
- Smith, S. W., J. S. Knapp, and R. C. McPherson, Seismicity of the Gorda plate, structure of the continental margin, and an eastward jump of the Mendocino triple junction, *J. Geophys. Res.*, *98*, 8153-8171, 1993.
- Wiens, D. A., J. J. McGuire, and P. J. Shore. Evidence for transformational faulting from a deep double seismic zone in Tonga, *Nature*, *364*, 790-793, 1993.
- Wyss, M., B. Liang, W. R. Tanigawa, and X. Wu, Comparison of orientations of stress and strain tensors based on fault plane solutions in Kaoiki Hawaii, *J. Geophys. Res.*, *97*, 4769- 4790, 1992.
- Wyss, M., and Z. Lu, Plate boundary segmentation by stress directions: Southern San Andreas fault, California, *Geophys. Res. Letts.*, *22*, 547-550, 1995.
- Yin, Z. M., and G. Ranalli. Determination of tectonic stress field from fault slip data: toward a probabilistic model. *J. Geophys. Res.*, *98*, 12165-12716, 1993.
- Zoback, M. D., and G. C. Beroza, Evidence for near-frictionless faulting in the 1989 (M 6.9) Loma Prieta, California. Earthquake and its aftershocks. *Geology*, *21*, 181-185, 1993.

Table 3.1 Stress tensor results for the Alaska WBZ

Set	N	F (°)	Depth (km)	M	σ_1		σ_2		σ_3		R	I
					PL	AZ	PL	AZ	PL	AZ		
S0	67	10.2	< 40	~ 3								N
S1	403	12.7	40 - 140	~ 3								N
L	67	8.5	0 - 140	~ 5	1	222	75	128	15	312	0.2	N
La	15	3.3	0 - 40	~ 5	2	207	87	78	2	297	0.6	3
Lb	33	4.0	55 - 140	~ 5	2	191	55	98	35	282	0.6	3
Lc	19	5.0	55 - 140	~ 5	2	78	30	169	60	343	0.7	3
Ld	48	6.9	0 - 140	~ 5	2	191	55	98	35	282	0.7	N
1	32	7.5	< 40	~ 3	12	147	9	55	75	290	0.3	N
1W	18	3.8	< 40	~ 3	7	147	9	56	79	273	0.5	2
1E	14	5.8	< 40	~ 3	22	151	68	328	1	61	0.4	N
2	35	8.7	< 40	~ 3	16	350	43	96	42	245	0.6	N
2N	16	3.8	< 40	~ 3	28	9	43	128	35	258	0.5	2
2S	19	8.9	< 40	~ 3	26	144	1	54	64	321	0.3	N
3	19	3.3	< 40	~ 3	72	218	17	21	5	112	0.4	7
4	39	8.1	40 - 50	~ 3	43	187	44	33	13	290	0.4	N
4a	23	4.3	40 - 50	~ 3	43	184	43	32	14	288	0.4	7
4b	16	6.1	40 - 50	~ 3	45	248	42	41	14	144	0.5	N
5	48	10.0	50 - 60	~ 3	12	21	72	150	14	288	0.6	N
5a	17	3.2	50 - 60	~ 3	2	152	88	284	2	62	0.6	8
5b	10	5.4	50 - 60	~ 3	80	93	0	2	10	272	0.8	N
5c	19	4.8	50 - 60	~ 3	72	42	17	211	3	302	0.5	8
6	67	10.2	60 - 75	~ 3	52	115	6	18	38	283	0.5	N
6a	12	4.0	60 - 75	~ 3	11	150	79	324	1	60	0.6	6
6b	12	3.6	60 - 75	~ 3	12	7	73	140	12	274	0.6	6
6c	18	3.7	60 - 75	~ 3	30	67	17	167	55	282	0.7	6

Table 3.1 Stress tensor results for the Alaska WBZ

Set	N	F (°)	Depth (km)	M	σ_1		σ_2		σ_3		R	I
					PL	AZ	PL	AZ	PL	AZ		
6d	18	4.9	60 - 75	~ 3	62	162	8	268	27	3	0.3	6
7	48	10.2	75 - 90	~ 3	3	187	60	92	30	279	0.4	N
7a	7	1.6	75 - 90	~ 3	48	196	40	355	11	94	0.6	7
7b	15	5.1	75 - 90	~ 3	55	51	10	155	34	252	0.5	7
7c	13	7.3	75 - 90	~ 3	31	229	42	105	32	341	0.4	N
7d	12	1.9	75 - 90	~ 3	3	187	60	91	30	279	0.3	7
8	83	11.1	90 - 120	~ 3	15	24	55	136	31	284	0.5	N
8a	15	3.4	90 - 120	~ 3	18	213	22	116	61	339	0.6	8
8b	16	3.2	90 - 120	~ 3	21	4	4	272	69	171	0.6	8
8c	16	4.7	90 - 120	~ 3	27	53	45	174	33	304	0.6	8
8d	14	5.0	90 - 120	~ 3	6	216	50	119	39	312	0.5	8
9	71	10.4	120 - 140	~ 3	2	36	46	128	44	305	0.5	N
9a	21	3.8	120 - 140	~ 3	4	205	49	110	41	298	0.5	6
9b	21	4.0	120 - 140	~ 3	39	167	19	60	44	310	0.8	6
9c	19	5.5	120 - 140	~ 3	13	33	46	137	41	292	0.6	6

I, indicating figure where region of data set is defined and the 95% confidence map is shown; N, number of events; F, average misfit angle (in degrees); M, magnitude; σ_1 , greatest principal stress; σ_2 , intermediate principal stress; σ_3 , least principal stress; AZ, azimuth; PL, plunge; R, magnitude ratio of principal stresses (see text).

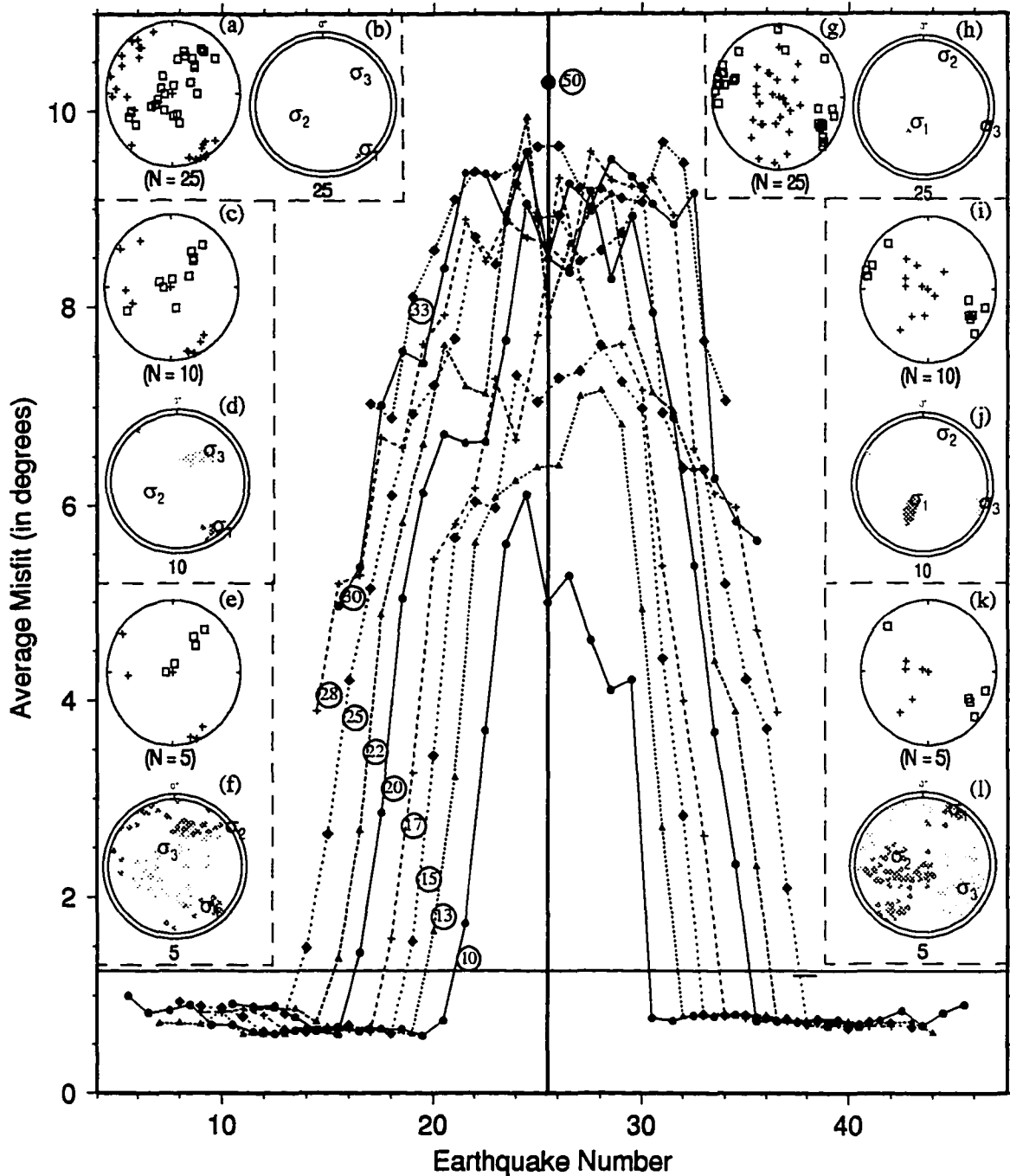


Figure 3.1 Average misfit for inversions for stress directions as a function of position of the moving windows for several window lengths, 10, 13, 15, 17, 20, 22, 25, 28, 30, 33, and 50. The data come from two synthetic sets with different stress regimes. The vertical line between earthquake No. 25 and 26 marks the boundary of change in stress directions. (b), (d) and (f) are stereographic projections of stress directions estimates based on inversions of fault plane solutions from the first set (earthquake No. 1 to 25), and (h), (j) and (l) from the second set (earthquake No. 26 to 50), respectively. The 95% confidence regions for the greatest and least principal stresses are shown by heavy and light shading, respectively. The orientation of P (pluses) and T (squares) axes of the focal mechanisms used in the inversions are shown in (a), (c), (e), (g), (i), and (k), respectively.

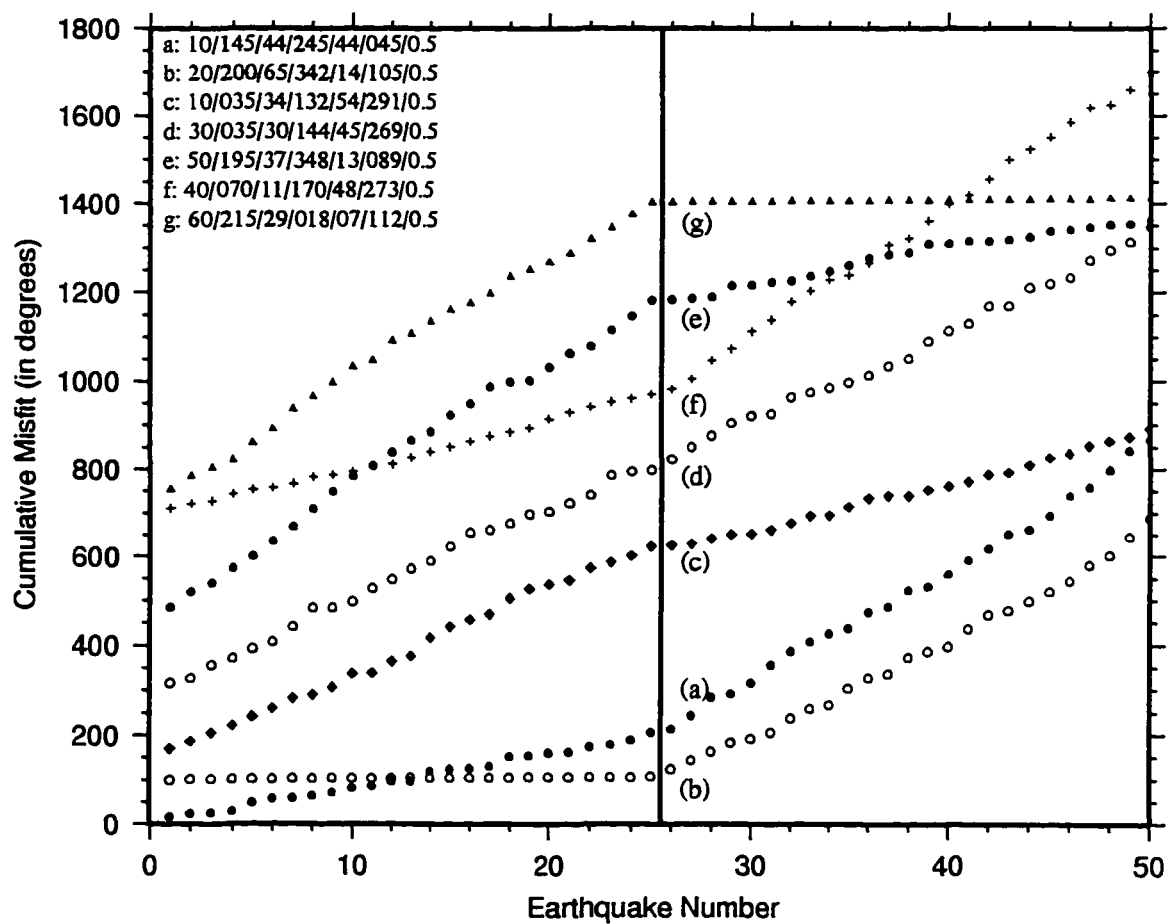


Figure 3.2 Cumulative misfit as a function of earthquake number for seven reference stress tensors. All but the lowest curve have been shifted upward for clarity. The earthquakes are the same as those in Figure 3.1. The reference stress tensors used to calculate the misfit of individual earthquakes are shown in the upper left corner. These stress tensors are represented by plunge and azimuth of σ_1 , σ_2 , σ_3 , and R (see text).

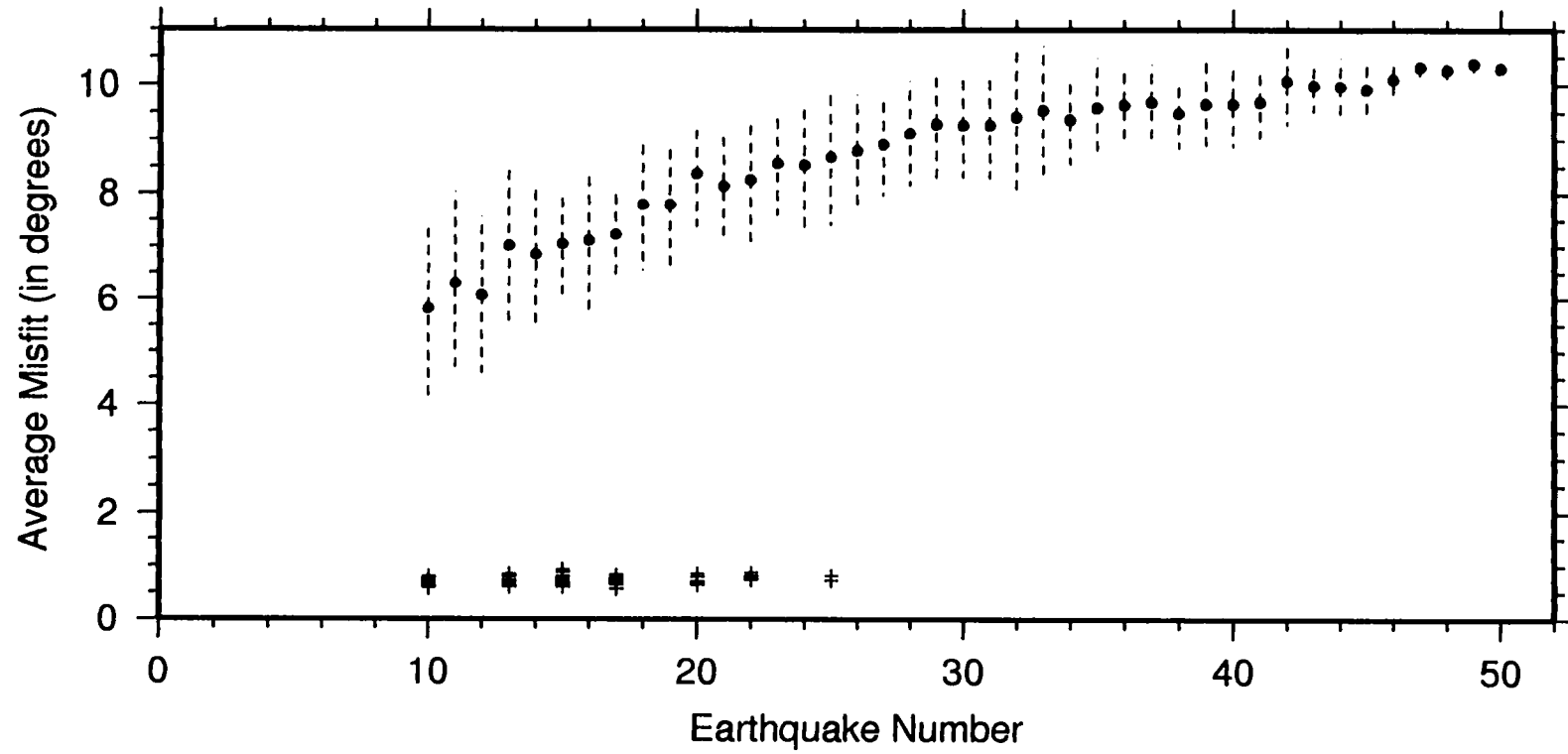


Figure 3.3 Average misfit (dots) and its standard deviation (dashed lines) as a function earthquake number. The data sets were selected randomly from 50 events which come from two stress regimes (Figures 3.1 and 3.2). The average misfits resulting from inversions of earthquakes from a single stress regime in Figure 3.1 are redrawn by pluses in the lower part of the figure.

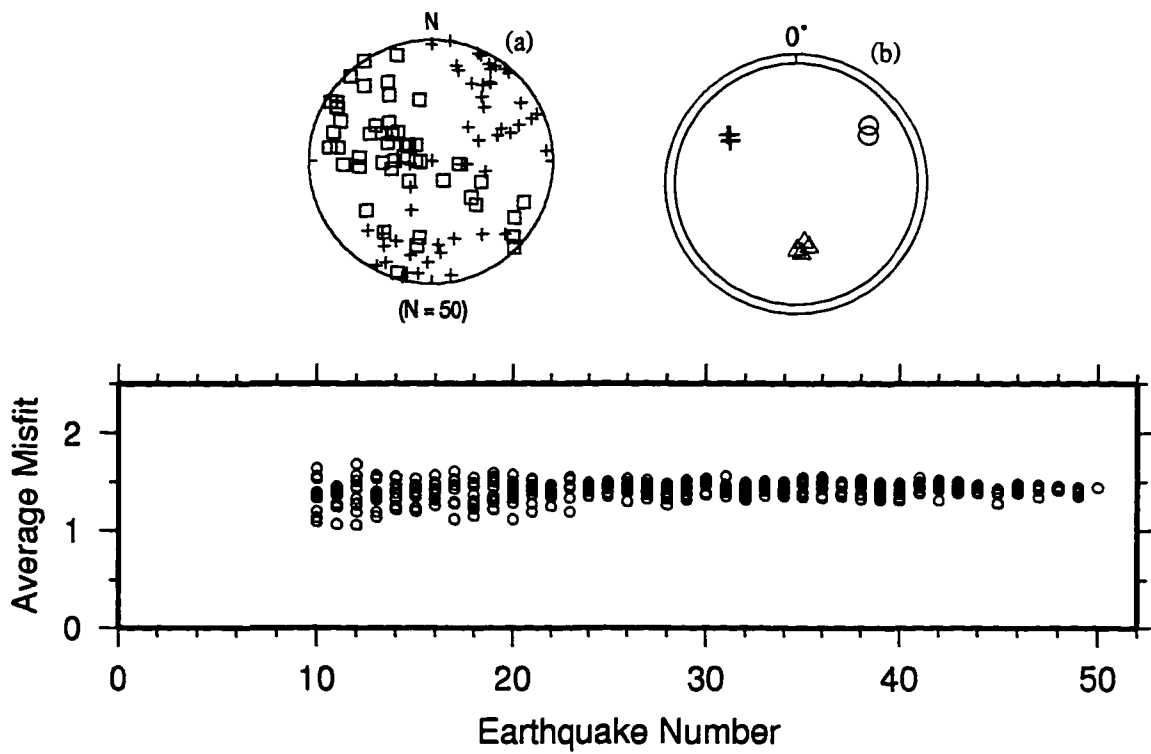


Figure 3.4 Average misfits as a function of earthquake number for data sets selected randomly from 50 events, which come from a single stress regime. (a) The orientation of P (pluses) and T (squares) axes of the 50 focal mechanisms plotted on a lower hemisphere, equal-area projection. (b) The greatest (circles), intermediate (triangles), and least (pluses) principal stress directions of the best fitting stress tensors from all the inversions.

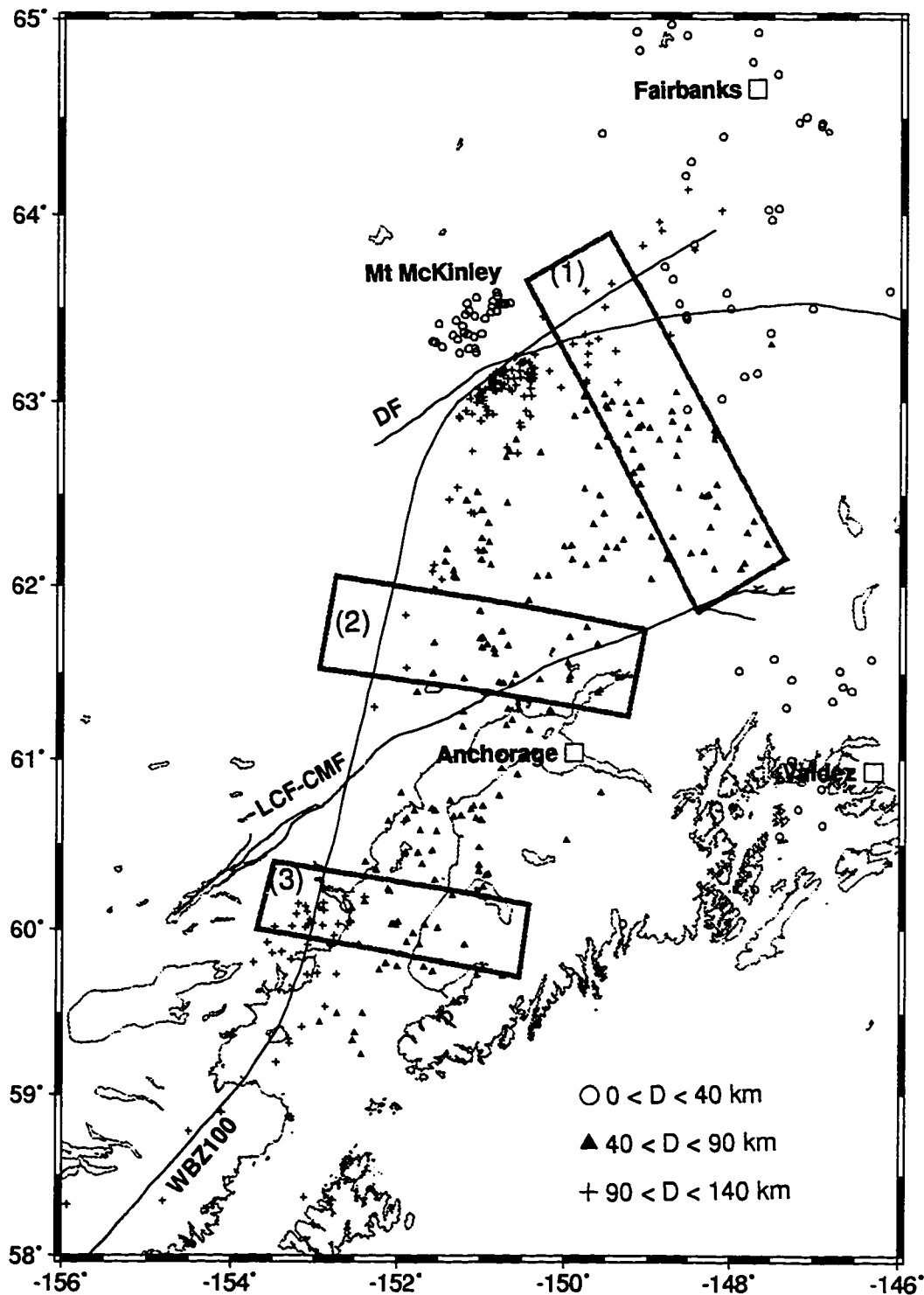


Figure 3.5 Epicenter map of small earthquakes ($M_L \sim 3.0$) with fault plane solutions in Alaska. The earthquakes in the areas enclosed by the three polygons are used to investigate the change of stress direction as a function of depth. Fault abbreviations: DF, Denali fault; LCF-CMF, Lake Clark fault and Castle Mountain fault; WBZ100, approximate surface projection of WBZ at 100 km.

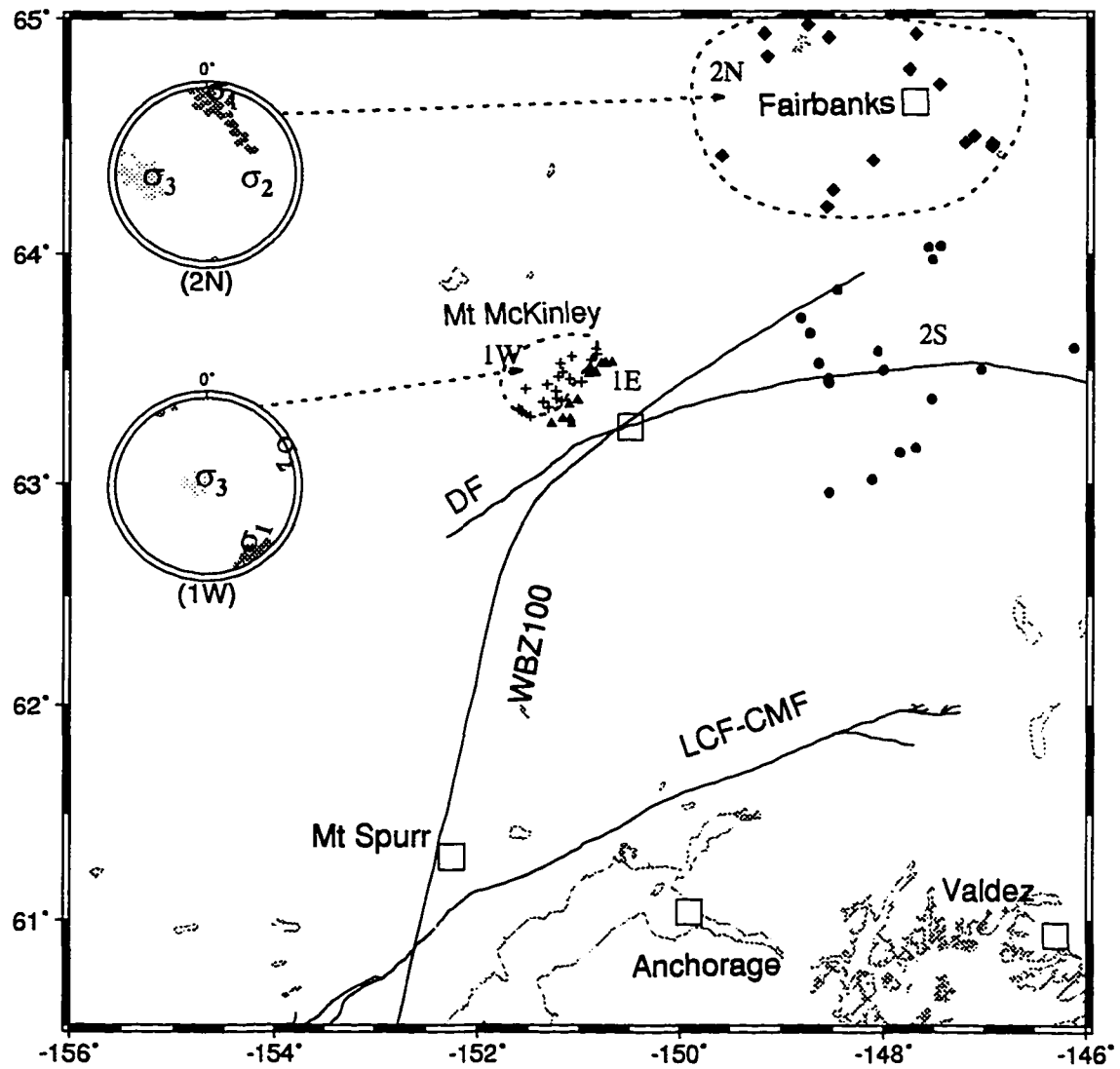


Figure 3.6 Epicenter map of small crustal earthquakes ($M_L \sim 3$) with fault plane solutions in Alaska and stereographic projection of the best fitting principal stress directions for two homogeneous data sets: 1W (crosses), west McKinley; 2N (diamonds) (Table 3.1). The inversions using the data from the earthquakes marked by triangles and dots did not yield meaningful results. The 95% confidence regions are defined by heavily and lightly shaded dots for the greatest and least principal stresses, respectively.

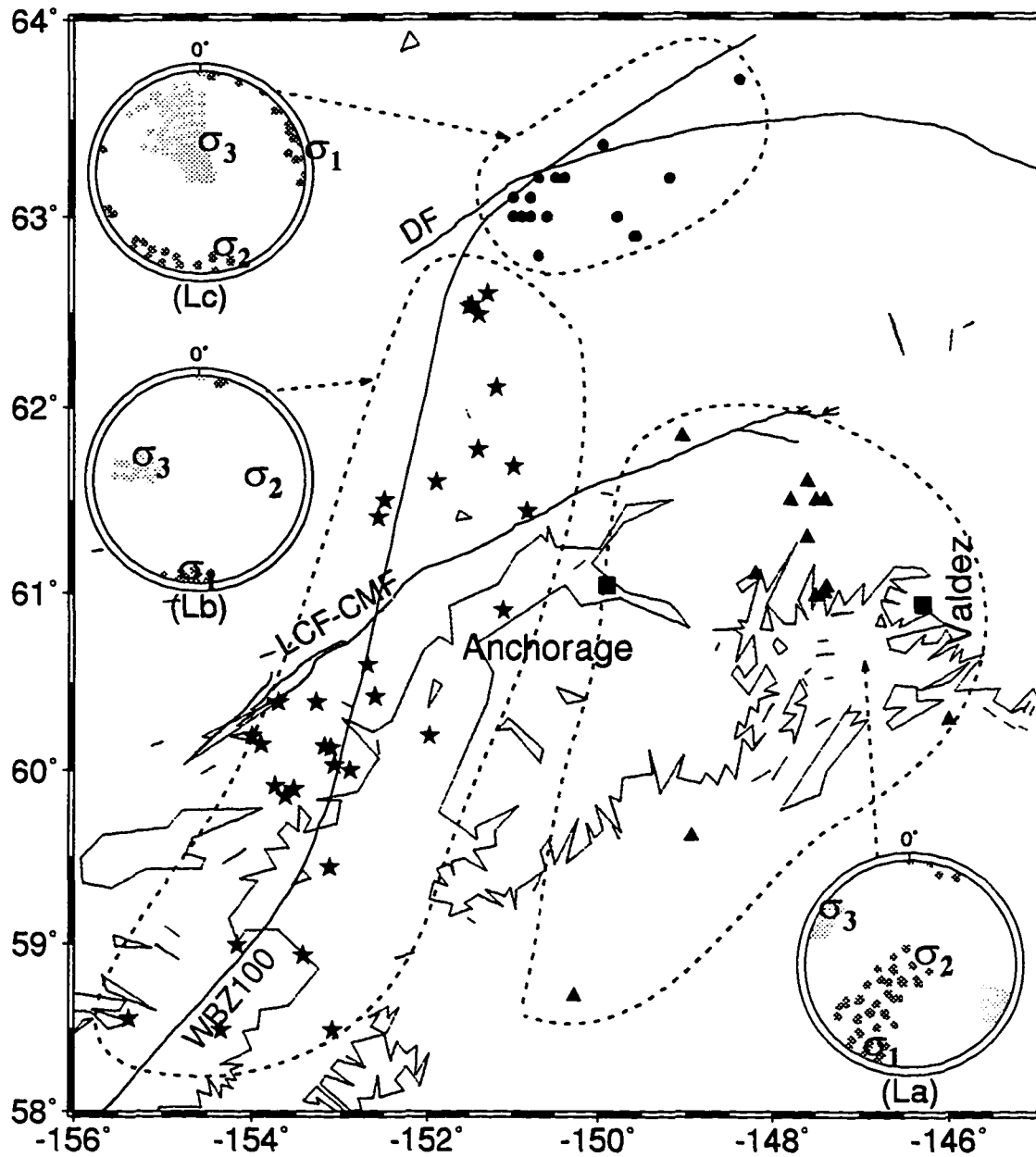


Figure 3.7 Epicenter map of large earthquakes ($M_s \sim 5$) with fault plane solutions in Alaska and stereographic projection of the best fitting principal stress directions for shallow WBZ events (triangles, set La in Table 3.1) and intermediate and deep WBZ earthquakes (stars, set Lb; dots, set Lc, in Table 3.1). The 95% confidence regions are defined by heavily and lightly shaded dots for the greatest and least principal stress, respectively

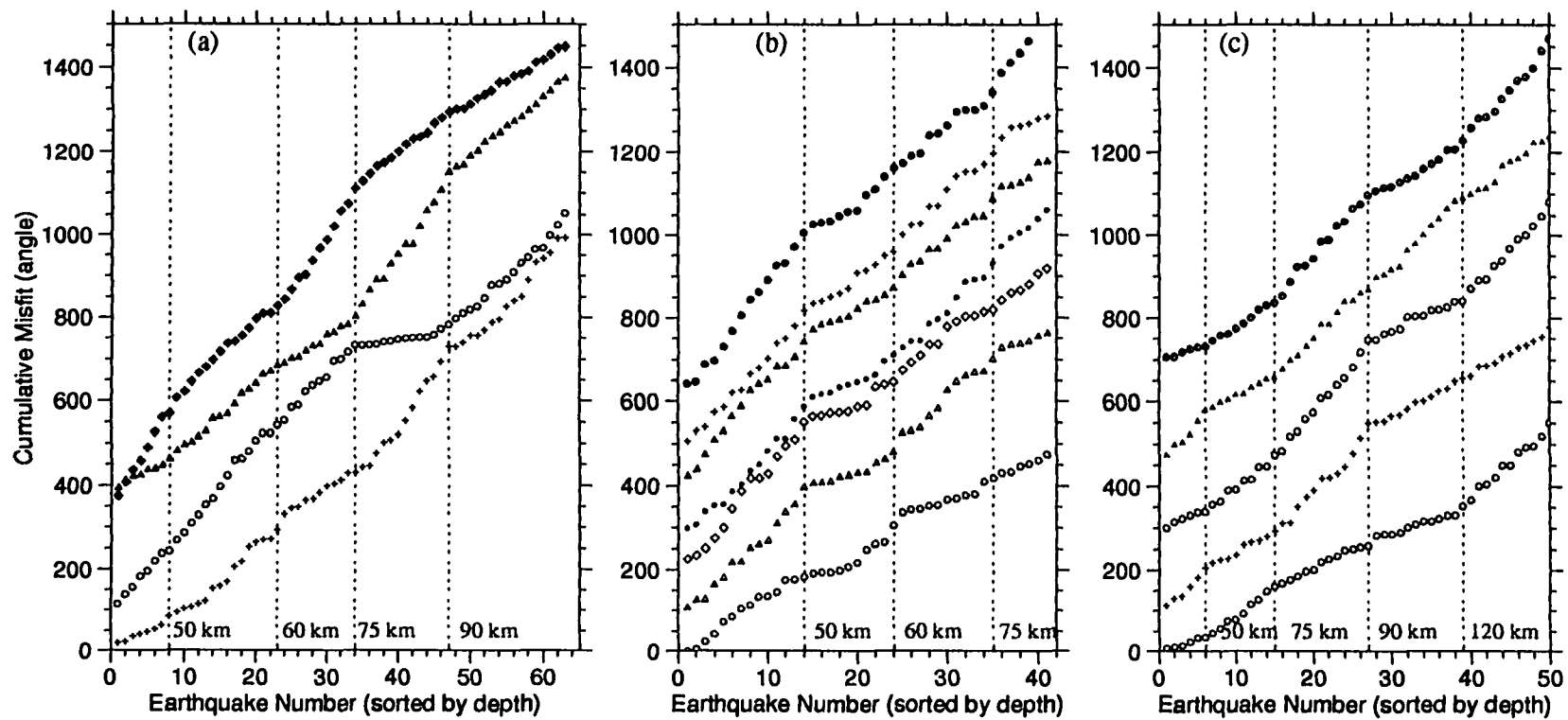


Figure 3.8 Cumulative misfit as a function of depth in polygon 1 (a), 2 (b), and 3 (c) defined in Figure 3.5. The depths at which stress directions change are indicated by vertical dashed lines. The curves with different symbols are based on several different test stress tensors for assumed stress directions. All but the lowest curve have been shifted upward for clarity.

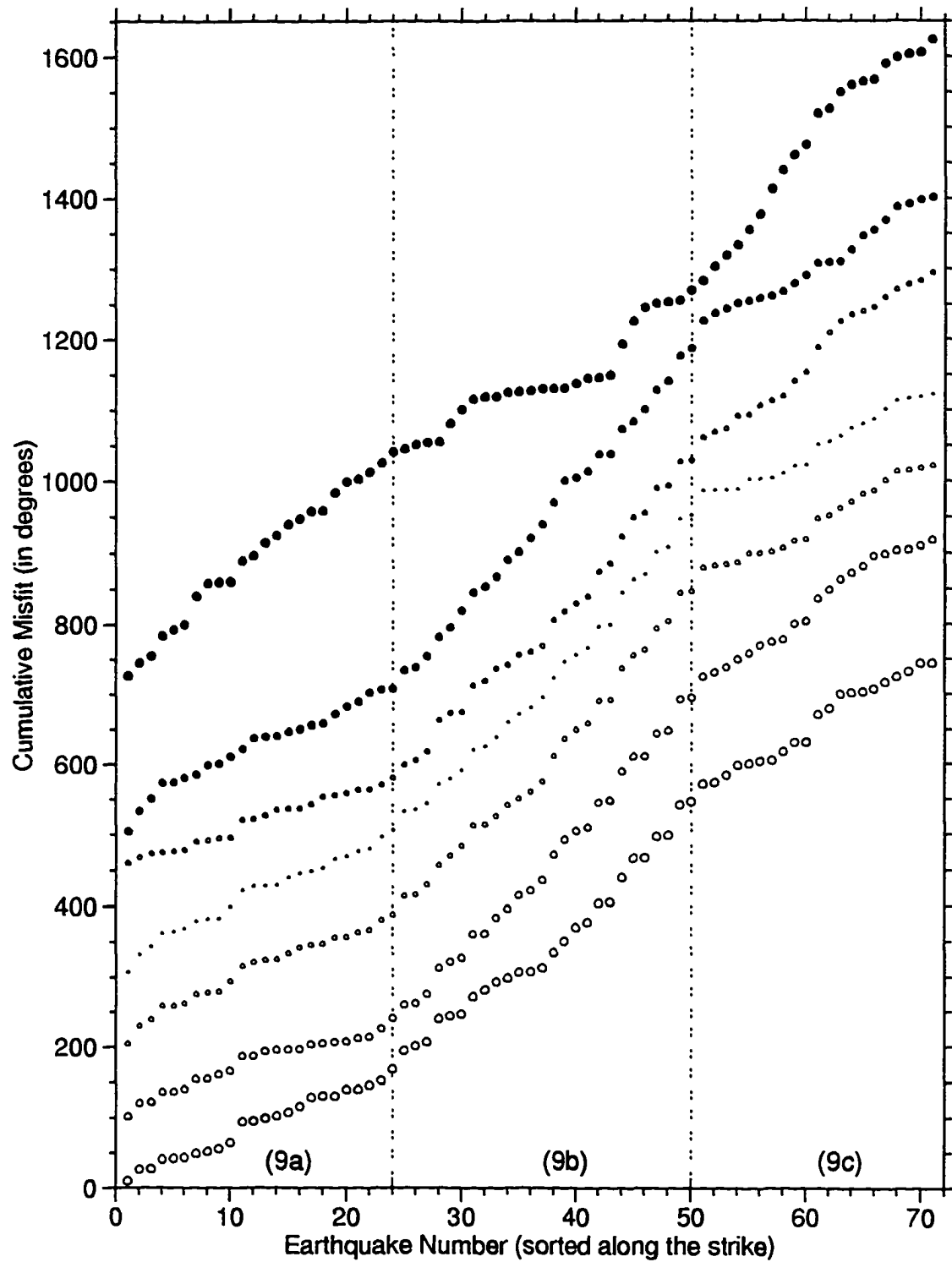


Figure 3.9 Cumulative misfit as a function of strike at depth 120 - 140 km using seven different test stress tensors. The changes of stress direction estimated around event number 24 and 50 separate the data set in this depth range into three sets (9a, 9b, and 9c, Table 3.1). Their principal stress orientations are shown in Figure 3.10. All but the lowest curve have been shifted upward for clarity.

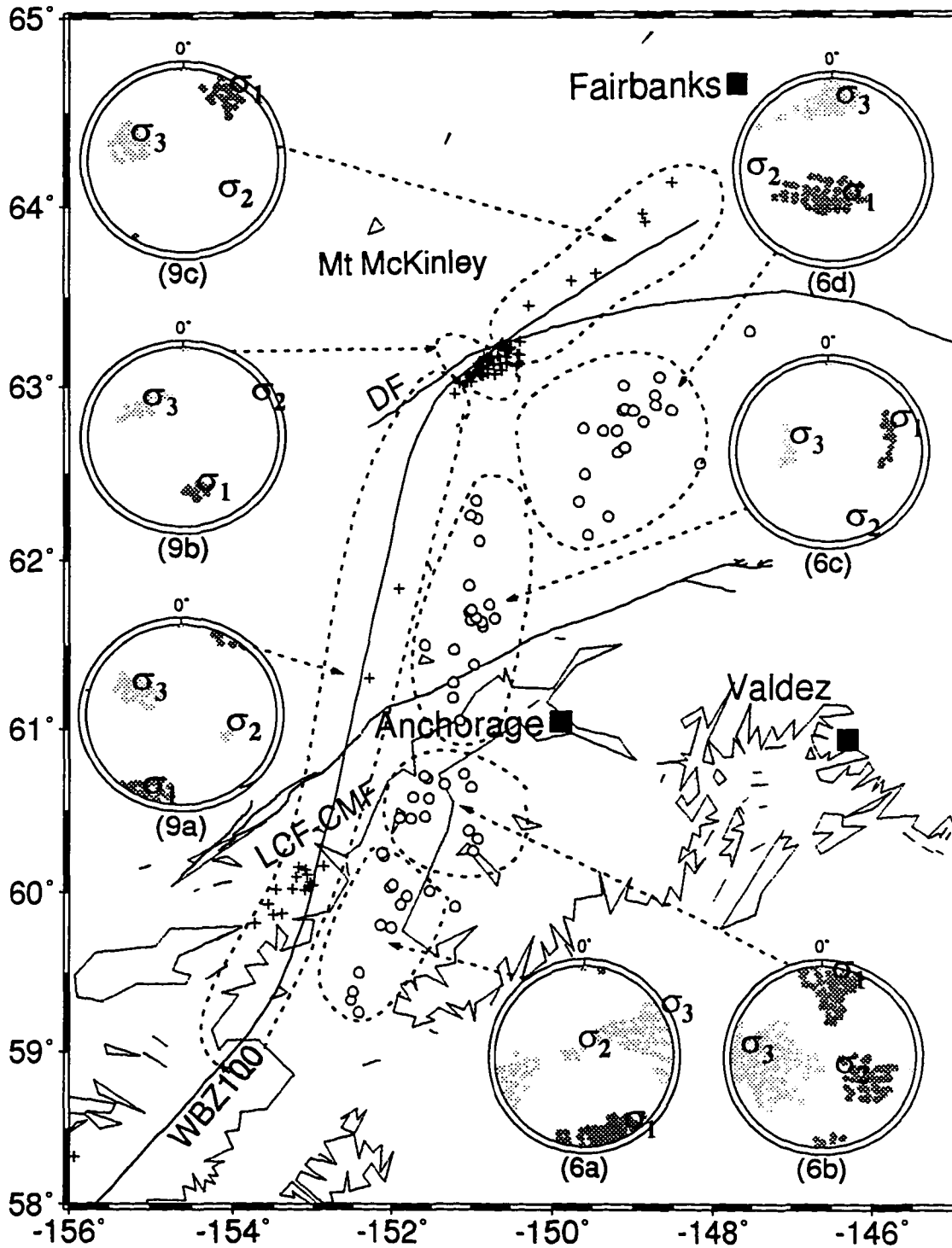


Figure 3.10 Epicenter map of small subcrustal earthquakes in the depth ranges 120-140 km (crosses), and 60-75 km (circles), together with stereographic projections of the best fitting principal stress directions for subsets selected based on cumulative misfit slopes. The subset numbers correspond to those in Table 3.1. Dashed contours outline the extent of the data sets. Inversion of data from earthquakes whose epicenters are not encircled by a dashed line did not yield meaningful results.

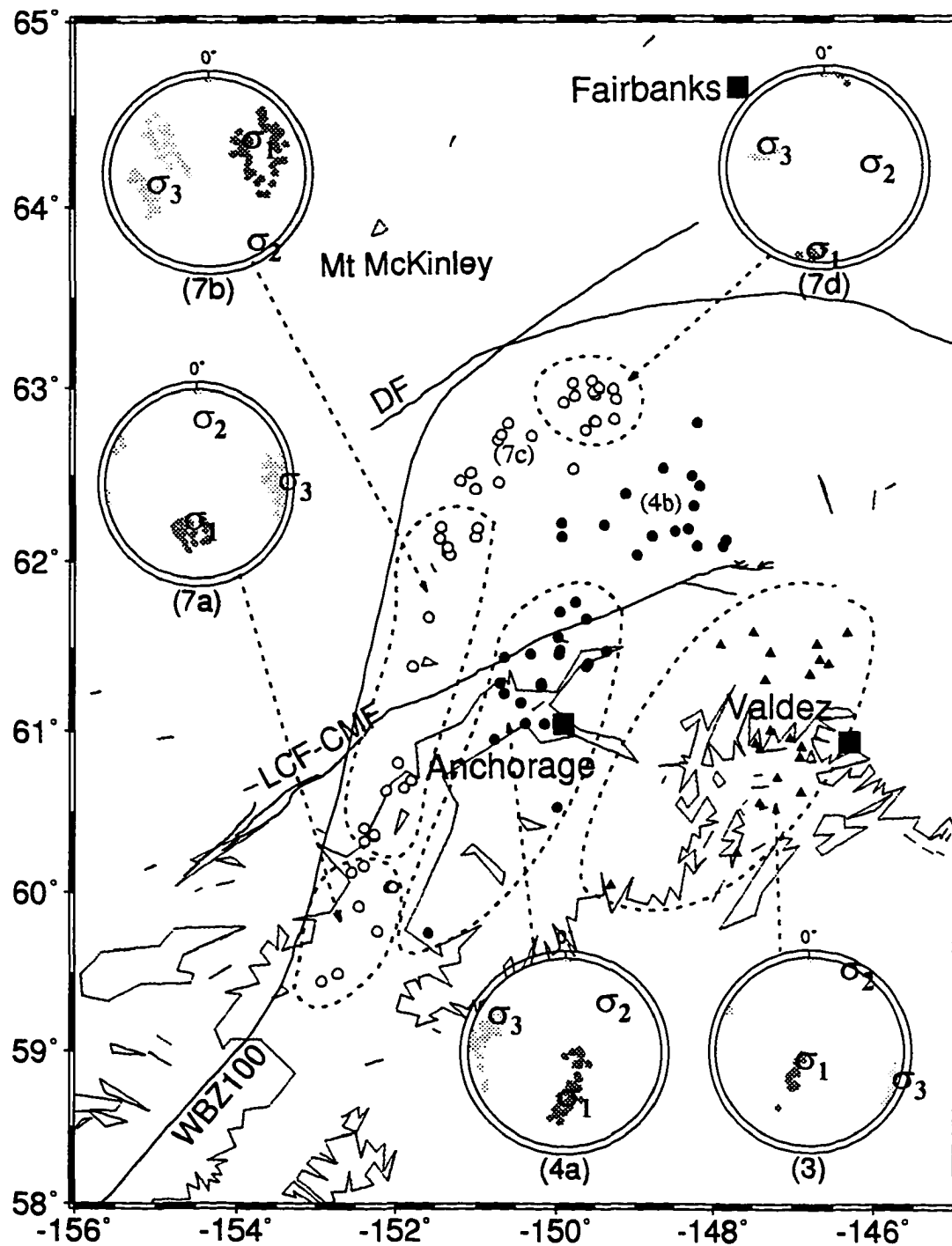


Figure 3.11 Epicenter map of small subcrustal earthquakes in the depth ranges 75 - 90 km (circles), 40 - 50 km (dots), and 0 - 40 km (triangles), together with stereographic projections of the best fitting principal stress directions for subsets selected based on cumulative misfit slopes (same as Figure 3.10).

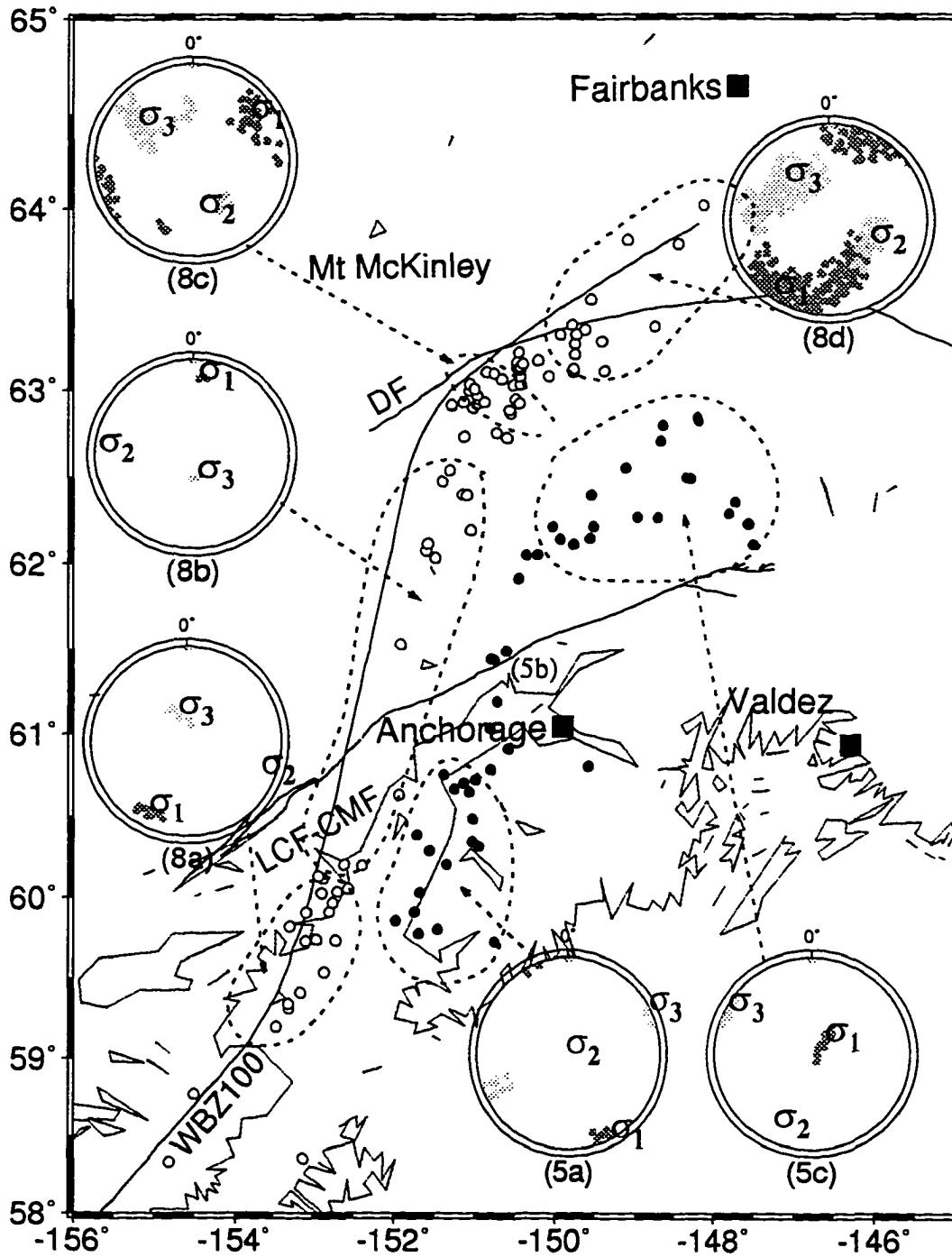


Figure 3.12 Epicenter map of small subcrustal earthquakes in the depth ranges 90 - 120 km (circles), and 50 - 60 km (dots), together with stereographic projections of the best fitting principal stress directions for subsets selected based on cumulative misfit slopes (same as Figure 3.10).

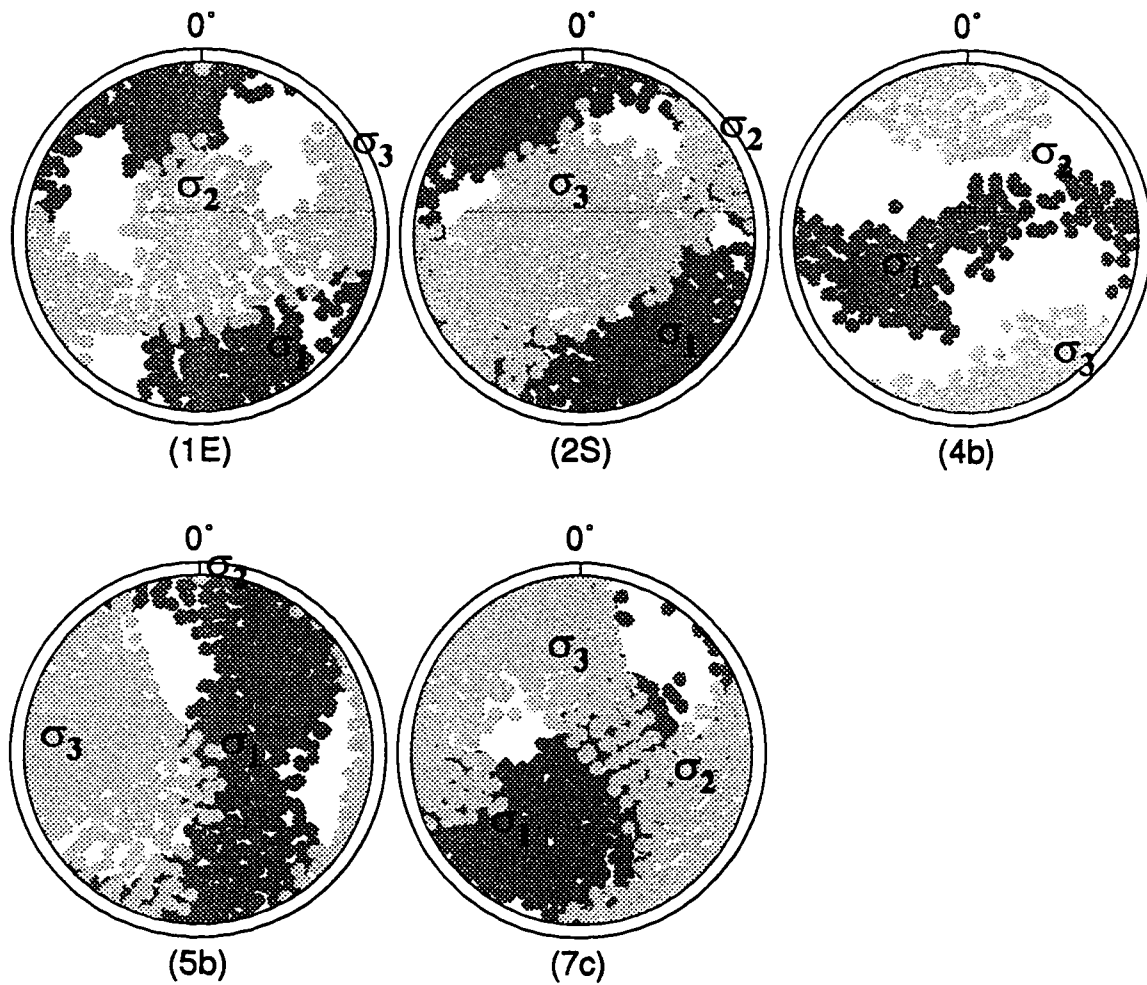


Figure 3.13 The principal stress directions of several inversions did not yield meaningful results. The epicenters of these earthquakes are shown in Figures 3.6, 3.11 and 3.12. The 95% confidence regions are defined by heavily and lightly shaded dots for the greatest and least principal stresses, respectively.

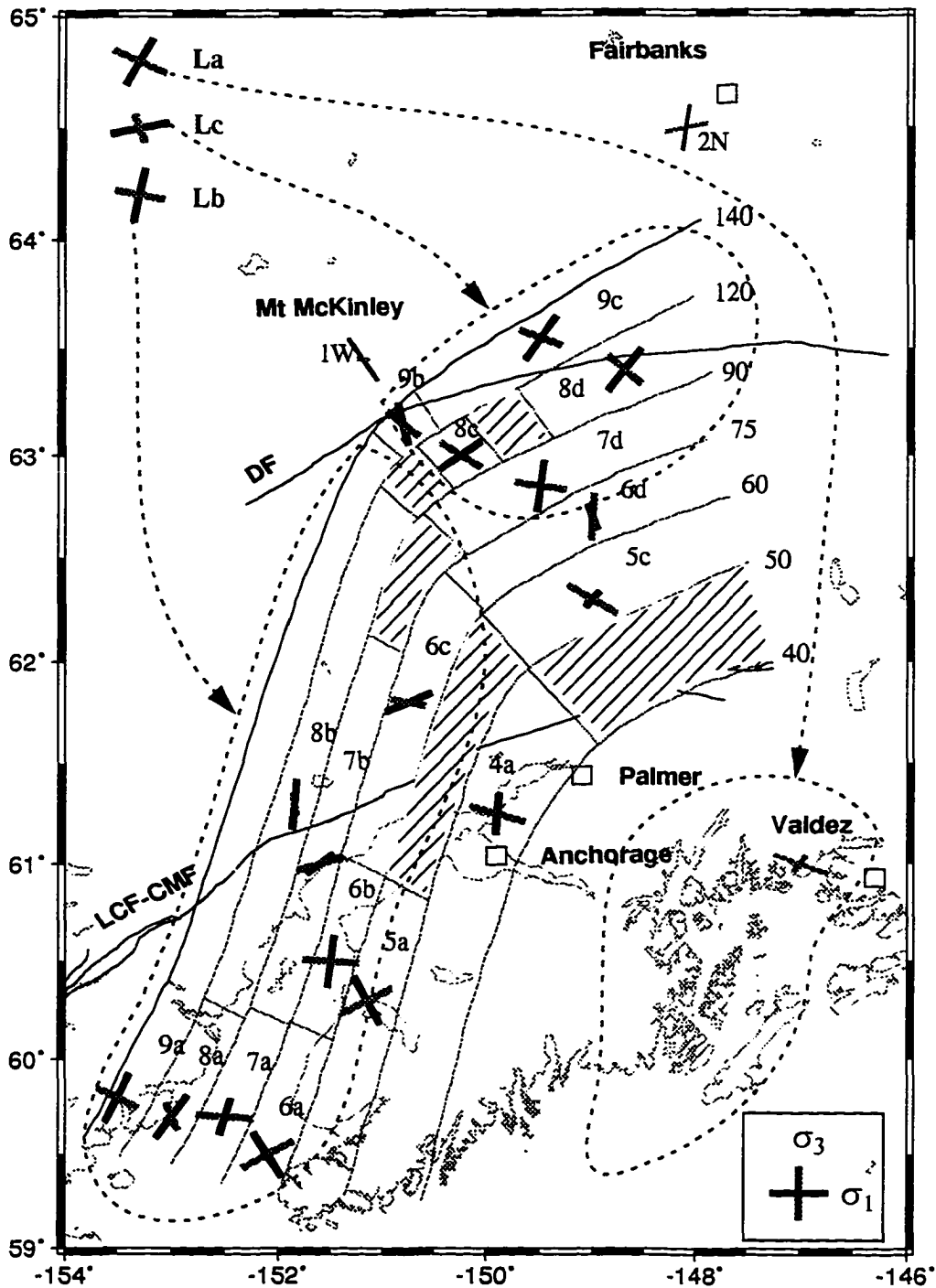


Figure 3.14 Map of stress directions in Alaska in the crust (thin bars) and in the subducting slab (thick bars) based on inversions of fault plane solutions of $M_L \sim 3$ earthquakes. The length of solid bars (σ_1 direction) and gray bars (σ_3 direction) are proportional to their dip with full length for horizontal (example at lower right) and zero length for vertical dip. The data set numbers are those used in Table 3.1. The boundaries within which each pair of stress directions is valid are defined by the lines of depth contours. In shaded volumes inversion attempts did not lead to meaningful results. The stress directions derived from the large earthquakes, shown at the top left, are valid for the Anchorage-Valdez (La) and the southern (Lb) and northern (Lc) parts of WBZ.

Chapter 4

Review of Interferometric SAR Theory

4.1 Introduction

A radar interferometer is formed by relating signals from two spatially separated antennas. The separation of the two antennas is called a baseline. The two antennas may be mounted on a single platform, the usual implementation for aircraft systems [Zebker and Goldstein, 1986], or a synthetic interferometer could be created by utilizing a single antenna on a satellite in nearly identical repeating orbits. For the latter case, even though the antennas do not illuminate the same area at the same time, the two sets of signals recorded during the two passes will be highly correlated if the scattering of the ground surface is unchanged between viewings.

Graham [1974] made the first interferometric measurements of topography with an airborne SAR, based on which the topography was estimated from the location of nulls in the coherent sum of two images acquired with separate antennas. *Zebker and Goldstein* [1986] were the first to estimate topography directly from the interferometric phase based on images acquired with an airborne L-band, single-pass

SAR. *Li and Goldstein* [1990] were the first to demonstrate that interferometry could be applied successfully to pairs of images where each image was acquired during a separate near-repeat satellite orbit. They generated interferograms from SEASAT data using the repeat-pass approach. The repeat-pass approach also has been applied to aircraft data by *Gray and Farris-Manning* [1993]. In addition to topography, repeat-pass INSAR can be used to detect surface displacement in the look direction of the radar. The capability was first shown by *Gabriel et al.* [1991]. The repeat-pass of C-band (radar wave length $\lambda = 5.66$ cm) ERS-1 INSAR has been used for measuring the velocity field of glaciers [e.g. *Goldstein et al.*, 1993; *Joughin et al.*, 1995; *Kwok and Fahnestock*, 1996], and displacement from earthquakes [e.g. *Massonnet et al.*, 1993, 1994; *Zebker et al.*, 1994a; *Peltzer and Rosen*, 1995; *Massonnet and Feigl*, 1995]. *Murakami et al.* [1995, 1996] demonstrated the potential of L-band ($\lambda = 23.5$ cm) repeat-pass JERS-1 INSAR to map the displacement field of earthquakes and detect crustal deformation. *Massonnet et al.* [1995] were the first to map the deflation associated with the eruption of Etna volcano by interferometric SAR. *Lu et al.* [1996], for the first time, detected long-term inflation of two volcanic vents at Katmai National Park, Alaska.

4.2 Basics of SAR Interferometry

The geometry of an interferometric SAR is shown in Figure 4.1. The interferometer acquires two images of the same scene with SARs located at S1 and S2. The first SAR is at altitude H. The range, r_0 , from the SAR at S1 to a point on the ground surface is determined by the ground range, y , and elevation, z . The range to the same ground point from the SAR at S2 differs from r_0 by Δ . For a single-pass system, such as TOPAR [*Zebker et al.*, 1992], two images are acquired simultaneously using separate antennas. In contrast, a repeat-pass interferometer

acquires a single image of the same area twice from two near-repeat orbits or flights. The distance between S1 and S2 is called the baseline, which has length B , and is tilted with respect to the horizontal by ξ .

We could view Figure 4.1 as a cross section of a SAR flight path. The following two equations relate the ground range and elevation to the range and look angle, θ ,

$$z = H - r_0 \cos \theta, \quad (4.1)$$

and

$$y = r_0 \sin \theta. \quad (4.2)$$

Referring to Figure 4.1 and applying the law of cosines, the range difference and look angle are related by

$$\cos\left(\frac{\pi}{2} - \theta + \xi\right) = \frac{B^2 + r_0^2 - (r_0 + \Delta)^2}{2r_0B}. \quad (4.3)$$

Solving for $\sin(\theta - \xi)$ yields [Rodriguez and Martin, 1992]

$$\sin(\theta - \xi) = \frac{B}{2r_0} - \frac{\Delta}{B} - \frac{\Delta^2}{2r_0B}. \quad (4.4)$$

Combining Equation 4.4 with Equations 4.1 and 4.2, we obtain [Rodriguez and Martin, 1992]

$$z = H - r_0[\cos \xi \sqrt{1 - \sin^2(\theta - \xi)} - \sin \xi \sin(\theta - \xi)], \quad (4.5)$$

and

$$y = r_0[\sin \xi \sqrt{1 - \sin^2(\theta - \xi)} + \cos \xi \sin(\theta - \xi)]. \quad (4.6)$$

Using range and range difference measured with a SAR interferometer, Equations 4.4-4.6 are solved to determine elevation and ground range. This is how interferometry could be used to measure topography.

Repeat-pass INSAR also can be used to measure any surface deformation that occurs between passes. Deformation in the direction toward or away from the radar

causes an additional change in range. Thus the total range difference between the two satellite passes is then

$$\Delta = \Delta_{topography} + \Delta_{deformation}, \quad (4.7)$$

where $\Delta_{topography}$ and $\Delta_{deformation}$ denotes the topography-dependent and deformation-dependent range difference, respectively.

In order to accurately estimate differential motion, the effect of topography must be removed from the interferogram. Topography and motion can be separated using a second interferogram which is acquired over the same area, sharing one orbit with the previous interferogram [e.g. *Gabriel et al.*, 1991; *Zebker et al.*, 1994a; *Peltzer and Rosen*, 1995]. The second interferogram must span an interval where no displacement occurs so that it is affected only by topography. The phase of this topography-only interferogram is unwrapped (discussed later) and scaled by the ratio of the baselines to simulate the effects of the topography in the original interferogram. A motion-only interferogram is obtained by subtracting the scaled, topography-only interferogram from the original interferogram. Alternatively, a Digital Elevation Model (DEM) [e.g. *Massonnet et al.*, 1993, 1994, 1995] can be used to simulate the topography-only interferogram.

4.3 Phase in Interferograms

To estimate elevation or differential motion, the range difference, Δ , must be known. This difference needs to be measured with an accuracy far greater than that obtainable with the normal range resolution of the SAR. Instead, this difference is measured using the phase information from a pair of complex SAR images. For a distributed target, a pixel in a complex image can be represented as

$$C_1 = \exp(-i\frac{4\pi}{\lambda}r_0)W_1 = \exp(-i\frac{4\pi}{\lambda}r_0)A_1e^{i\psi_1}, \quad (4.8)$$

where λ is the wave length of radar and W_1 is a complex Gaussian random variable with amplitude A_1 and phase ψ . Because phase is uniformly distributed, ψ are unknown. Therefore a single complex image can not be used to determine range information. However, a second SAR complex image could be obtained after the SAR flies over the same area a second time.

$$C_2 = \exp(-i\frac{4\pi}{\lambda}(r_0 + \Delta))W_2 = \exp(-i\frac{4\pi}{\lambda}(r_0 + \Delta))A_2e^{i\psi_2}. \quad (4.9)$$

A complex interferogram is constructed as the product of one complex SAR image with the complex conjugate of the second. A pixel in the interferogram can be expressed as

$$C_1C_2^* = \exp(i\frac{4\pi}{\lambda}\Delta)\exp[i(\psi_1 - \psi_2)]A_1A_2. \quad (4.10)$$

The phase of a pixel in the interferogram is given by

$$\phi = [(\frac{4\pi}{\lambda}\Delta + (\psi_1 - \psi_2))_{\text{mod}(2\pi)}]. \quad (4.11)$$

If the scattering character of the ground surface is undisturbed, coherence can be maintained during the two passes, thus, $(\psi_1 - \psi_2) \rightarrow 0$. Equation 4.11 could become

$$\phi = (\frac{4\pi}{\lambda}\Delta)_{\text{mod}(2\pi)}. \quad (4.12)$$

From Equation 4.12, the phase difference is still only known modulo 2π . Therefore, a phase-unwrapped algorithm [e.g. *Goldstein et al.*, 1988] is needed to remove the modulo 2π ambiguity. The range difference for repeat-pass INSAR is determined using

$$\Delta = \frac{\lambda}{4\pi}\phi, \quad (4.13)$$

where ϕ denotes the unwrapped interferometric phase difference.

4.4 The Effect of Baseline and Topography on Range Difference

To help illustrate how range difference is related to ground range and topography and how the baseline affects this relationship, several approximations are derived in this section. The baseline is usually expressed in terms of its components perpendicular to, B_{\perp} , and parallel to, B_{\parallel} , a reference look direction (Figure 4.2) [Solaas and Coulson, 1994]. A convenient choice is to let the center look angle, θ_c , define the reference look direction [e.g. Joughin, 1995]. The two components of baseline are related by

$$B_{\perp} = B \cos(\theta_c - \xi), \quad (4.14)$$

and

$$B_{\parallel} = B \sin(\theta_c - \xi). \quad (4.15)$$

The typical values for r_0 and Δ are 780 km and several meters, respectively. Consider $r_0 \gg \Delta$, the expression given by Equation 4.4 can be approximated as

$$B \sin(\theta - \xi) = -\Delta + \frac{B^2}{2r_0}. \quad (4.16)$$

The look angle can be expressed as $\theta = \theta_c + \delta\theta$, and $\delta\theta$ is the difference of look angle from the center look angle. Thus

$$B \sin(\theta - \xi) = B \sin(\theta_c - \xi + \delta\theta) = B_{\parallel} \cos \delta\theta + B_{\perp} \sin \delta\theta. \quad (4.17)$$

Combining Equation 4.16 and 4.17 and solving for the range difference yields [Joughin, 1995]

$$\Delta = -B_{\perp} \sin \delta\theta - B_{\parallel} \cos \delta\theta + \frac{B^2}{2r_0}. \quad (4.18)$$

For most spaceborne SARs, such as ERS-1/2, $\delta\theta$ varies only a few degrees across the swath. This implies that the range difference, Δ , is an almost linear

function of $\delta\theta$, with its slope determined by B_{\perp} and its intercept determined, in part, by B_{\parallel} . Furthermore, Equation 4.18 could be approximated into,

$$\Delta \approx -B_{\parallel}. \quad (4.19)$$

Thus, range difference is controlled by B_{\parallel} . This is the parallel-ray approximation used by some researchers [e.g. *Zebker and Goldstein, 1986; Zebker et al., 1994*]

Referring to Figure 4.2, we see that

$$\sin \delta\theta = \frac{n_c}{r_0}, \quad (4.20)$$

where n_c is the perpendicular distance from the target point to the center slant-range direction. This distance can be expressed as

$$n_c = y \cos \theta_c + z \sin \theta_c - y_c \cos \theta_c. \quad (4.21)$$

Plugging these results into Equation 4.18 yields [*Joughin, 1995*]

$$\Delta = -\frac{B_{\perp}}{r_0}[y \cos \theta_c + z \sin \theta_c] - B_{\parallel} \cos \delta\theta + \frac{B^2}{2r_0} + const. \quad (4.22)$$

This approximation indicates that the effect of topography and ground range on range difference is primarily determined by B_{\perp} , with only weak, nonlinear terms affected by B_{\parallel} .

For a flat surface (i.e., $z = 0$), the range difference is given by

$$\Delta_{flat} = -\frac{B_{\perp}}{r_0}y \cos \theta_c - B_{\parallel} \cos \delta\theta_{flat} + const, \quad (4.23)$$

where the $\delta\theta_{flat}$ is the derivation of the look angle from the center angle for a flat surface. From this equation it is apparent that Δ_{flat} varies almost linearly with y . This causes a flat surface to appear as nearly linear phase, called phase ramp, in an interferogram. When the surface is not flat, the topography appears as phase functions superimposed on the phase ramp. It is often useful to subtract

the phase ramp for a flat surface from the range difference to examine the effect of topography. The component of the range difference directly affected by topography is then given by

$$\Delta_{topography} = \Delta - \Delta_{flat} \quad (4.24)$$

Based on Equations 4.18 and 4.24, and several approximations, we obtain

$$\Delta_{topography} = \frac{-B_{\perp}}{\sin \theta_c r_0} z + const \quad (4.25)$$

Thus, after removing the phase ramp, the range difference has an approximately linear relation to surface elevation (of course, we assume no deformation of the ground surface between the two passes).

Several observations can be made from the approximations given in this section. The major effect of B_{\parallel} is to determine a phase constant for the interferogram. Terms containing B_{\parallel} are only weakly affected by changes in the topography. On the other hand, the sensitivity of the interferometer to topography is directly proportional to B_{\perp} .

A more realistic approximation for the ramp phase assumes an ellipsoidal earth. Over the area covered by a SAR image, it is often possible to further approximate the earth as a sphere. In this case, the radius of the sphere is equal to the radial distance from the center of the ellipsoid to the point on the surface corresponding to the center of the image. The GEM6 ellipsoid is used as model of the earth by the ASF processor [Olmsted, 1993]. This ellipsoid is parameterized by its major axis, e_{major} , and minor axis, e_{minor} . The radius of the earth at latitude, θ_{lat} , is determined by

$$R_e = \sqrt{(e_{major} \sin \theta_{lat})^2 + (e_{minor} \cos \theta_{lat})^2}. \quad (4.26)$$

The look angle for a point with $z = 0$ is computed by

$$\theta_{z=0} = \arccos\left(\frac{r_0^2 + 2HR_e + H^2}{2r_0(R_e + H)}\right). \quad (4.27)$$

So, the ramp phase is obtained by

$$\phi_{z=0} = \frac{4\pi}{\lambda} \left(-B_{\perp} \sin \theta_{z=0} - B_{\parallel} \cos \theta_{z=0} + \frac{B^2}{2r_0} \right). \quad (4.28)$$

Equations 4.26-28 are used to compute the phase ramp, which should be removed from the interferograms.

We may compare the sensitivity of the phase measurement to the topography and displacement. By differentiating the equation 4.7 with respect to height, and combining Equations 4.13 and 4.25, we find

$$\frac{d\phi}{dz} = -\frac{4\pi}{\lambda} \frac{B_{\perp}}{\sin \theta_c r_0}. \quad (4.29)$$

By differentiating the Equation 4.7 with respect to deformation, we get

$$\frac{d\phi}{d\Delta_{deformation}} = \frac{4\pi}{\lambda}. \quad (4.30)$$

Because $r_0 \gg B$ is always true, it is evident from Equations 4.29 and 4.30 that a much more sensitive dependence of phase results from deformation than from topographic variation. In other words, the system is more sensitive in an absolute sense to surficial change than to the topography itself. It is also noticed that the sensitivity to topography also depends on the baseline length while the sensitivity to deformation is independent of baseline length. Thus, while radar interferometry can be used to measure topography to an accuracy of meters, deformation may be determined at the centimeter or millimeter level.

4.5 Errors in Elevation and Deformation Estimates

The uncertainties in elevation derived by INSAR are caused by two types of errors [Rodriguez and Martin, 1992]. The first type are intrinsic errors which are caused

by uncertainties in the parameters used to estimate the surface elevation; the second are location-induced errors, which occur when errors in the estimate of ground range cause the height estimate to be attributed to the wrong location. For relatively flat surfaces, location-induced errors are negligible, while for steeper surfaces they can be significant. Only intrinsic errors are considered here for simplicity.

Differentiating 4.1, 4.2, and 4.15 with respect to each individual parameter, we obtain the height uncertainties associated with each parameter. The effect of range error on elevation error [*Li and Goldstein, 1990; Rodriguez and Martin, 1992*] is given by

$$\delta z_{r_0} = -\cos\theta\delta r_0. \quad (4.31)$$

Range errors are caused by errors in the system clock timing and propagation delay [*Li and Goldstein, 1990*]. Errors in the estimation of satellite altitude are directly related to the elevation error by [*Li and Goldstein, 1990; Rodriguez and Martin, 1992*]

$$\delta z_H = \delta H. \quad (4.32)$$

The error in the estimate of the tilt angle causes an error in the elevation estimate, which can be expressed as

$$\delta z_\xi = r_0 \sin\theta\delta\xi. \quad (4.33)$$

The error in elevation is related to the error in the estimate of baseline length [*Rodriguez and Martin, 1992*] by

$$\delta z_B = r_0 \tan(\theta - \xi) \sin\theta \frac{\delta B}{B}. \quad (4.34)$$

Because of the $\tan(\theta - \xi)$ factor, errors of this type vary greatly with tilt angle. Relatively small errors occur when $\theta \sim \xi$ (i.e., $B_{\parallel} \sim 0$), while much larger errors occur when $(\theta - \xi) \sim \frac{\pi}{2}$ (i.e., $B_{\perp} \sim 0$). It has been shown by *Li and Goldstein* [1990] that the baseline error must be smaller than 1 m in order to produce satisfactory

DEM. The required accuracy may exceed the accuracy of baseline estimates derived from the satellite orbital data. As a result, the baseline usually has to be estimated using tie points (known elevations) within a scene [e.g. *Zebker et al.*, 1994b].

Because phase is used to estimate elevation, phase errors also contribute to the topographic error. The relationship between phase error and topographic error [Rodriguez and Martin, 1992] is given by

$$\delta z_\phi = \frac{-\lambda r_0 \sin \theta}{4\pi B \cos(\theta - \xi)} \delta \phi. \quad (4.35)$$

The phase error is caused by the thermal noise in the SAR system and environmental changes of the surface target. The elevation error caused by phase errors is inversely proportional to the baseline length so that long baselines are important for the reduction of elevation error. But long baselines cause more decorrelation, which increases the phase error and, thus, the elevation error. This requires that these opposing influences of baseline length on elevation error be balanced by choosing a length to minimize elevation error [Rodriguez and Martin, 1992].

The uncertainties in the estimation of differential motion are caused by the phase error and the error in baseline estimate. Error in deformation is related to error in phase by

$$\delta \Delta_{deformation} = \frac{\lambda}{4\pi} \delta \phi. \quad (4.36)$$

Errors in the baseline estimate introduce errors into the estimates of differential motion because the effect of topography is removed incorrectly. This error is dominated by a phase ramp, which can be expressed as

$$\delta \phi_{ramp} = \frac{4\pi}{\lambda} [\delta B_\perp \sin \delta \theta + \delta B_\parallel \cos \delta \theta + \frac{B}{r_0} (\delta B_\perp + \delta B_\parallel)]. \quad (4.37)$$

Because the error is in the form of a ramp, the error in the differential motion between points increases as the distance between them increases. Let's assume an interferogram with 50 km in dimension, and errors in δB_\perp and δB_\parallel of 1 m (I could

not tolerate such large errors!). Then the deformation error could be at most 5 cm for the whole image caused by the ramp phase.

4.6 Correlation in INSAR Images

Correlation coefficients are a quantitative way to assess coherence of images. This section examines the causes of decorrelation between complex SAR images. Correlation coefficients are important also because the correlation between images determines the amount of phase error and, thus, the accuracy of elevation and differential-motion estimates. *Zebker and Villasenor* [1992] listed three sources of decorrelation, each characterized by a corresponding correlation coefficient. Thermal decorrelation, $\rho_{thermal}$, is caused by the presence of uncorrelated-noise sources, while spatial decorrelation, $\rho_{spatial}$, results when the target is viewed from different positions. For repeat-pass INSAR environmental changes such as moisture condition, vegetation, and snow and ice between passes cause temporal decorrelation, $\rho_{temporal}$. The total correlation coefficient is the multiple combination of individual correlation coefficients.

$$\rho = \rho_{thermal}\rho_{spatial}\rho_{temporal}\rho_{other} \quad (4.38)$$

ρ_{other} represent the decorrelation coefficient caused by misregistration, interpolation, and other processing errors. The estimation of correlation coefficients from two SAR images can be calculated by

$$\rho = \frac{\Sigma C_1 C_2^*}{\sqrt{\Sigma |C_1|^2 \Sigma |C_2|^2}} \quad (4.39)$$

The $\rho_{spatial}$ between echoes varies approximately linearly, decreasing from unity at zero baseline length to zero at critical baseline

$$B_c = \frac{\lambda r}{2R_y \cos \theta} \quad (4.40)$$

where R_y is the ground range resolution. For ERS-1 ($\lambda = 56.6$ mm) the critical baseline is about 1100 m. The JERS-1 SAR has critical baseline of 7 km with wavelength of 23.5 cm.

Based on the critical baseline, for optimal system performance, the baseline must be large enough to give sufficient phase sensitivity to height, yet small enough as to not introduce too much decorrelation noise. Therefore, this defines a trade-off in interferometer design.

Given ρ calculated based on two SAR images, the phase standard deviation can be

$$\delta\phi = \frac{1}{\sqrt{(2N_l)}} \frac{\sqrt{(1-\rho^2)}}{\rho} \quad (4.41)$$

where N_l is the number of looks used for producing the interferogram. Because SAR is a coherent radar, each pixel obtained suffers from the fading noise (speckle). Multiple pixels, or so-called multilooks, are usually used to reduce the phase variation at the expense of resolution. With this procedure, groups of adjacent pixels in the image are replaced by their averages.

Equation 4.41 shows that the standard deviation of the phase decreases with the increase of correlation coefficients, and thus the resolution of topography or deformation produced by INSAR increases. The resolution of topography can be obtained by combining Equations 4.35 and 4.41

$$\delta z_\phi = \frac{-\sqrt{2}\lambda r_0 \sin\theta}{8\pi B \cos(\theta - \xi)} \frac{\sqrt{(1-\rho^2)}}{\rho\sqrt{N_l}} \quad (4.42)$$

The resolution of deformation can be obtained based on Equation 4.41

$$\delta\Delta_{deformation} = \frac{-\sqrt{2}\lambda\sqrt{(1-\rho^2)}}{8\pi\rho\sqrt{N_l}} \quad (4.43)$$

4.7 Phase Unwrapping

The interferometric phase needs to be unwrapped to remove the modulo- 2π ambiguity before estimating the topography. A simple way to do this is to first difference the phase at each pixel, and then to integrate the result. Direct application of this approach allows local errors to propagate, causing global errors [Goldstein *et al.*, 1988]. These errors must be isolated before an algorithm, which uses integration, can succeed. The basic idea of unwrapping the phase is to choose the paths of integration that lead to a correct solution [Goldstein *et al.*, 1988]. A fundamental assumption is that the resolution is fine enough so that the true phase does not change by more than $\pm\pi$ between adjacent pixels. In accordance with this assumption, the phase image, which is modulo 2π , is differenced so that phase is wrapped into the interval $(-\pi, \pi]$. This leads to errors when the phase difference exceeds the assumed limits. Such errors can result from rapid change of the underlying topography or differential motion.

The unwrapped solution should be independent of the path of integration. This implies that in the error-free case the integral of the differenced phase about a closed path should equal zero, and that non-zero results are caused by errors. Thus, inconsistencies (local errors) are detected by summing the phase difference clockwise around the closed paths formed by each set of four pixels that are mutual neighbors. An inconsistency is found when summation yields a value of $\pm 2\pi$ rather than 0. These points, called residues, are referred to as positively or negatively charged, depending on their sign [Goldstein *et al.*, 1988]. Integration of the differenced phase about a closed path yields a value equal to the sum of residues contained within the path. In order to obtain a correct solution, paths of integration that encircle a net charge must be avoided. This is done by connecting opposite charged residues with branch cuts, which are lines that the path of inte-

gration is restricted from crossing. When all the residues are connected by branch cuts, phase unwrapping can be completed by integrating the differenced phase subject to the rule that paths of integration can not cross branch cuts. Therefore, we can integrate the phase in the interferogram, and unwrapping is finished.

4.8 Limitations of the interferometric technique

1) Constructing interferograms requires that radar echoes acquired on the two or three passes must correlate with each other, that is, the signal must be substantially similar over a significant period of time. Physically, this translates to a requirement that the ground scattering surface be relatively undisturbed at the radar wavelength scale between measurements. Several studies addressed this phenomenon, both theoretically [e.g. *Li and Goldstein, 1990*], and experimentally [e.g. *Zebker and Villasenor, 1992; Gray et al., 1993*] quantified the temporal decorrelation process and found that different surfaces decorrelate at different rates. This limits the applicability of the approach to areas where the scattering surface does not change with time. Some regions, such as a desert area, which may exhibit very little decorrelation over long periods, are ideal field for SAR interferometry.

2) SAR system designs are not optimum, which limits the resolution of the interferogram. First, due to foreshortening or layover effects, in areas where the surface slope approaches the incidence angle, the ground range resolution becomes much larger than the output range pixel spacing, so that a single measurement characterizes many output pixels. Since we map the center of the resolution cell, several points in the output grid remain unfilled. This effect dominates at low incidence angles such as 23° used by ERS-1/2. The second effect is that of shadowing. Similar to optical shadows, radar shadows are formed when a taller object intercepts the illumination that would have illuminated a shorter object behind the

taller. Since no echo is available in these regions, no phase estimate is available.

3) Unwrapping is challenging work. The ability to unwrap arbitrary phase fields depends on two factors: the noise level in the images and interferometric fringe spacing. Since the fringe rate depends on local surface slope, typically it is more difficult to estimate the phase reliably in rough terrain than in flat terrain.

4.9 References

- Gabriel, A. K., R. M. Goldstein, and H. A. Zebker, Mapping small elevation changes over large areas: differential radar interferometry. *J. Geophys. Res.*, *94*, 9183-9191, 1989.
- Goldstein, R. M., H. A. Zebker, and C. L. Werner, Satellite radar interferometry: Two-dimensional phase unwrapping, *Radio Science*, *23*, 713-720, 1988.
- Goldstein, R. M., H. Engelhardt, B. Kamb, and R. M. Frolich, Satellite Radar Interferometry for Monitoring Ice Sheet Motion: Application to an Antarctic Ice Stream, *Science*, *262*, 1525-1530, 1993.
- Graham, L. C., Synthetic interferometer radar for topographic mapping. *Proc. of the IEEE*, *62*, 763-768, 1974.
- Gray, A. L., and P. J. Farris-Manning, Repeat-pass interferometry with airborne synthetic aperture radar, *IEEE Transactions on Geoscience and Remote Sensing*, *31*, 180-191, 1993.
- Joughin, J., Estimation of ice-sheet topography and motion using interferometric synthetic aperture radar, *Ph. D. thesis*, pp182. University of Washington, 1995.
- Joughin, I. R., D. P. Winebrenner, and M. A. Fahnestock, Observation of complex ice-sheet motion in Greenland using satellite radar interferometry. *Geophys. Res. Letts*, *22*, 571-574, 1995.
- Kwok, R., and M. A. Fahnestock, Ice sheet motion and topography from radar interferometry, *IEEE Transactions on Geoscience and Remote Sensing*, *34*, 189-200, 1996.
- Li, F. K., and R. M. Goldstein, Studies of Multibaseline Spaceborne Interferometric Synthetic Aperture Radars, *IEEE Transactions on Geoscience and Remote Sensing*, *28*, 88-96, 1990.
- Lu, Z., R. Fatland, M. Wyss, S. Li, J. Eichelberger, and K. Dean, Deformation of

- Volcanic Vents Detected by ERS-1 SAR Interferometry, Katmai National Park, Alaska. *Nature*, submitted. April 1996.
- Massonnet, D., M. Rossi, C. Carmona, F. Adragna, G. Peltzer, K. Feigl, and T. Rabaute, The displacement field of the Landers earthquake mapped by radar interferometry, *Nature*, *364*, 138-142, 1993.
- Massonnet, D., K. Feigl, M. Rossi, C. Carmona, F. Adragna, Radar interferometry mapping of deformation in the year after the Landers earthquake, *Nature*, *369*, 227-229, 1994.
- Massonnet, D., P. Briole, and A. Arnaud, Deflation of Mount Etna monitored by spaceborne radar interferometry, *Nature*, *375*, 567-570, 1995.
- Massonnet, D., and K. L. Feigl, Satellite radar interferometric map of the coseismic deformation field of the M=6.1 Eureka Valley, California earthquake of May 17, 1993, *Geophys. Res. Letts.*, *22*, 1541-1544, 1995.
- Murakami, M., S. Fujiwara, M. Nemoto, T. Saito, P. Rosen, M. Tobita, and C. Werner, Application of the interferometric JERS-1 SAR, for detection of crustal deformations in the Izu Peninsula, Japan, *EOS, Trans. Am. Geophys. Union*, *76*, F63, 1995.
- Murakami, M., M. Tobita, S. Fujiwara, T. Saito, and H. Massaharu, Coseismic crustal deformations of 1994 Northridge California earthquake detected by interferometric JERS-1 SAR, *J. Geophys. Res.*, submitted, 1995.
- Olmsted, C. Alaska SAR Facility scientific SAR user's guide, *ASF-SD-003*, pp53. Alaska SAR Facility, 1993.
- Peltzer, G., and P. Rosen, Surface displacement of the 17 May 1993 Eureka Valley, California, earthquake observed by SAR interferometry, *Science*, *268*, 1333-1336, 1995.
- Rodriguez, E., and J. M. Martin, Theory and design of interferometric synthetic aperture radars, *Proc. IEE*, *139*, 147-159, 1992.

- Solaas, G. A., and S. N. Coulson, ERS-1 SAR interferometric baseline algorithm verification, Version 1.1, *ES-TN-DPE-OM-GS02*, ESA/ESRIN, Frascati, Italy, 1994.
- Zebker, H. A., and R. M. Goldstein, Topographic Mapping From Interferometric Synthetic Aperture Radar Observations, *J. Geophys. Res.* *91*, 4993-4999, 1986.
- Zebker, H. A., S. A. Madsen, J. M. Martin, K. B. Wheeler, T. Miller, Y. Lou, G. Alberti, S. Vetrella, and A. Cucci, The TOPASR interferometric radar topographic mapping instrument, *IEEE Transactions on Geoscience and Remote Sensing*, *30*, 933-940, 1992.
- Zebker, H. A., and J. Villasenor, Decorrelation in Interferometric Radar Echoes, *IEEE Transactions on Geoscience and Remote Sensing*, *30*, 950-959, 1992.
- Zebker, H. A., P. A. Rosen, R. M. Goldstein, A. Gabriel, and C. L. Werner, On the derivation of coseismic displacement fields using differential radar interferometry: The Landers earthquake, *J. Geophys. Res.*, *99*, 19617-19634, 1994a.
- Zebker, H. A., C. L. Werner, P. L. Rosen, and S. Hensley, Accuracy of topographic maps derived from ERS-1 interferometric radar, *IEEE Transactions on Geoscience and Remote Sensing*, *32*, 823-836, 1994b.

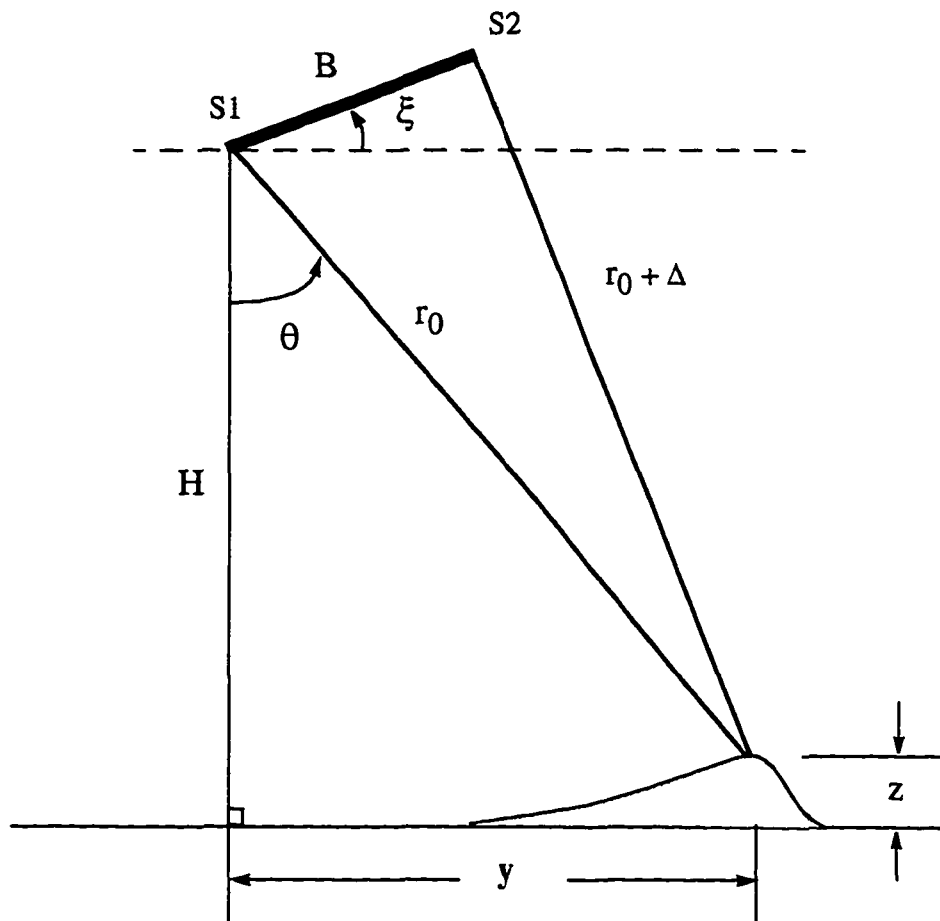


Figure 4.1 Geometry of an interferometric SAR

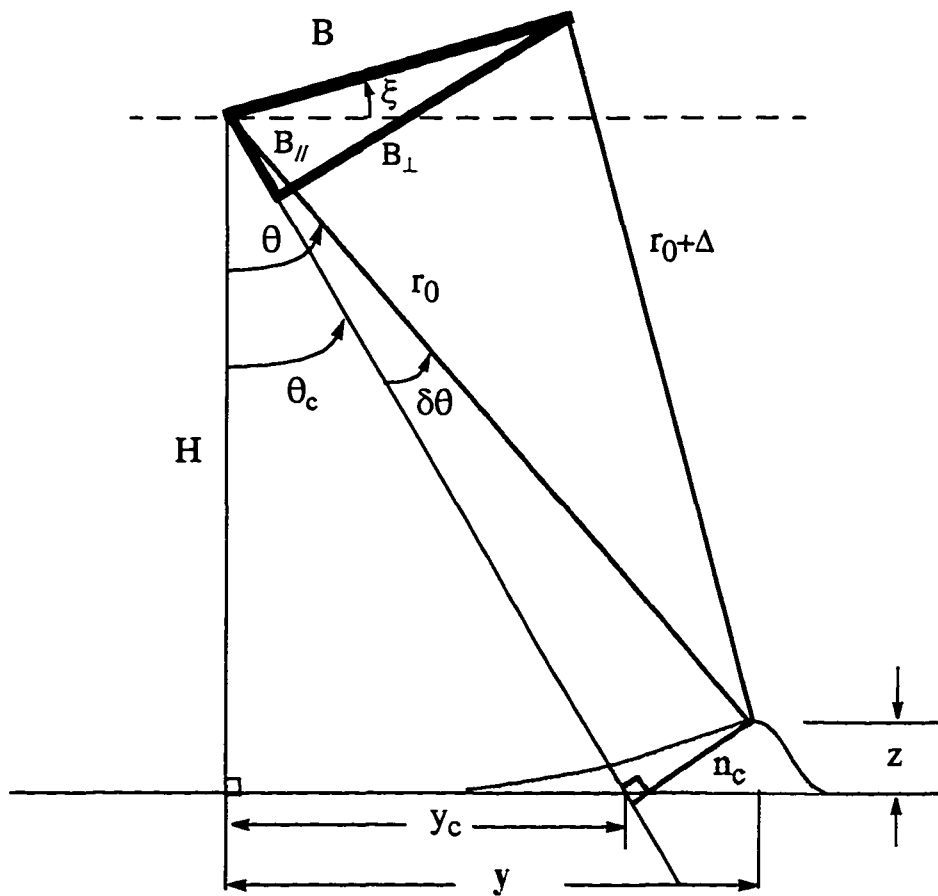


Figure 4.2 Baseline geometry of an interferometric SAR.

Chapter 5

Deformation of Volcanic Vents Detected by ERS-1 SAR Interferometry, Katmai National Park, Alaska

5.1 Abstract

Using Synthetic Aperture Radar (SAR) interferometry, we detected several centimeters of uplift that accumulated during two years (1993-1995) at two neighboring volcanoes in Alaska's Katmai National Park. The SAR interferometry technique has been used to map displacements caused by earthquakes [*Massonnet et al.*, 1993, 1994; *Zebker et al.*, 1994a; *Peltzer and Rosen*, 1995; *Murakami et al.*, 1995], and volcanic deflation associated with the eruption of Etna volcano [*Mas-*

sonnet et al., 1995] . Here, we report for the first time on a successful attempt to use this technique to monitor long-term uplift at two active volcanoes: New Trident and Novarupta Dome. From the uplift gradient we estimate the depth of the pressure source, presumably a magma body or hydrothermal system, under New Trident volcano to be 2 km. If we are able to continue monitoring the Katmai volcanic group using ERS-1 satellite radar interferometry, we may be able to assess the likelihood of future eruptions of New Trident and Novarupta Dome from the deformation rate.

5.2 Introduction

Volcanic eruptions are among the most spectacular and dangerous of natural disasters. There are 80 Quaternary volcanoes in Alaska, of which at least 44 have erupted one or more times since 1741 [*Kienle and Nye*, 1990]. On average, there is approximately one large explosive eruption every year [*Nye, personal communication*, 1995]. Two-thirds of Alaskans live near active volcanoes [*Peterson*, 1986]. Volcanic eruptions inject large volumes of volcanic ash combined with corrosive gases into the upper troposphere and lower stratosphere, the normal cruising altitude for jet aircraft. Approximately 10,000 people fly over Alaska's volcanoes every day and there are about 50,000 flights each year [*Nye, personal communication*, 1995]. Anchorage, the major hub for north Pacific air traffic and one of the largest freight airports in the United States, is home to three major airports located within 200 km of Spurr and Redoubt volcanoes, and within 450 km of Augustine and Novarupta (Katmai) volcanoes. The December 1989 to April 1990 eruption of Redoubt volcano in Alaska widely affected commercial and military airplane operations near Anchorage, and significantly affected Alaska's economy. Five commercial jetliners were damaged and repair costs exceeded \$80 million [*Steen-*

blik, 1990]. There were curtailments or cancellations of flights by international air carriers, costing approximately \$2.6 million [Steenblik, 1990]. The volcanic ash from the 1992 eruption of Spurr volcano in Alaska caused three Anchorage airports to be closed for several days, which cost approximately \$0.5 million [Casadevall, 1993]. Eruptions of volcanoes in Alaska have threatened, and will continue to threaten human life, air transportation and the economy of Alaska.

Systematic surveillance and monitoring often enable eruptions to be forecast or predicted [e.g. Fournier d'Albe, 1979; Swanson *et al.*, 1985]. Most volcanic eruptions are preceded by pronounced ground deformation in response to increasing pressure from magma chambers, or by the upward intrusion of magma. Some volcanoes also experience subsidence after eruptions, which is assumed to be due to collapse of the magma reservoir [e.g. Swanson *et al.*, 1981; Linde *et al.*, 1993]. Most well-documented eruption case studies show that ground surface deformation prior to the eruption is pronounced and generally increases in both rate and magnitude prior to the eruption [Newhall and Dzurisin, 1988]. Documented surface displacements commonly range from tens of centimeters to several meters, and the associated strains may range from tens to several hundred ppm (part per million) [e.g. Johnsen *et al.*, 1980; Savage and Clark, 1980; Tryggvason, 1980; Lipman *et al.*, 1981; Berrino *et al.*, 1984; Bianchi *et al.*, 1987; Ida, 1988; Newhall and Dzurisin, 1988; Savage, 1988; McKee *et al.*, 1989.]

In the past, volcanic ground deformation has been measured by direct measurement (tape measure!), tiltmeters, spirit leveling, and other geodetic techniques, such as Electronic Distance Measurements (EDM). Recently, measurement using the Global Positioning System (GPS) have begun to provide important constraints on volcanic deformation [e.g. Sigmundsson *et al.*, 1992; Owen *et al.*, 1995]. However, all of these measurement techniques provide information only at discrete points where the measurements are made. All require specific field measurements

to be made prior to activity on the volcano. Finally, all place equipment, or (far worse) people at risk when a volcano is very close to eruption. SAR interferometry suffers from none of the above mentioned drawbacks. Surface displacements are measured over a broad swath wherever phase coherence can be maintained. No field measurements are required, and no personnel are placed at risk.

Due to the remote locations, difficult logistics and high cost, field measurements have not been possible for most of Alaska's volcanoes. However, by INSAR such measurements will become possible for at least part of the year. We have a huge archive of satellite image data at the Alaska SAR Facility (ASF), so we can measure past as well as future deformation.

SAR interferometry measures the phase difference between two satellite passes resulting from the difference in the round-trip path length of radar waves to the same ground point. The resulting interferogram is a contour map of the change in distance to the ground surface along the look direction of the satellite. Each fringe (band of three-color, red-green-blue, or band of six-color, red-yellow-green-cyan-blue-purple) in the accompanying interferograms corresponds to a change in range distance from the satellite to the ground surface equal to one-half of the radar wavelength (28.3 mm for ERS-1).

An interferogram is characterized by the physical separation of two consistent satellite passes in space, i.e. the baseline separation, and by the time interval spanned by the two passes. The interferometric phase (fringe pattern in an interferogram) is controlled by: a) topography, b) ground-surface deformation, and c) noise from SAR system, atmospheric effects, and environmental changes such as those caused by vegetation, moisture condition, etc. The topographic component in an interferogram scales with the spatial baseline separation, while the component of ground surface movement is independent of the baseline. If the ground surface is unchanged during two ERS-1 satellite passes, the interferogram can be

used to produce high resolution Digital Elevation Models (DEM) [e.g. *Zebker et al.*, 1994b, *Mrstik et al.*, 1996]. When the spatial baseline approaches zero, the fringes in an interferogram are completely controlled by ground movement and contain no information dependent on the topography. This is the ideal case to measure surface deformation. In the case where the baseline length is not zero, the component of the phase signal contributed by ground movement can be obtained by removing the topographic component of the fringe in an interferogram. Two methods are used to achieve this goal. One is to use an existing DEM to synthesize an interferogram and remove the topographic effect from the observed interferogram [e.g. *Massonnet et al.*, 1993, 1994, 1995]. The other method makes use of three satellite passes; a pair of images is used to construct a DEM, and this DEM is used to remove the topographic effect in the second pair [e.g. *Zebker et al.*, 1994a; *Peltzer and Rosen*, 1995].

The advantages of satellite interferometry over the commonly used geodetic measurements are: a) Radar interferometry measures spatially-distributed ground surface deformation with a level of detail and resolution not attainable by GPS or EDM. Integrating the displacement field of a volcano derived from satellite interferometry with information derived from GPS or EDM will result in a significant step forward in understanding of the detailed physical processes of magma intrusions. b) Since the satellite orbits at regular intervals, the base line data have already been collected. Satellite radar interferometry can capture ground surface change from a volcano without advance knowledge of the state of the volcano. c) No personnel or equipment are placed at risk in the collection of SAR measurements.

5.3 Analysis

Figure 5.1 shows an interferogram constructed for the Katmai area covering Novarupta and the Valley of Ten Thousand Smokes from images obtained in passes three days apart. The broad fringes occur in the Valley of Ten Thousand Smokes. If the phases in Figure 5.1 are attributed to the effect of topography, a digital topography map can be produced based on the interferogram. Figure 5.2 is topographic map constructed from the interferogram (Figure 5.1) which clearly shows the Valley of Ten Thousand Smokes and the dome of Novarupta associated with the volcanic centers. Noise analysis implies that the height resolution of our technique is approximately 10 meters.

In order to measure the long-term deformation of volcanoes, we must be able to maintain phase coherence over several years. Phase coherence depends on baseline separation, time interval between the two satellite passes, environmental changes, and thermal noise in the measurement system. All these factors reduce the coherence of the constructed interferogram. *Zebker and Villasenor* [1992] showed coherence will get worse if the baseline separation gets larger and/or the time interval gets longer.

Obtaining phase coherence is a great challenge for constructing interferograms for Alaska's volcanoes, which are covered seasonally or permanently by snow and ice. Nevertheless, the logistical difficulties of surface-based measurements make application of satellite-based monitoring techniques such as SAR interferometry highly desirable. We chose the Katmai volcanic group of the Alaska Peninsula as the site for our investigation because it has produced major eruptions in recent time and has relatively subdued topography. Indeed, some 100 km² of the region was "paved" with ignimbrite in 1912 to form the Valley of Ten Thousand Smokes (VTTS) in the greatest eruption on Earth this century, and remains unvegetated

today [*Hildreth, 1983*] (Figure 5.3). The vent is marked by Novarupta Dome (N) and a 2-km-diameter basin containing arcuate fractures and hot spots. The surface of the ignimbrite ranges from ash-sized particles at its distal end to pumice clasts up to tens of centimeters near Novarupta. Five kilometers to the southeast is the New Trident vent, located on the southwest flank of Trident volcano. This lava complex formed during a series of eruptions that lasted from 1953 to 1968 (Figure 5.3) [*Snyder, 1954; Ray, 1967*]. Both Novarupta Dome and New Trident lavas have rugged surfaces comprised of 1-3 m blocks.

Our analysis of ERS-1 SAR interferometry at Katmai leads to the following conclusions on coherence: 1) For all areas, coherence will be lost for images acquired between October and June because of environmental changes such as snow cover and melting; 2) For VTTS, coherence may be maintained over the three-month period from the middle of June to the end of September; 3) For the young lava flows of New Trident volcano and Novarupta Dome, coherence is maintained for at least two years using summer images. Therefore, we analyzed the images acquired by ERS-1 during the summers of 1993 and 1995 and thus minimized or eliminated environmental change factors.

Figure 5.4 (a and b) shows interferograms that span the period between the summers of 1993 and 1995. The baseline separation of two satellite passes is 1 m. One fringe in the interferogram at New Trident vent (Figure 5.4a) represents a ground-surface deformation of 28.3 mm along the radar's look direction if we attribute the fringe pattern completely to ground movement. There are at least two fringes along the line from A to B (distance 650 m), most likely three fringes from A to the yellow dot (New Trident vent). The fringes can not be attributed to topography because the relief from A to B is less than 500 m, corresponding to at most 1/20 of one fringe. The order of color banding is green-blue-red from A to B, which implies increasing phase and corresponds to upward movement of B

relative to A, or inflation. The fringe pattern is quite clear on the west flank of the volcano, whereas it is disturbed on the east flank for unknown reason.

We conclude that 60 to 80 mm inflation took place along the look direction of the satellite around the vent of New Trident between 1993 and 1995. Taking into account the radar's 23° incidence angle, the vertical ground deformation could amount to 65 to 87 mm over two years. The inflated region covers about 7 km^2 . Due to the loss of coherence (shaded area in Figures 5.4a and 5.4b), we may have underestimated the amount and the area of inflation. The boundary between the region of coherence and loss of coherence corresponds to the change in surface from rough young lava to loose ash.

We interpret this inflation as created by shallow intrusion of magma and/or pressurization of the hydrothermal system under the vent. Assuming a simple model of pressure change in a sphere located in an elastic half-space [*Mogi, 1958*], we estimated the depth of a magma body to be approximately 2 km, based on the uplift gradient. This corresponds approximately to a volume of intense microseismicity [*Jolly, A., pers. comm.*].

Figure 5.4b shows an interferogram of Novarupta Dome, indicated by N, and the surrounding region. Here, one fringe pattern is represented by a six-color-band. Most of the regions lose coherence over the two years between images. However in a 9 km^2 area east of Novarupta Dome (outlined by dashed line in black) we see a bull's-eye pattern, which may indicate ground deformation. The topographic relief in this area could contribute a $1/30$ part of a fringe at most. We count $2/3$ of a fringe in this area, corresponding to about 20 mm uplift of the volcanic surface, centered approximated 2 km east of Novarupta Dome (Figure 5.4b). In this case, the boundary between coherence and loss of coherence does not correspond to dramatic changes in surface texture.

The fringes located in the dashed white outline indicate an uplift from C to D

of about 30 mm along the radar look direction (Figure 5.4b). This corresponds to 33 mm inflation if the deformation is assumed to have been vertical. Due to loss of coherence on the steep rubbly slope west of this uplifted region, we could only see part of the bull's-eye fringe pattern. The inflation could be due to expansion of a shallow magma body or hydrothermal system. Alternatively, the inflation could be due to movement along a vent-bounding fault, because this fringe is located near arcuate grabens created during 1912's eruption of Novarupta Dome.

To evaluate whether the fringe patterns in Figures 5.4a and 5.4b are caused by deformation rather than by atmospheric effects or environmental changes, we analyzed three other images. Two were acquired during the summer of 1995 with 35 days separation, and one was acquired in the summer of 1993. We constructed two interferograms, one for a 35-day and another for a two-year interval. We use the 35-day interferogram as a DEM to remove the topographic effect in the two-year interferogram. Figure 5.5 shows the interferogram generated from this data set including the topographic correction. We find approximately the same fringe patterns as those observed in Figure 5.4a and 5.4b. Because Figure 5.5 is produced using three images, the noise level is higher than that in Figure 5.4. Errors introduced by atmospheric effects are generally less than half a fringe for an approximate 2000 km² area [Massonnet *et al.*, 1995], which is much larger than our uplifted areas. Also, it is unlikely that atmospheric conditions remained the same when the two sets of data were gathered. We therefore conclude that the fringe patterns most likely reflect ground deformation. We do not attribute the ground deformation to earthquakes, because no earthquakes large enough to produce such deformation have been located in the region.

The accuracy of the measurement by interferometry technique is also limited by the error in estimating the baseline separation of the two satellite passes. The baseline separations are calculated based on the position and velocity vectors of

satellites. We further refine the baseline separation as follows: we change the baseline by 0.5 m at each step, produce an interferogram for each baseline separation, and then select the interferogram with no striped fringe pattern (the striped fringes are caused by errors in the baseline separation estimate). This procedure is time-consuming, but it provides an accurate estimate of the baseline within ± 1 m.

The shaded regions in Figures 5.4 and 5.5 are areas of coherence loss. Lost coherence is represented by random colors in the interferograms. We differentiate areas with adequate phase signals from noisy areas by evaluating phase coherence everywhere in the range image. The correlation coefficient ranges from 1 for best coherence to 0 for complete loss of coherence. Figure 5.6 shows histograms for a representative area of low coherence ('noise' - Figure 5.6a) and for a representative area of high coherence ('useful signal' - Figure 5.6b) at the inflated region of New Trident vent. The mean correlation coefficient is 0.32 ± 0.16 and 0.64 ± 0.20 for the region of lost coherence and New Trident vent, respectively. Based on the correlation coefficients in Figure 5.6a, we estimate the standard deviation of the interferometric phase to be about 40° . This corresponds to 3 mm resolution on detecting ground deformation.

At New Trident during 1993 and 1995, the inflation rate was about $30 \sim 40$ mm/year and the strain rate was $20 \sim 30$ ppm/year. This rate is twice the long-term inflation rate at Sakurajima volcano, Japan ($10 \sim 15$ mm/year) [Organizing Committee, 1988] before the 1915 and 1946 eruptions. The inflation rate is also higher than those at Yellowstone caldera (1 ppm/year) [Dzurisin and Yamahita, 1987], Long Valley caldera ($1 \sim 25$ ppm/year) [Hill et al. [1991], and Campi Flegrei caldera, Italy (20 ppm/year) [Berrina et al., 1984]. The inflation rate at New Trident vent is comparable with that observed at Kilauea volcano, about $20 \sim 50$ ppm/year before eruptions [Decker, 1981].

A geodetic network (white dots in Figure 5.4b) was established in 1989 to

monitor ground deformation in the area of Novarupta Dome [*Kleinman and Iwatsubo, 1991*]. The Novarupta geodetic network was re-surveyed in 1990, 1993, and 1995. During 1990-1993, the lengths of all ten measured lines (by Electronic Distance Measurement (EDM)) increased by an average of 22.5 millimeters, which is two-to-three times the expected error for lines of this length [*Kleinman et al., 1996*]. During 1993-1995, the Main Street (Ma) benchmark [Figure 5.4b] may have moved northwest about 2 cm based on GPS measurement [*Kleinman et al., 1996*]. However, because the benchmarks are located outside the inflated area, the GPS measurement could not help us further pin down the inflation around the region of Novarupta Dome.

The seismological evidence suggested the existence of shallow fluid body under the study area. Analysis of seismic signals showed that travel time delays of up to 0.9 sec existed at a station near New Trident vent between September 1987 and December 1990 [*Ward et al., 1991*]. These authors explained the anomaly by the presence of a large, low-velocity magma body or plexus of magma bodies around the New Trident volcano. The hypocenters of earthquakes ranged from 2 to 6 km depth.

Gravity studies also suggest the existence of a shallow fluid body under the study area. Gravity measurements completed in July 1990 [*Saltus et al., 1991*] showed a large bowl-shaped Bouguer gravity anomaly of -42 mgal centered at a point 3 km west of New Trident vent. The anomaly spans about 400 km². These authors developed a model of an anomalous body centered at 6 km with a top that could be as shallow as 2 km, which is consistent with earlier gravity observations [*Kienle, 1970*].

5.4 Conclusion

We suggest that our observations of 70 to 90 mm uplift at New Trident vent and 20 to 30 mm deformation at Novarupta Dome reflect expansion of shallow magma cupolas. Based on our observations and previous supporting work, we envision a large magma body under the study area with several localized areas of expansion. The observed uplift rates of a few centimeters per year indicate the Katmai volcanic group, the site of the largest volcanic eruption of this century, is still very much alive.

5.5 References

- Berrino, G., G. Corrado, G. Luongo, and B. Toro, Ground deformation and gravity changes accompanying the 1982 Pozzuoli uplift, *Bull. Volcanol.*, *47*, 187-200, 1984.
- Bianchi, R., A. Coradini, C. Federico, G. Giberti, P. Lanciano, J. P. Pozzi, G. Sartoris, and R. Scandone, Modeling of surface deformation in volcanic area: the 1970-1972 and 1982-1984 crises of Campi Flegrei, Italy, *J. Geophys. Res.*, *92*, 14139-14150, 1987.
- Casadevall, T. J., Volcanic ash and airports, *U. S. Geol. Surv. Open File Rep.*, *93-518*, 1993.
- Davies, P. M., Surface deformation due to inflation of an arbitrarily oriented triaxial ellipsoidal cavity in an elastic half-space, with reference to Kilauea volcano, Hawaii, *J. Geophys. Res.*, *91*, 7429-7438, 1986.
- Decker, R. W., Dynamics of Hawaiian volcanoes: an overview, *U. S. Geol. Surv. Prof. Paper 1350*, 997-1018, 1981.
- Dzurisin, D., and K. M. Yamashita, Vertical displacements at Yellowstone caldera, Wyoming, 1976-1986, *J. Geophys. Res.*, *92*, 13753-13766, 1987.
- Fournier d'Albe, E. M., Objectives of volcanic monitoring and prediction, *J. Geol. Soc. London*, *136*, 321-326, 1979.
- Goldstein, R. M., H. Engelhardt, B. Kamb, and R. M. Frolich, Satellite Radar Interferometry for Monitoring Ice Sheet Motion: Application to an Antarctic Ice Stream, *Science*, *262*, 1525-1530, 1993.
- Hildreth, W., The compositionally zoned eruption of 1912 in the Valley of Ten Thousand Smokes, Katmai National Park, Alaska, *J. Volcanol. Geotherm. Res.*, *18*, 1-56, 1983.
- Hill, D. P. and others, Response plans for volcanic hazards in the Long Valley

- caldera and Mono craters area, California. *U.S. Open file Report 91-270*, 1991.
- Ida, Y., Crustal deformation. in Aramaki, S. (ed.), The 1986-1987 eruption of Izu-Oshima volcano, Earthquake Res. Inst. Univ. of Tokyo, 62p. 1988.
- Johnsen, G. V., A. Bjorensen, and S. Sigurdsson, Gravity and elevation changes caused by magma movement beneath the Krafla caldera, northeast Iceland. *J. Geophys.*, 47, 132-140.
- Kienle, J.. Gravity traverses in the Valley of Ten Thousand Smokes. Katmai National Monument, Alaska, *J. Geophys. Res.*, 75, 6641-6649, 1970.
- Kienle J., and C. J. Nye, Volcano tectonics of Alaska, in C. A. Wood and J. Kienle (eds.), *Volcanoes of North America, United States and Canada*, Cambridge Univ. Press, 1990.
- Kleinman, J. and E. Iwatsubo. A geodetic network in the Novarupta area, Katmai National Park, Alaska, *Geophys. Res. Letts.*, 28, 1517-1519, 1991.
- Kleinman, J., E. Iwatsubo, J. Power, and E. Endo. Geodetic studies in the Novarupta area, Katmai National Park, Alaska, 1990 - 1995. submitted to *US Geol. Surv. Open File Report*, 1996.
- Linde, A. T., K. Agustsson, I. S. Sacks, and R. Stefansson, Mechanism of the 1991 eruption of Hekla from continuous borehole strain monitoring, *Nature*, 365, 737-740, 1993.
- Lipman, P. W., J. G. Moore, and D. A. Swanson. Bulging of the north flank before the May 18 eruption - geodetic data, in Lippman, P. W. and D. R. Mullineaux (eds.), The 1980 eruptions of Mount St. Helens, Washington. *U. S. Geol. Surv. Prof. Paper 1250*, 143-154, 1981.
- Massonnet, D., M. Rossi, C. Carmona, F. Adragna, G. Peltzer, K. Feigi, and T. Rabaute, The displacement field of the Landers earthquake mapped by radar interferometry, *Nature*, 364, 138- 142, 1993.
- Massonnet, D., K. Feigi, M. Rossi, C. Carmona, and F. Adragna. Radar interfer-

- ometry mapping of deformation in the year after the landers earthquake. *Nature*, 369, 227-229, 1994.
- Massonnet, D., P. Briole, and A. Arnaud. Deflation of Mount Etna monitored by spaceborne radar interferometry, *Nature*, 375, 567-570, 1995.
- McKee, C., J. Mori, and B. Talai. Microgravity changes and ground deformation at Rabaul caldera, 1973-1985, in Latter, J. H. (ed), *Volcanic Hazards*. Springer-Verlag, Berlin, New York, 399-428, 1989.
- Mogi, K., Relations between the eruptions of various volcanoes and the deformations of the ground surface around them, *Bull. Earthquake Res. Inst. Univ. Tokyo*, 36, 99-134, 1958.
- Mrstik, V., G. VanBlaricum, G. Cardillo, and M. Fennell. Terrain height measurement accuracy of interferometric synthetic aperture radars, *IEEE Transactions on Geoscience and Remote Sensing*, 34, 219-228, 1996.
- Murakami, M., M. Tobita, S. Fujiwara, T. Saito, H. Massaharu. Coseismic crustal deformations of the 1994 Northridge California earthquake detected by interferometric JERS-1 SAR, submitted to *J. Geophys. Res.*, 100, 1995.
- Newhall, S. G., D. Malone, and C. S. Weaver. Forecasts and predictions of eruptive activity at Mount St. Helens, USA: 1975-1984, *J. Geodynamics*, 3, 397-423, 1985.
- Newhall, C. G., and D. Dzurisin, Historical unrest at large calderas of the world. *U. S. Geol. Surv. Bull.*, 1855, 1108, 1988.
- Organizing Committee on Kagoshima International conference on Volcanoes. *A guide book for Sakurajima volcano*. Japan, 1988.
- Owen, S., P. Segall, J. Freymueller, A. Miklius, R. Denlinger, T. Arnadottir, M. Sako, and R. Burgmann, Rapid deformation of the south flank of Kilauea volcano, Hawaii. *Science*, 267, 1328-1332, 1994.
- Peltzer, G., and P. Rosen, Surface displacement of the 17 May 1993 Eureka Valley, California, earthquake observed by SAR interferometry, *Science*, 268, 1333-1336.

- 1995.
- Peterson, D. W., Volcanoes: tectonic setting and impact on society. *Studies in Geophysics*, National Academy Press, 1986.
- Ray, D., Geochemistry and petrology of the Mt. Trident andesites, Katmai National Monument, Alaska, *Ph. Thesis*. University of Alaska Fairbanks, 1967.
- Saltus, R. W., D. Stone, J. Kienle, and A. M. Goodliffe, New gravity data at Katmai National Park, Alaska, suggest a magma body analogous to that at the Geysers-Clear Lake Region, California, *EOS Trans. Am. Geophys. Un.*, 72, 429, 1991.
- Savage, J. C. and N. M. Clark, Magmatic resurgence in Long Valley caldera, California: possible cause of the 1980 Mammoth Lakes earthquakes, *Science*, 217, 531- 533, 1980.
- Savage, J. C., Principal component analysis of geodetically measured deformation in Long Valley caldera, eastern California, 1983-1987, *J. Geophys. Res.*, 93, 13297- 13305, 1988.
- Sigmudsson, F., P. Einarsson, and R. Bilham, Magma chamber deflation recorded by the Global Positioning System: the Hekla 1991 eruption, *Geophys. Res. Lett.*, 19, 1483-1486, 1992.
- Snyder, G. L., Eruption of Trident volcano, Katmai National Monument, Alaska, *U.S. Geol. Surv. Circular 318*, 7p, 1954.
- Steenblik, J. W., Volcanic ash: a rain of terra, *Air Line Pilot*, 56, 9-15, 1990.
- Swanson, D. A., P. W. Lipman, J. G. Moore, C. C. Heliker, and K. M. Yamashita, Geodetic monitoring after the May 18 eruption, in Lipman, P. W. and D. R. Mullineaux (eds.), The 1980 eruptions of Mount St. Helens, Washington, *U. S. Geol. Surv. Prof. Paper 1250*, 143-154, 1981.
- Tryggvason, E., Subsidence events in Krafla area, north Iceland, 1975-1979, *J. Geophys.*, 47, 141-153, 1980.

- Ward, P., A. M. Pitt, and E. Endo. Seismic evidence for magma in the vicinity of Mt. Katmai, Alaska. *Geophys. Res. Letts.*, 18, 1537-1540. 1991.
- Zebker, H. A., and J. Villasenor. Decorrelation in Interferometric Radar Echoes. *IEEE Transactions on Geoscience and Remote Sensing*, 30, 950-959. 1992.
- Zebker, H. A., P. A. Rosen, R. M. Goldstein, A. Gabriel, and C. L. Werner. On the derivation of coseismic displacement fields using differential radar interferometry: The Landers earthquake, *J. Geophys. Res.*, 99, 19617-19634. 1994a.
- Zebker, H. A., C. L. Werner, P. L. Rosen, and S. Hensley. Accuracy of topographic maps derived from ERS-1 interferometric radar, *IEEE Transactions on Geoscience and Remote Sensing*, 32, 823-836. 1994b.

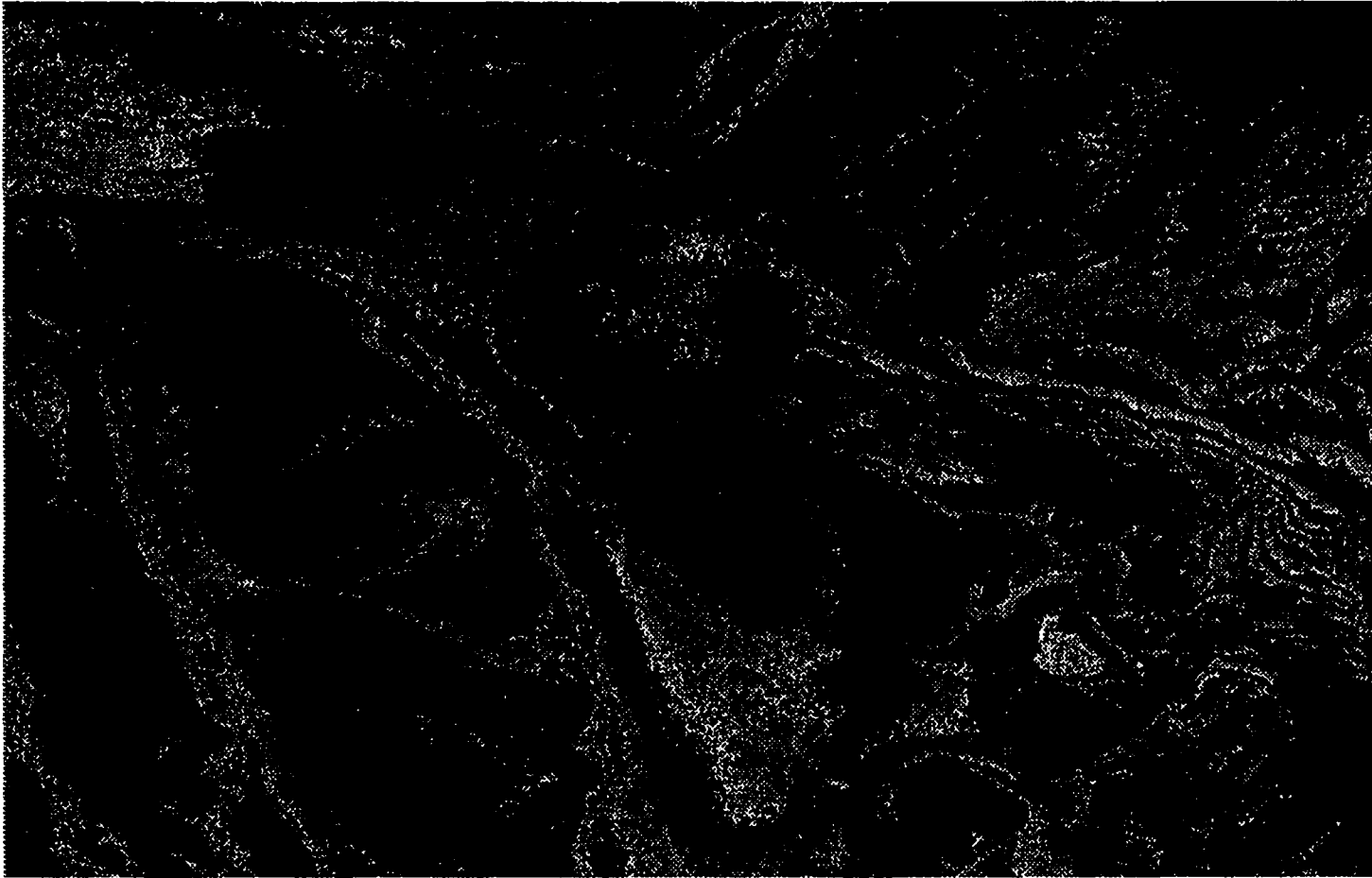


Figure 5.1 Interferogram using ERS-SAR data for an area with dimensions of 17 X 14 km covering Novarupta Dome, the site of this century's largest eruption on Earth. The image pair used to generate the interferogram was acquired in September 1991, and the orbit passes were separated by 3 days. The color code (red-yellow-green-blue-violet-magenta) covers an elevation interval of 21.7 meters. The image is not correlated in black areas. However, reliable elevation differences between points can be obtained by integration along paths that avoid black areas.

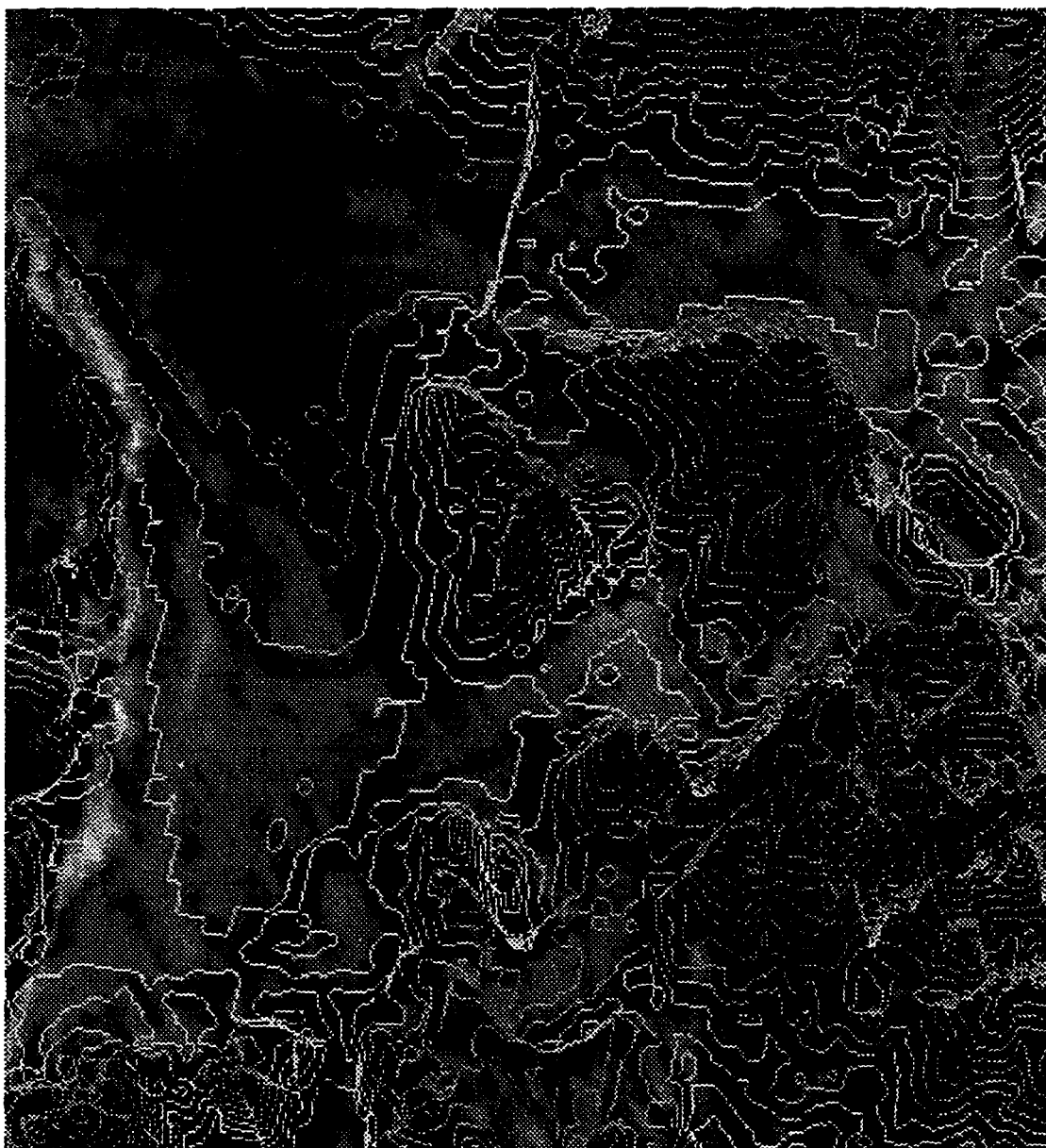


Figure 5.2 Topographic map of the area around Novarupta Dome (12 X 12 km) derived from an interferogram as shown in Figure 5.1. The contour interval is 18 meters. Geographic north is downward in the figure. The band of relatively flat area in the lower center is the Valley of Ten Thousand Smokes. Novarupta is located about 4 km toward the 10 o'clock position from the center of the figure.

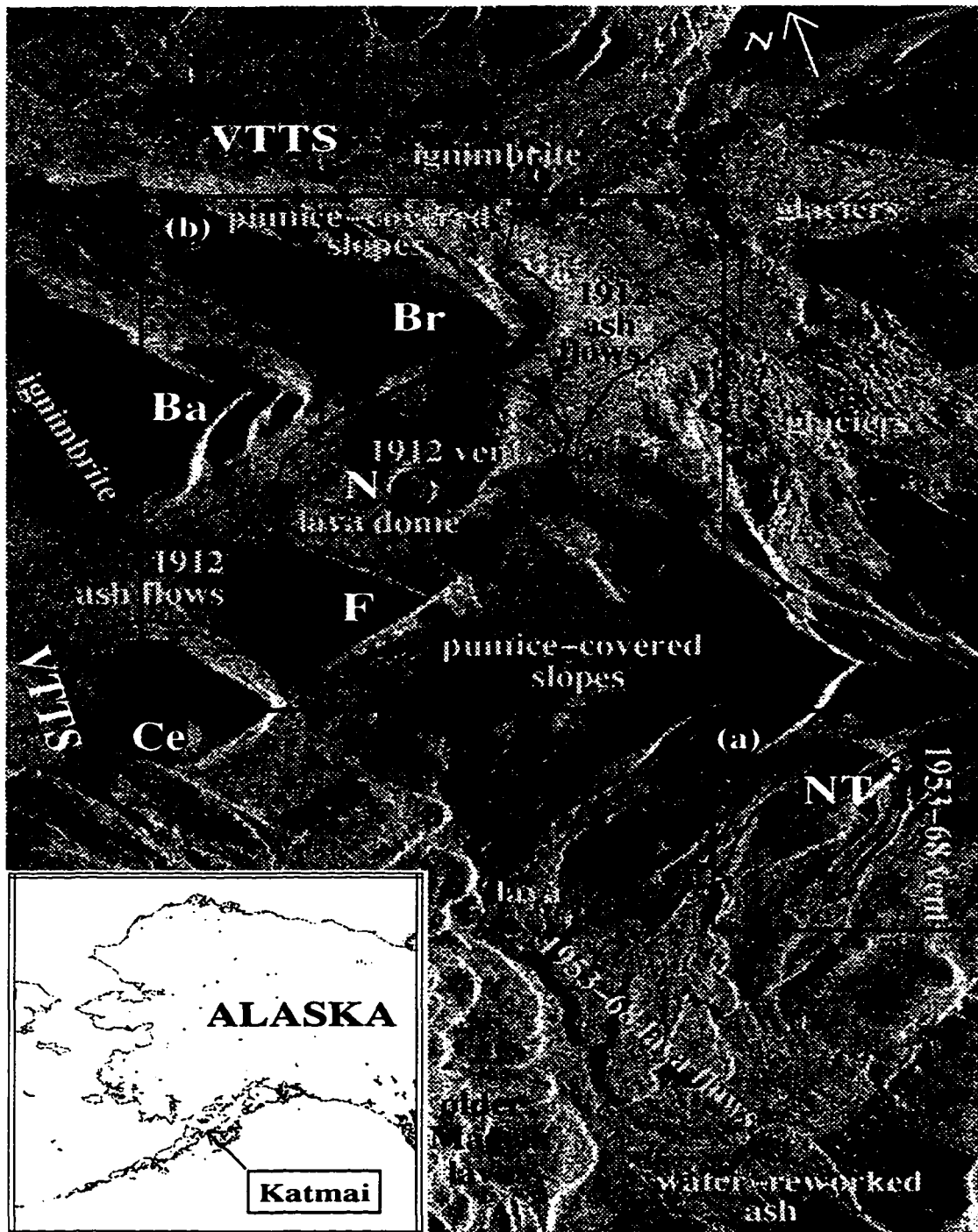


Figure 5.3 ERS-1 radar image of Katmai group and surrounding region. The location of the Katmai region with respect to Alaska is shown at the lower left corner. The two small boxes a) and b) denote the areas covered by Figures 5.4a/5.5a and 5.4b/5.5b, respectively. [Key: NT, New Trident vent; VTTS, Valley of Ten Thousand Smokes; Ba, Baked Mountain; Br, Broken Mountain; Ce, Mount Cerberus; F, Falling Mountain; N, Novarupta Dome.]

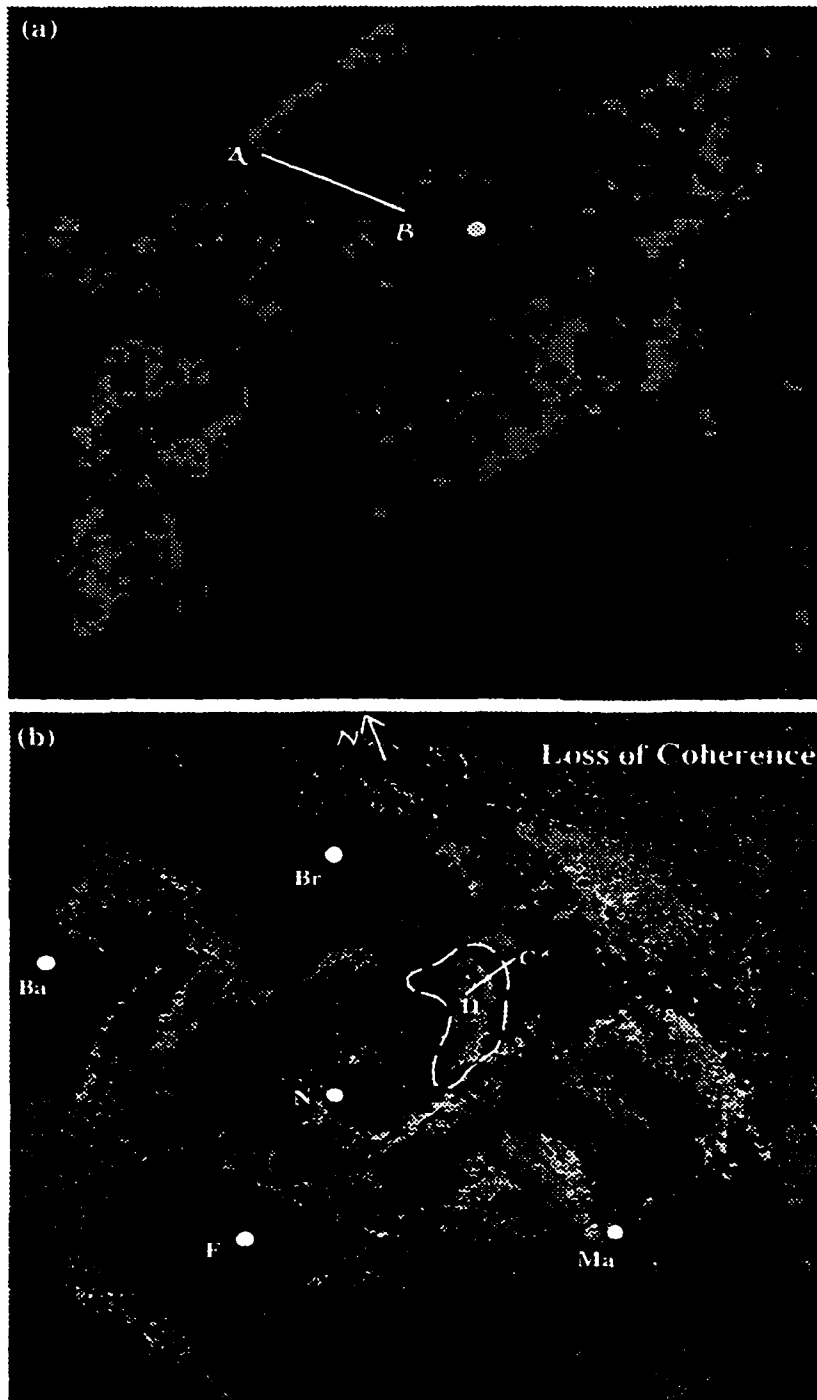


Figure 5.4 Interferograms at New Trident vent (a), and the area of Novarupta Dome (b). One fringe (a) is represented by three colors. The fringe (b) is represented by six colors. The interferograms were constructed using a pair of ERS-1 images recorded in the summers of 1993 and 1995 with baseline separation of 1 m. Dimensions of Figures a and b are 3.5 km X 3.5 km, and 8 km X 8 km, respectively. The yellow dot in a is the location of the vent of New Trident volcano. White dots in b are the benchmarks of the geodetic network. We shaded the regions of lost coherence for clarity. [Key: Ba, Baked Mountain; Br, Broken Mountain; F, Falling Mountain; N, Novarupta Dome; Ma, Mount Main Street.]

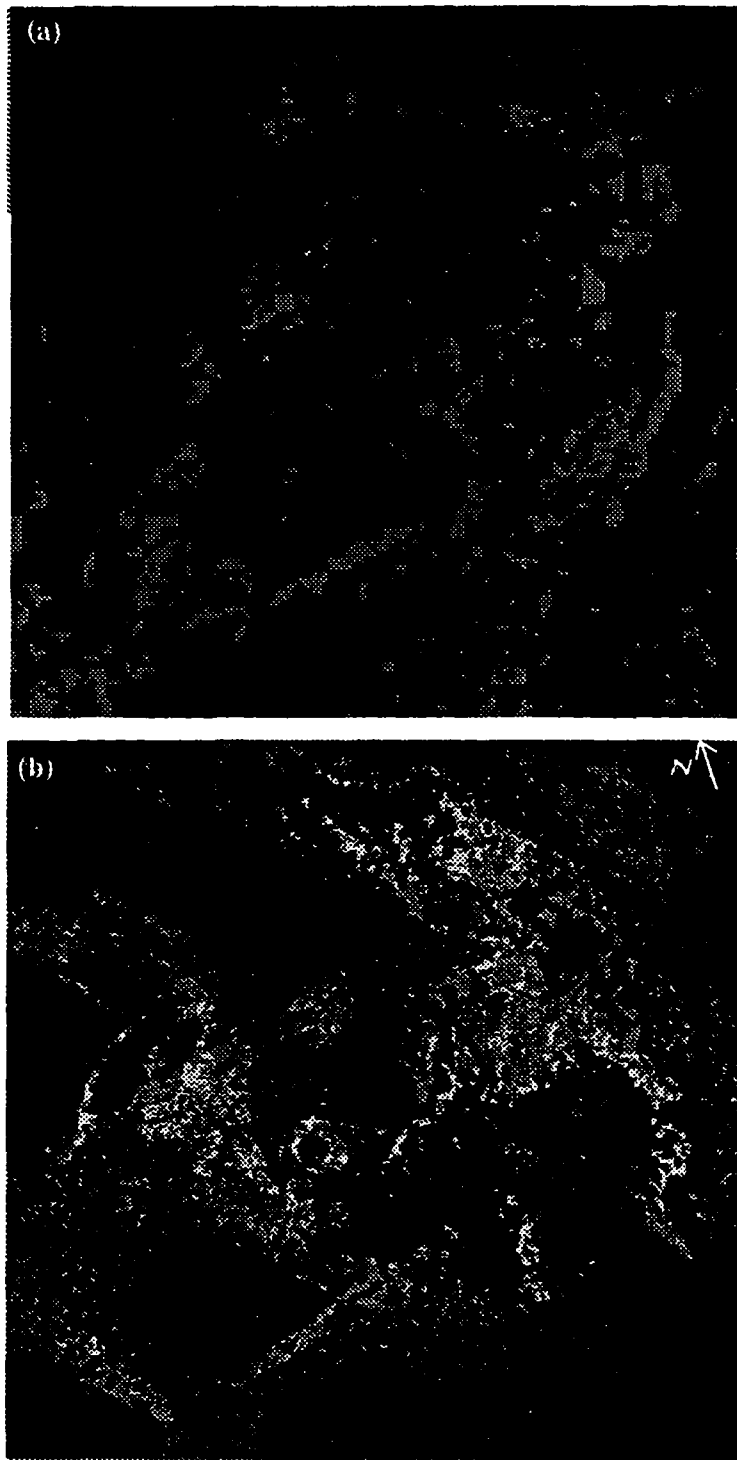


Figure 5.5 Interferograms of New Trident vent (a), and in the area of Novarupta (b). The interferograms are constructed by three ERS-1 images recorded in the summers of 1993 and 1995. The topographic component in the interferograms has been removed. The color bands and dimensions of the figures are the same as those in Figure 5.4.

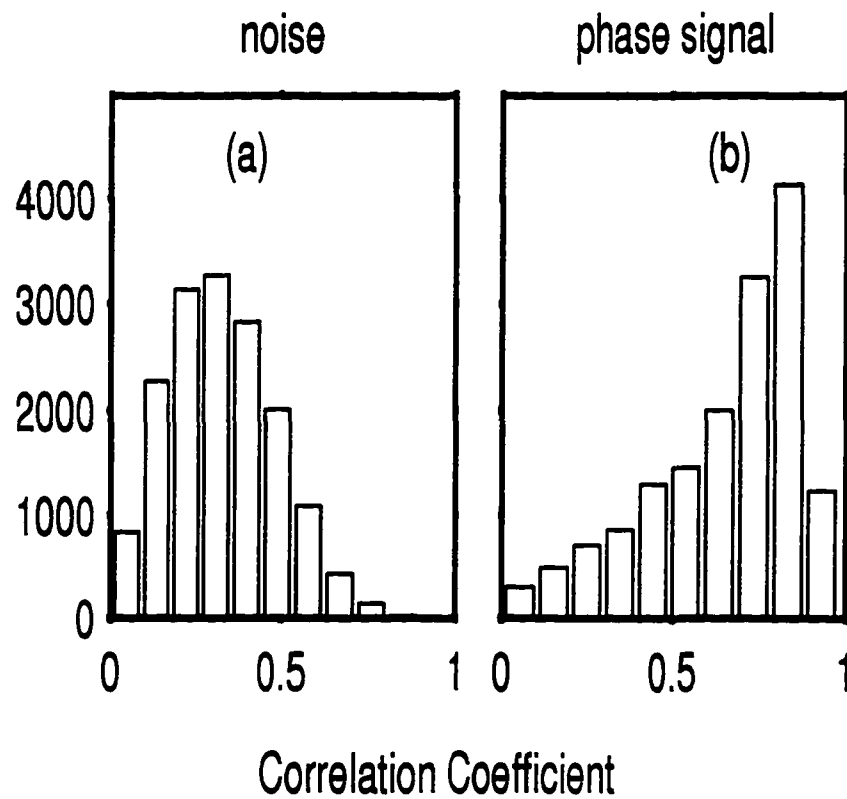


Figure 5.6 Comparison of histograms of correlation coefficients for an area with loss of coherence (a) and an area of inflated region at New Trident vent (b). The correlation coefficient ranges from 1 for best coherence to 0 for complete loss of coherence. The mean correlation coefficient is 0.32 ± 0.16 and 0.64 ± 0.20 for the region of lost coherence and New Trident vent, respectively. The regions with loss of coherence are represented by random colors in an interferogram (shaded regions in Figures 5.4 and 5.5).

Chapter 6

Conclusions

The method of plotting the cumulative misfit as a function of earthquake numbers, which are ordered in space or time, is proposed for investigating the stress homogeneity of the Aleutian arc, or for investigating the stress changes as a function of time. Using this method along the Aleutian plate boundary, we conclude that the aftershock sequences of the 1964 and 1986 events appear more homogeneous than those of the foreground and background sequences, based on the analysis of misfit as a function of time. The homogeneity condition of the aftershock sequence (sometimes also containing several preshocks) lasts approximately 1 year. The cumulative misfit as a function of earthquake number along the strike of the arc shows that the Aleutian arc (from 170°E to 145°W) can be divided into five major segments. The focal mechanism data in the stress-homogeneous segments were used to invert the principal stress orientations using the method of *Cephart* [1990].

We considered the correlation of the stress boundaries with four other tectonic features: fracture zones, submarine canyons, ends of the aftershock zones of great ruptures, and asperities. The strongest correlation seems to exist between fracture zones and stress direction changes. This may be interpreted as indicating a decoupling within the underthrusting plate along the zones of weakness (the fracture

zones) across which stress may not be transmitted fully. The correlation of morphological features, such as canyons, with stress discontinuities is weakest. This suggests that most of the canyons may not influence the process in the lower crust. Further, a fairly strong correlation of asperities and ends of ruptures with location of stress discontinuities is observed.

The method of plotting the cumulative misfit as a function of earthquake numbers, could also be used to determine the volume where the stress directions are homogeneous. Applying this method to the Alaska WBZ, we inverted for stress directions in Alaska using fault plane solutions. To satisfy the assumption of homogeneity of the stress field we subdivided the data set of the small and large earthquakes into 25 and 3 sub-sets as a function of space, respectively. In the subducting slab the stress directions measured by the large earthquakes were homogeneous, with extension down dip and greatest compression along strike. The unusual orientation of the greatest principal stress is attributed to the bend of the slab under central Alaska, which generates compressive stresses along strike. The small earthquakes, in contrast, reveal a great deal of heterogeneity as a function of depth and along strike, although they show a trend that confirms the overall inversion result from the large events. We propose that the ratio of the dimensions of the stress field (sensed by earthquakes) to the rupture dimensions is approximately 20. The estimated stress directions of the crustal earthquakes correspond to the following mechanisms: (1) strike-slip faulting with the greatest principal stress oriented NS near Fairbanks, and (2) thrusting with the greatest principal stress oriented NW near Mount McKinley.

The criteria by which we judge the usefulness of an inversion for the stress directions are (1) that the directions are reasonably well constrained, and (2) that there is evidence for homogeneity in the sample. The latter we base on the size of the average misfit which we require to be less than approximately 6° in the

method of Gephart and Forsyth [1984]. Using the smallest average misfit we can find (about 3.2° in Alaska) as a guide, we seek to find all subsets that approach this value. The cumulative misfit plot as a function of space is the method by which we search for divisions between homogeneous sub-sets. Applying this method we have been able to reduce the average misfit of inversions in subsets. The average misfits of the sub-sets we accept as satisfying the assumption of homogeneity, are smaller than the average misfit of the overall data set by factors of 2 to 3.

Using INSAR we observed 70 to 90 mm uplift at New Trident vent and 20 to 30 mm deformation at Novarupta Dome over a two-year-period. We interpret the inflation to reflect expansion of shallow magma cupolas. Based on our observations and previous supporting work, we envision a large magma body under the study area with several localized areas of expansion. The observed uplift rates of a few centimeters per year indicate the Katmai volcanic group, the site of the largest volcanic eruption of this century, is still very much alive.

Appendix A

This appendix consists of figures that we could not fit into Chapters 2 and 3 which are originally prepared for journal publication. However, these figures are helpful to understand some of the detailed analyses and explanations in Chapters 2 and 3.

Figure A.1 is a schematic plot showing our hypothesis, and the method to test our hypothesis (see Method in Chapter 2). We hypothesize that the stress directions are uniform in limited segments of the plate boundary, but different in each sub-segment. The extent of segments with homogeneous stress-directions will be determined from changes in slope of the cumulative misfit, $\Sigma f(x)$, calculated based on a reference-stress-tensor, which can be an assumed one approximately fitting the tectonic setting, or it can be the stress-tensor fitting any segment. Segments will be considered as defined, if their relatively constant slopes of $\Sigma f(x)$ are different from that of the neighboring segment above the 95% confidence level, as judged by the standard deviate z-test or t-test (Equations 2.1 and 2.2). The schematic plot of Figure A.1 illustrates that the stress-heterogeneous fault AZ can be divided into four segments where the stress is homogenous. The hypothesis we set out to test is confirmed by the results shown in Chapters 2 and 3, and the result in *Wyss and Lu [1995]*. We conclude that segments of constant slope of $\Sigma f(x)$ exist, and the slopes of neighboring segments differ strongly. Especially, the

fact that our quantitative method picks all four segment-boundaries, proposed by *Jones* [1988] based on common sense, supports our proposal that this method is capable of defining the segmentation of faults in a meaningful way [*Wyss and Lu*, 1995].

Figures A.2-A.6 show cumulative misfit as a function of distance along the strike at several depth ranges of the Alaska WBZ. Based on these plots and Figure 3.9, we divide the earthquakes in individual depth range into subsets. The stress directions in most of the sub-volumes are homogenous. For some sub-sets, such as 4b in Figure A.2 and 5b in Figure A.3, we could not find suitable divisions so that the stress directions are meaningful. We interpret this observation as caused by the rapid changes of stress directions in the volumes.

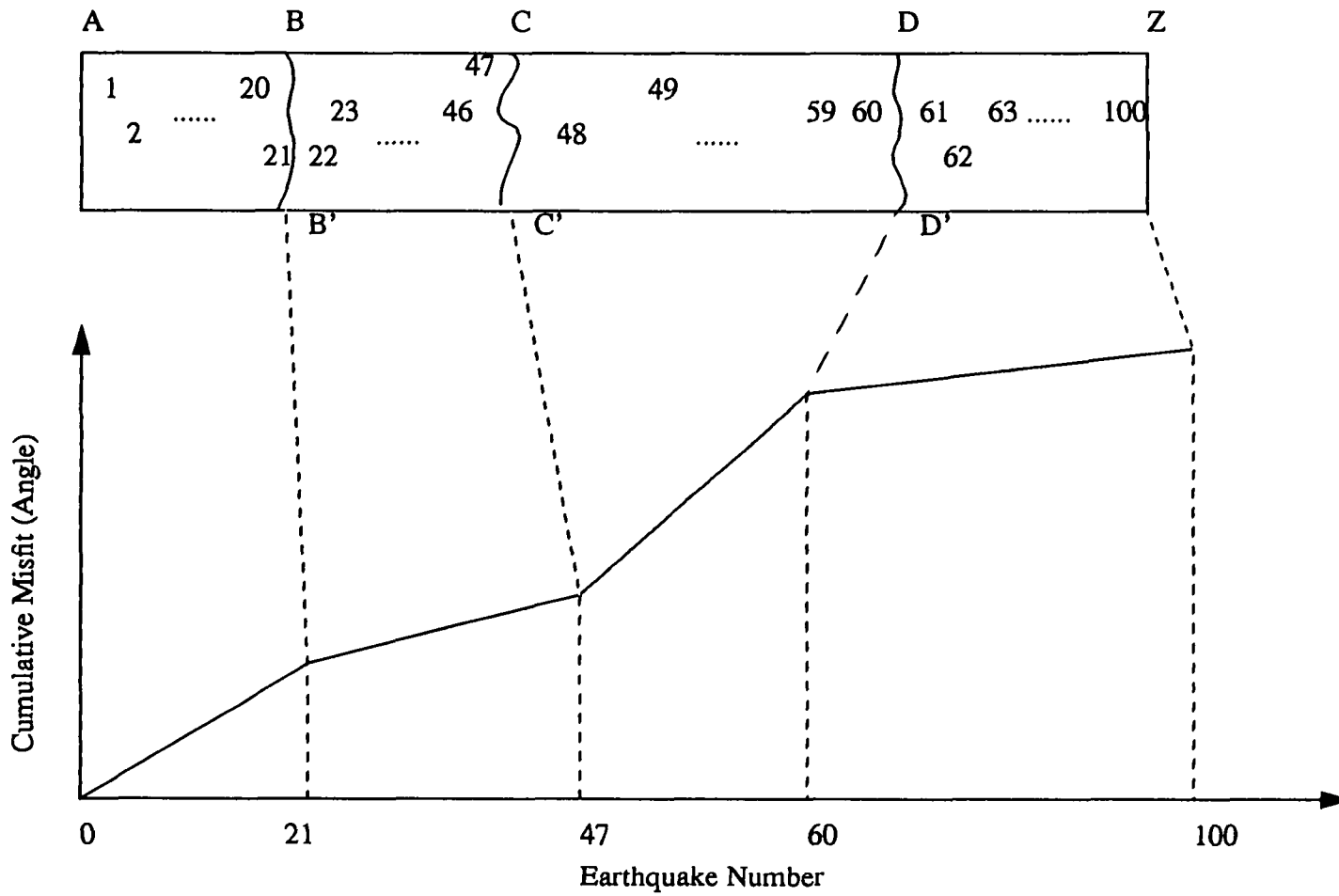


Figure A.1 Schematic plot shows that the segmentation of the fault AZ which can be found made up of 4 sub-faults, AB, BC, CD, and DZ. The BB', CC', and DD' are the boundaries of the segmentation based on the plot of the cumulative misfit angle as a function of the earthquake numbers which are lined from left to right according to their locations (numbers shown in the upper plot).

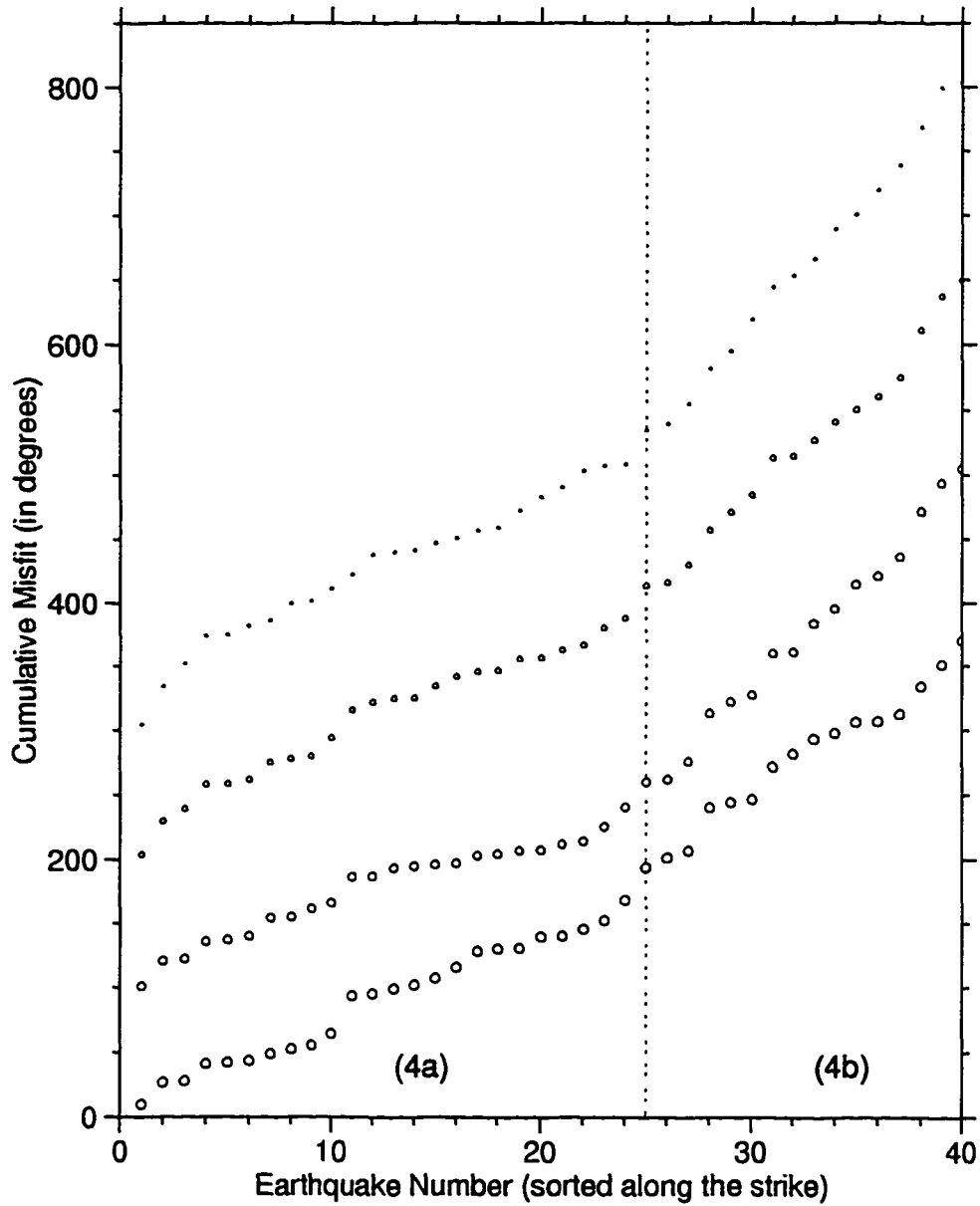


Figure A.2 Cumulative misfit as a function of strike at depth 40 - 50 km using four different test stress tensors. The changes of stress direction estimated around event number 25 separate the data set in this depth range into two sets (4a and 4b, Table 3.1). Their principal stress orientations are shown in Figures 3.11 and 3.13. All but the lowest curve have been shifted upward for clarity.

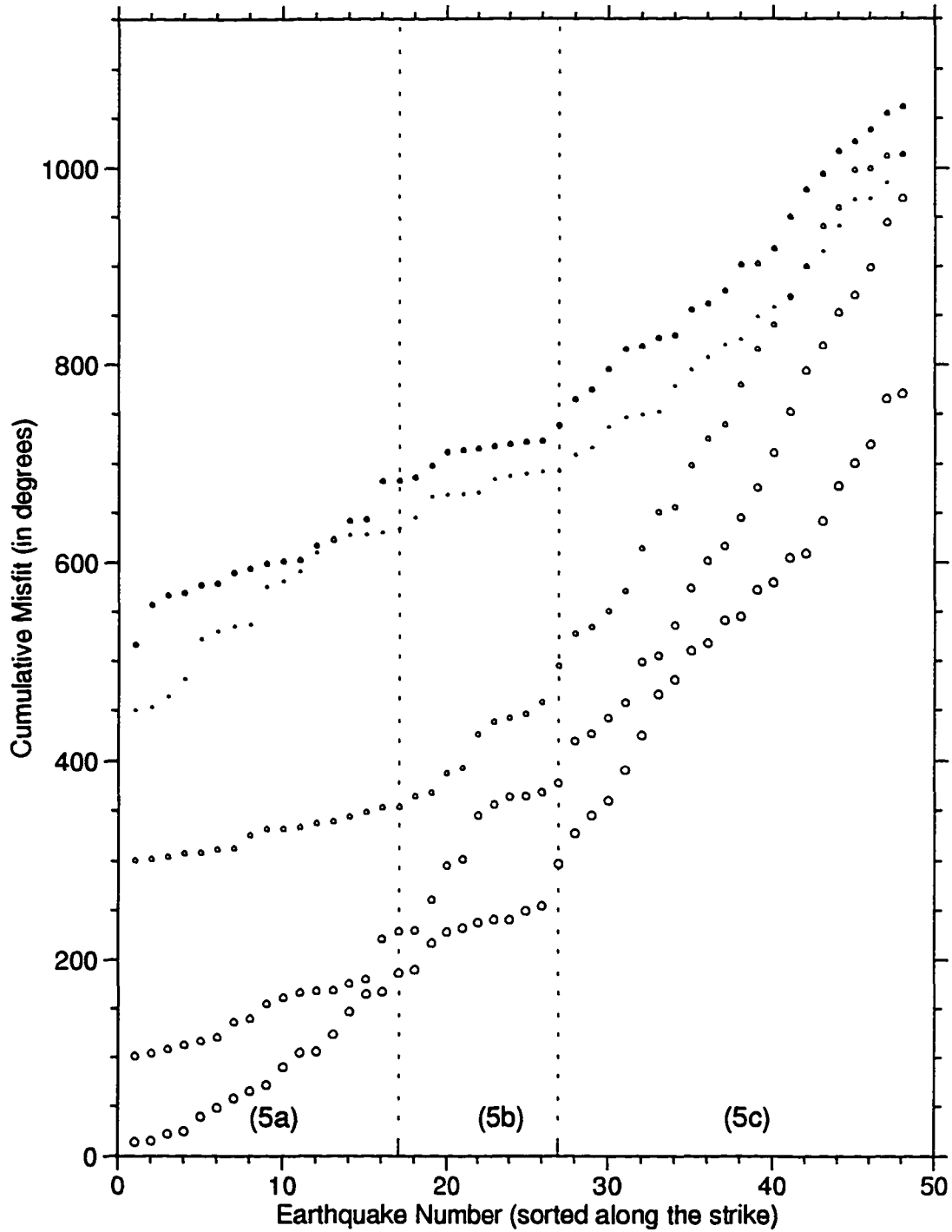


Figure A.3 Cumulative misfit as a function of strike at depth 50 - 60 km using five different test stress tensors. The changes of stress direction estimated around event number 17 and 27 separate the data set in this depth range into three sets (5a, 5b and 5c, Table 3.1). Their principal stress orientations are shown in Figures 3.12 and 3.13. All but the lowest curve have been shifted upward for clarity.

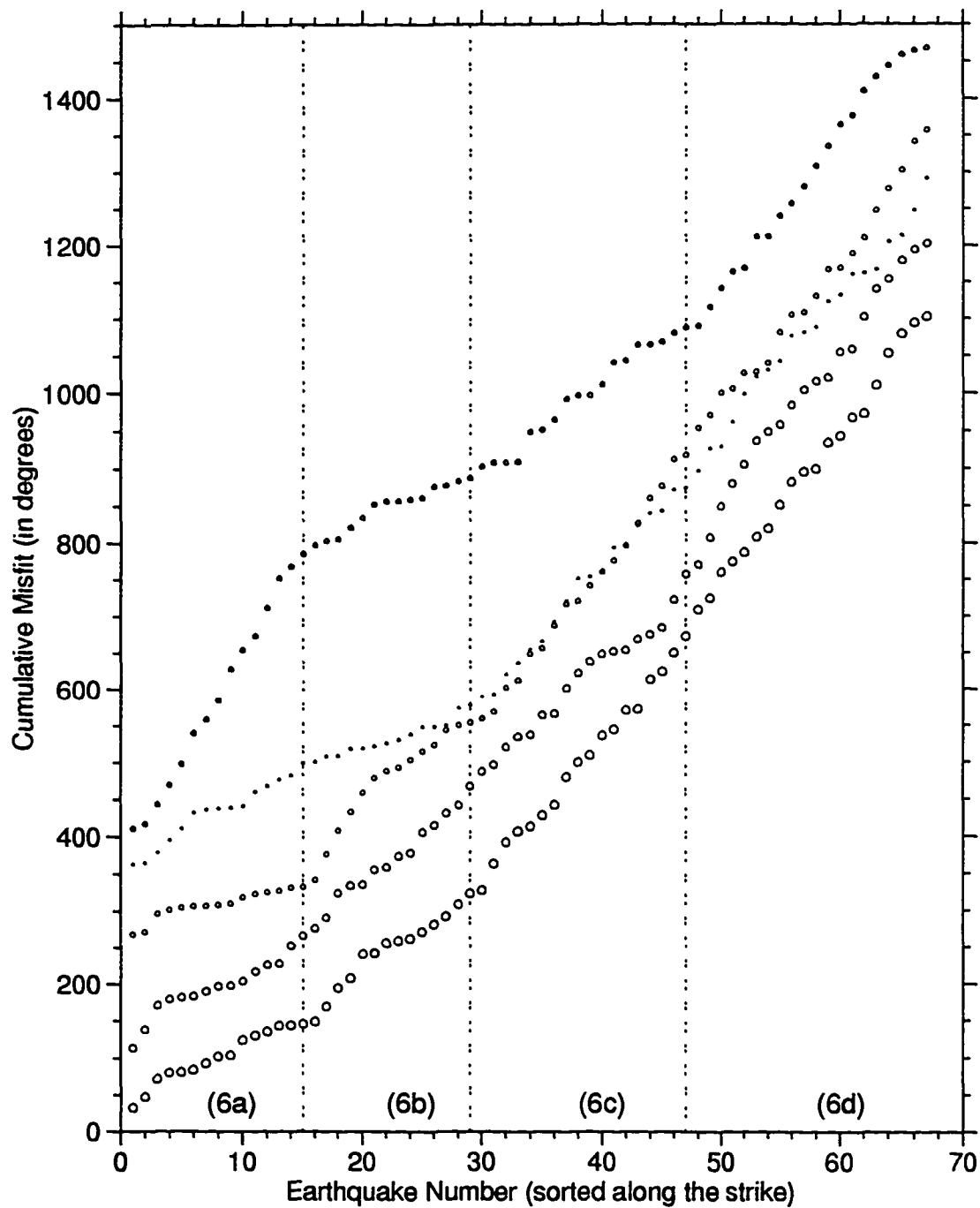


Figure A.4 Cumulative misfit as a function of strike at depth 60 - 75 km using five different test stress tensors. The changes of stress direction estimated around event number 15, 29 and 47 separate the data set in this depth range into three sets (6a, 6b, 6c and 6d, Table 3.1). Their principal stress orientations are shown in Figure 3.10. All but the lowest curve have been shifted upward for clarity.

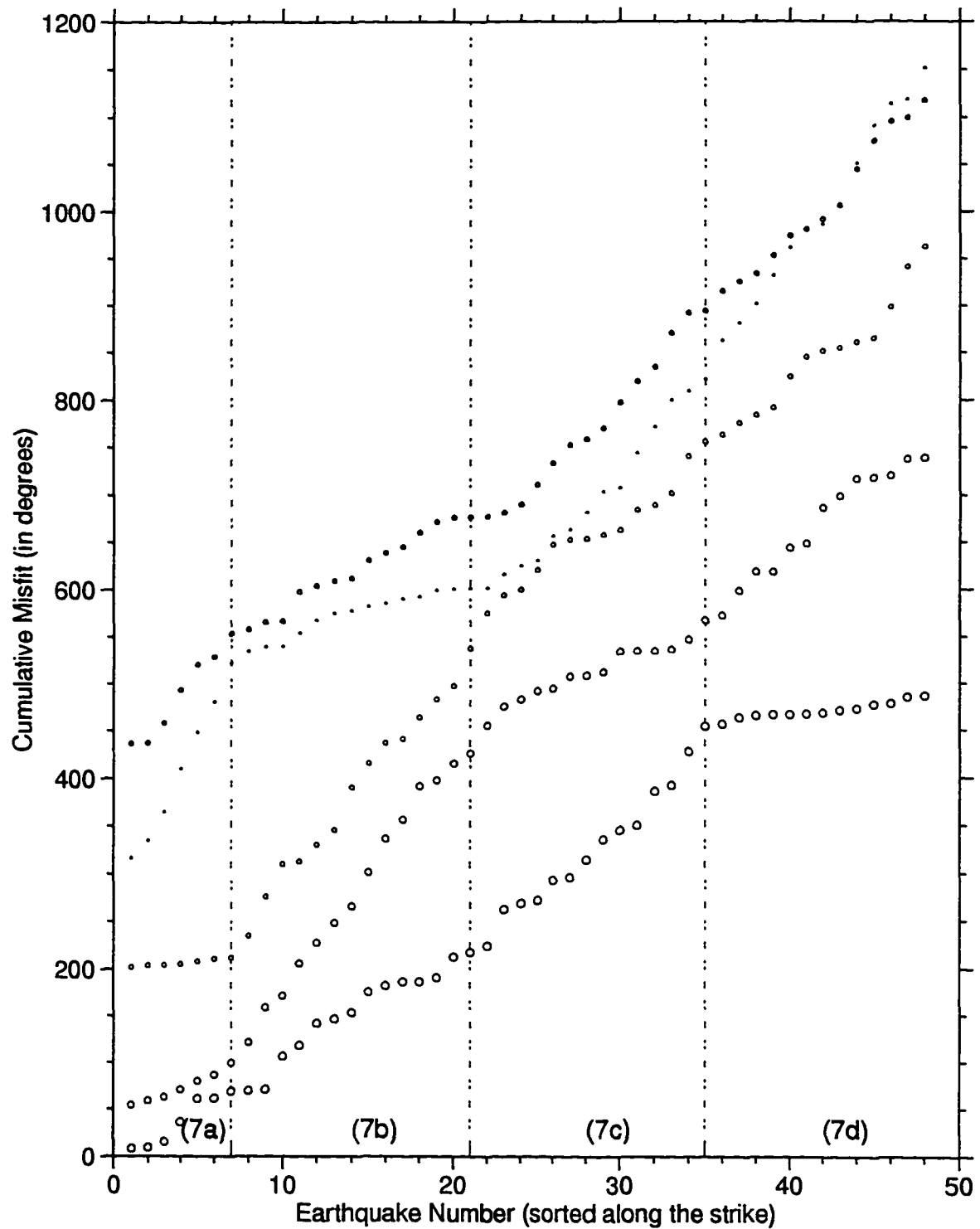


Figure A.5 Cumulative misfit as a function of strike at depth 75 - 90 km using five different test stress tensors. The changes of stress direction estimated around event number 7, 21 and 35 separate the data set in this depth range into four sets (7a, 7b, 7c and 7d, Table 3.1). Their principal stress orientations are shown in Figures 3.11 and 3.13. All but the lowest curve have been shifted upward for clarity.

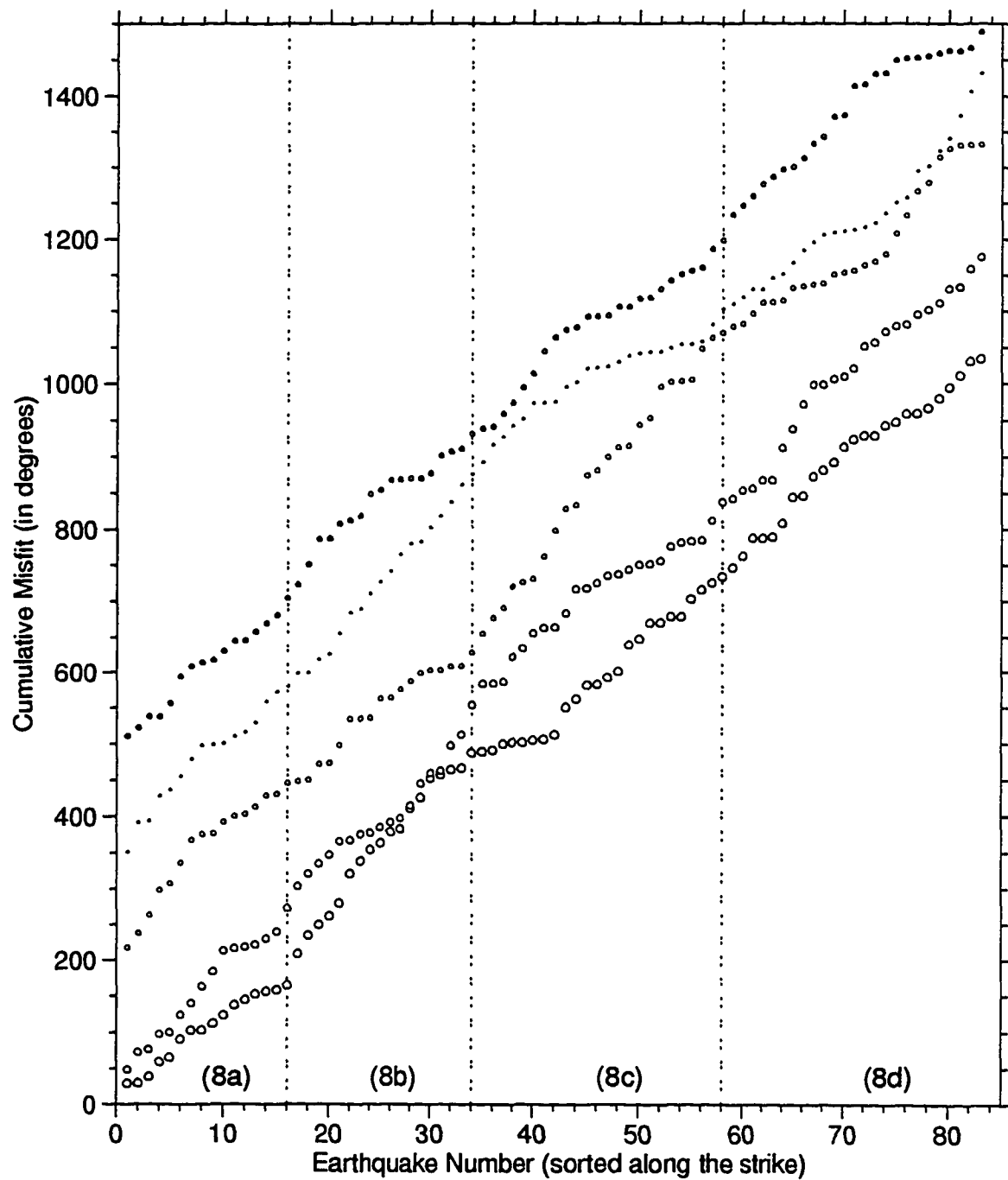


Figure A.6 Cumulative misfit as a function of strike at depth 90 - 120 km using five different test stress tensors. The changes of stress direction estimated around event number 16, 34, and 58 separate the data set in this depth range into four sets (8a, 8b, 8c and 8d, Table 3.1). Their principal stress orientations are shown in Figure 3.12. All but the lowest curve have been shifted upward for clarity.